A precise Higgs mass measurement at the ILC and test beam data analyses with CALICE

Dissertation Submitted to

Tsinghua University and Paris XI University

in partial fulfillment of the requirement

for the degree of

Doctor of Science

By

Ruan Manqi

(Physics)

Defense jury members:	M. V. Boudry	
	M. S. Chen	
	M. Y. Gao	Supervisor
	M. D. Ruan	Reporter
	M. Z. Yang	
	M. Z. Zhang	Supervisor
	M. S. Zhu	Chairman

Date of defense: 27/10/2008

Abstract

Utilizing Monte Carlo tools and test-beam data, some basic detector performance properties are studied for the International Linear Collider (ILC). The contributions of this thesis are mainly twofold, first, a study of the Higgs mass and cross section measurements at the ILC (with full simulation to the $e^+e^- \to HZ \to H\mu\mu$ channel and backgrounds); and second, an analysis of test-beam data of the Calorimeter for Linear Collider Experiment (CALICE).

For a most general type of Higgs particle with 120GeV the mass, setting the center-of-mass energy to 230GeV and with an integrated luminosity of 500fb^{-1}, a precision of 38.4MeV is obtained in a model independent analysis for the Higgs boson mass measurement, while the cross section could be measured to 5%; if we make some assumptions about the Higgs boson's decay, for example a Standard Model Higgs boson with a dominant invisible decay mode, the measurement result can be improved by 25% (achieving a mass measurement precision of 29MeV and a cross section measurement precision of 4%).

For the CALICE test-beam data analysis, our work is mainly focused upon two aspects: data quality checks and the track-free ECAL angular measurement. Data quality checks aim to detect strange signals or unexpected phenomena in the test-beam data so that one knows quickly how the overall data taking quality is. They also serve to classify all the data and give useful information for the later offline data analyses. The track-free ECAL angular resolution algorithm is designed to precisely measure the direction of a photon, a very important component in determining the direction of the neutral components in jets. We found that the angular resolution can be well fitted as a function of the square root of the beam energy (in a similar way as for the energy resolution) with a precision of approximately $80mrad/\sqrt{E/GeV}$ in the angular resolution.

Key words: ILC; Higgs mass; CALICE; ECAL

Résumé

En utilisant les outils de Monte Carlo et les données de test en faisceau, la performance d'un détecteur au futur collisionneur linéaire international a été étudiée. La contribution de cette thèse porte sur deux parties; d'une part sur une mesure de précision de la masse du boson Higgs et de la section efficace de la production avec le processus $e^+\tilde{e} \rightarrow HZ$ où le boson Z se désintègre en paire $\mu^+\mu^-$ et d'autre part sur une analyse des données de test en faisceau de la collaboration CALICE (CAlorimeter for Linear Collider Experiment).

Pour un Higgs de 120GeV, nous avons obtenu une précision de 38.4MeV sur la masse de Higgs et de 5% sur la section efficace en choisissant une énergie dans le centre de masse optimale de 230 GeV et avec une luminosité intégrée de 500 fb-1. Ces résultats sont indépendants d'un modèle de Higgs donné puisque aucune information sur la désintégration du Higgs n'a été utilisée dans l'analyse. Si on suppose que le Higgs est celui du modèle standard ou il se désintègre principalement en particules invisibles, la précision peut être améliorée de façon significative (29MeV pour la masse et 4% pour la section efficace).

Pour l'analyse des données de test en faisceau, mon travail concerne deux aspects. Premièrement une vérification sur la qualité des données en temps quasi réel et deuxièmement une mesure précise sur la résolution angulaire d'une gerbe électromagnétique dans le calorimètre prototype utilisé dans le test en faisceau. Le but pour la vérification de la qualité des données est de détecter des problèmes éventuels sur l'ensemble du détecteur y compris l'électronique, le système de haute tension et d'acquisition, et de classer des différentes données pour faciliter les analyses offlines. Pour déterminer la résolution angulaire du calorimètre électromagnétique, nous avons développé un algorithme qui est basée uniquement sur le dépôt d'énergie dans différentes cellules produites par le faisceau d'électrons sans utilisant l'information du détecteur de trace devant le calorimètre. Celle-ci est importante pour pouvoir identifier le composant neutre d'un jet. Nos résultats montrent que la dépendance de la résolution angulaire en énergie du faisceau est similaire à celle de la résolution en énergie et peut être décrite par $(74/\sqrt{(E/GeV)} + 8.7)$mrad.

Key words: ILC; Higgs mass; CALICE; ECAL

Contents

Chapter 1 Introduction 1
1.1 Brief introduction to the ILC project 1
1.1.1 Why particle physics needs the ILC 1
1.1.2 Key issues in the ILC project 4
1.2 Introduction to the CALICE Collaboration 5
1.3 Main contributions and outline of this thesis 6

Chapter 2 Higgs physics at ILC 8
2.1 Introduction: the Higgs particle in the SM and beyond 8
2.2 The SM Higgs particle 9
2.3 Measurement of the SM Higgs boson mass at the ILC 11
2.4 Measurement of other SM Higgs observables at the ILC 15
2.4.1 Measurement of the Higgs boson spin and parity 15
2.4.2 Higgs decay branching ratios and total width 17
2.4.3 Higgs self-coupling measurement 20
2.5 Summary 22

Chapter 3 Introduction to ILC detector, accelerator and software 24
3.1 Introduction 24
3.2 Current 4 ILC detector concepts 25
3.2.1 SiD concept 25
3.2.2 LDC concept 27
3.2.3 GLD concept 29
3.2.4 4^{th} concept 31
3.3 The emergence of the ILD Collaboration and current status of the ILD detector optimization study 33
3.4 Introduction to the LDC01_Sc concept 36
3.4.1 Tracking system 38
3.4.2 μ momentum measurement accuracy and fast simulation tool 41

3.4.3 Calorimetry system....44
3.5 Introduction to the ILC accelerator and beam parameters....46
3.5.1 The ILC accelerator....46
3.5.2 beam parameters and the beam-beam effect....50
3.6 Introduction to the ILC software....54
3.6.1 The LCIO and MARLIN....54
3.6.2 From the generator to the analysis: ILC simulation, reconstruction and analysis software....55
3.6.3 Grid: massive computing and storing tool....59
3.6.4 GALICE software....60
3.6.5 Discussing....60
3.7 Summary....61

Chapter 4 Higgs boson recoil mass and cross section measurements through the $e^+e^- \to HZ \to H\mu\mu$ channel....62
4.1 Introdcution....62
4.2 The Radiation effect....63
4.3 Main backgrounds and precuts....68
4.4 Model independent analysis of the Higgs boson mass and cross section measurements....72
4.4.1 Replacement of the precuts and new variables for the cuts....72
4.4.2 The parameter optimization for event selection....76
4.4.3 The fit method and fit result....78
4.5 Higgs boson mass and cross section measurements in a model dependent analysis....83
4.5.1 Variables used to distinglish events with SM Higgs boson and invisibly-decaying Higgs boson events....83
4.5.2 Mass and cross section measurements for the SM Higgs....85
4.5.3 Mass and cross section measurements for an invisbly-decaying Higgs boson....87
4.6 Preliminary study on beam parameter optimization....89
4.7 Summary....95

Chapter 5 Introduction to the CALICE test beam experiment 97
5.1 Brief introduction to the CALICE project 97
5.2 Introduction to prototype sub-detectors 99
5.2.1 The ECAL 99
5.2.2 The HCAL and TCMT 101
5.3 Setting up the CALICE test beam experiment 102
5.4 DAQ and data flow for the CALICE test beam experiment 108
5.4.1 ECAL Calibration 108
5.4.2 Noise level 110
5.4.3 The Data quality check 111
5.5 Summary 118

Chapter 6 CALICE test beam data analysis, ECAL part 119
6.1 Introduction: interaction of beam particles and materials 119
6.2 The energy response and resolution for the ECAL prototype 122
6.3 Shower profile and spatial resolution 126
6.3.1 The longitudinal shower profile 126
6.3.2 The transverse shower profile 128
6.3.3 The spatial resolution for the CALICE ECAL prototype 130
6.4 Angular resolution for the CALICE ECAL prototype 132
6.4.1 Introduction and motivation 132
6.4.2 Algorithm 135
6.4.3 Results for angle measurements 138
6.5 Summary 140

Chapter 7 Summary and perspective 142
7.1 Summary of this thesis 142
7.2 Perspective 145

Reference 147

Acknowledgements 150

CV and Publication 151

Chapter 1 Introduction

Utilizing Monte Carlo tools and a test beam data analysis, this thesis explores some basic detector performance properties for the International Linear Collider (ILC). The contributions made for this thesis are mainly twofold, first, a study of the Higgs mass and cross section measurements at the ILC (with full simulation to the $e^+e^- \to HZ \to H\mu\mu$ channel and corresponding backgrounds); and second, development of the Calorimeter for Linear Collider Experiment (CALICE) test beam data analysis. The first Chapter provides a brief introduction to the motivations and background for this study.

1.1 Brief introduction to ILC project

The ILC, a proposed new particle accelerator, promises to radically change our understanding of the universe – revealing the origin of mass, uncurling hidden dimensions of space, and explaining the mystery of dark matter. Advanced super conducting technology will accelerate and collide particles to incredibly high energies down tunnels that span more than 30 kilometers in length. State-of-the-art detectors will record the collisions at the centre of the machine, opening a new gateway into the Quantum Universe, an unexplored territory…

---- From ILC Passport [1]

1.1.1 Why particle physics needs International Linear Collider?

The basic subject investigated by high energy physics is the elementary particles and the interactions between them. These play an essential role in many aspects of the evolution of the universe, aspects ranging from the big bang to the decoupling of the different interactions as we know them today, from the birth of a galaxy to the collapse of a star, from the emergence of the first hydrogen atom to the formation of

life, *etc*. More philosophically, the fundamental questions that high energy physics attempts to answer are: where do we come from, what are we made of, and what is the fate of the universe?

Endeavors dating back to the set up of the first accelerator just prior to the middle of last century have resulted in many success stories culminating in the establishment of the so-called the Standard Model (SM), which can account for nearly all phenomena in high energy experiments and is widely regarded as the most important achievement of the 2nd half of 20th century. Despite its myriad successes, the SM is inadequate as a truly fundamental theory. Reasons for this include the hierarchy problem and the excessive number (17) of free parameters. Required aspects of the SM also remain mysterious. Paramount among these is the yet undiscovered Higgs particle, which plays an essential role in mass generation in the SM. In addition, astrophysical data shows that a majority of the matter in the universe is composed of dark matter (as opposed to visible matter), which cannot be composed (solely) of SM particles. The next generation of accelerators, mainly the LHC (Large Hadron Collider) and the ILC (see Figure 1.1) will probe these mysteries.

Searching for the Higgs particle and precisely measuring its properties is the central task for the LHC and the ILC. The LHC and ILC will also try to answer the questions of how the basic interactions might be unified, why there is asymmetry between matter and anti-matter in the universe [2], and what the nature of the dark matter is, *etc*. Our understanding of the basic interactions of elementary particles is expected to be raised to a new level by the LHC and the ILC.

The LHC [3] is a proton-proton collider, installed in the 27 km long tunnel at CERN. The center-of-mass energy is expected to reach 14 TeV at the LHC. There are four detectors on the LHC: ATLAS, CMS, LHCb and ALICE. The main task of the ATLAS and CMS detectors is to probe the Higgs sector while that of LHCb is to study CP violation in b-physics and ALICE will focus on investigating the quark-gluon plasma phase transition as well as the thermodynamics for the early universe through heavy ion collisions.

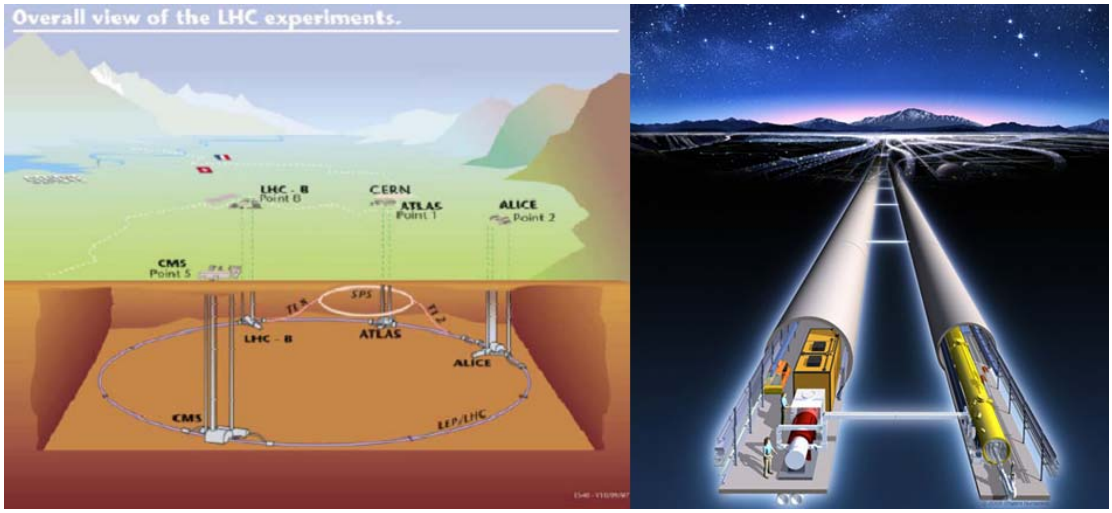

Figure 1.1 The LHC [2] and the ILC [3]

The ILC is a linear electron-positron collider [4] with a proposed length of 31 km. The center-of-mass energy of the ILC would range from the Z threshold up to 1 TeV, its luminosity could reach 500 fb^{-1} in the first 4 years and will be even higher afterward. The construction of the ILC could commence soon after the principal physics discoveries expected at the LHC have been attained. Compared to the LHC, the ILC has three main advantages:

First, the center-of-mass energy is precisely known and tunable;

Second, an electron-positron ILC machine allows for polarized beams. Since left-handed fermions behave differently than the right-handed fermions of the same flavor in the SM (since their quantum numbers differ), beam polarization can be used to increase desired signal cross sections while simultaneously suppressing unwanted background cross sections. For example, using a beam highly polarized in favor of right-handed electrons will greatly suppress the WW production cross section, since W bosons only couple to left-handed electrons. Also beam polarization could be utilized to detect the SUSY particles [2].

Third, QCD backgrounds are much smaller at the ILC [5]. At the LHC, QCD backgrounds are so huge that finding a signal event is like searching a needle in a haystack. Thus detectors at the LHC will require extremely stingy triggering requirements. In contrast, signal processes at the ILC range from comparable in size

to the expected backgrounds to only a couple of orders of magnitude down (see Figure 1.2). Thus detector design for the ILC can focus mainly on maximizing precision in the measurements.

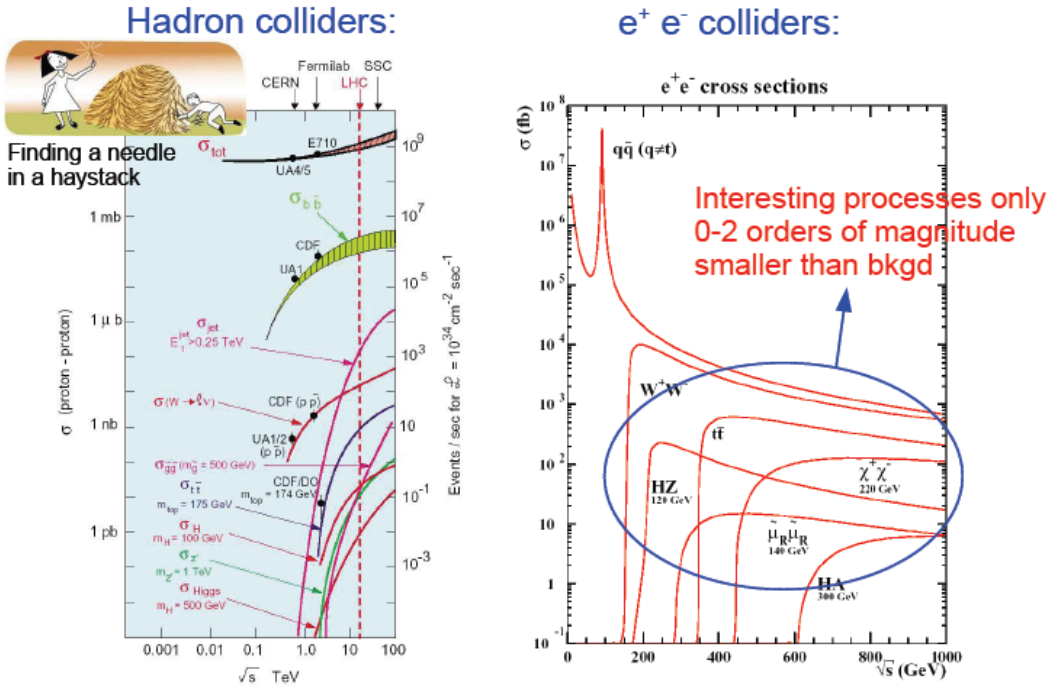

Figure 1.2 Cross section comparisons for the LHC and the ILC [5]

The ILC will be able to detect a SM Higgs boson throughout its theoretically-allowable mass range. The ILC also has the unique capability to scan all possible new interactions with energy thresholds at or below the TeV scale. If TeV-scale supersymmetry (SUSY) exists, the ILC could precisely measure the profiles of all the SUSY particles discovered at the LHC. Top quark physics could also be precisely studied using the huge number of $t\bar{t}$ events generated at the ILC.

1.1.2 Jet energy measurement: key issues in the ILC project

Table 1.1 lists some of the ILC benchmark channels (include both SM and MSSM processes) [6]. $t\bar{t}h$ channel could be used to measure the Higgs-top quark coupling, and hhZ channel is used to determine the Higgs self coupling constant.

Most of the benchmark channels have jets in their final states, thus an ILC detector must be able to precisely measure jet energies, with precision up to $0.3/\sqrt{E/GeV}$ [7] --- roughly a factor two better than what has been achieved in previous detectors. One of the optimal methods to reach this precision is the Particle Flow Analysis (PFA).

$Z\gamma$	2 ℓ, 2 jets
W^+W^-	1 ℓ+2 jets, 4 jets
$t\bar{t}$	ℓ+jets, 6 jets
$t\bar{t}h$	8 jets
hZ	2ℓ+2 jets, 4 jets
hhZ	2ℓ+4 jets, 8 jets
$\chi_1^0\chi_1^0$	jets + $\not{E}$
$\tilde{t}\tilde{t}$	6 jets+$\not{E}$
$\not{R}_p$ $\chi_1^0\chi_1^0$	2ℓ+ 4 jets, 6 jets
$\not{R}_p$ $\chi^+\chi^-$	2ℓ+ 6 jets, 10 jets
graviton	no-pointing γ
extra-dimension	γ+$\not{E}$

Table 1.1 Benchmark channels at the ILC [6]

The PFA is based on the idea that different particles within a jet should be individually identified and reconstructed in different subdetectors. For neutral particles this requires a calorimeter with high pattern-recognition efficiency, obtained for instance by introducing an extremely high level of spatial granularity. To study and develop the calorimeter for the ILC, the CALICE collaboration has been formed [8].

1.2 Introduction to the CALICE collaboration

Today the CALICE collaboration consists of over 200 physicists from 12 countries. It aims at designing and constructing a high spatial-granularity calorimetry system optimized for the PFA. The CALICE collaboration has designed and constructed some calorimeter prototypes, which was then subjected to test beam

experiments. Aims of these studies have been twofold:

To study the physics performances of highly granular calorimeters;

Check the feasibility of large detectors with “technological” prototypes;

Improve the MC simulation tools use the test beam data.

A large amount of test beam data has been obtained in the test beam program. The analysis of said data is part of thesis (see Chapter 5 and Chapter 6).

1.3 Main contribution and outline of this thesis

This thesis is divided into seven chapters. Chapter 2 and Chapter 3 are dedicated to the introduction of relevant backgrounds: in Chapter 2 we introduce the physics backgrounds (Higgs physics at ILC) and in Chapter 3 we deal more specifically with backgrounds in an ILC machine, detector and software. Higgs boson mass and production cross section measurements are discussed in Chapter 4. After a discussion on radiation effects and backgrounds, the model-independent and model-dependent analyses are presented, and then Chapter 4 concludes with a preliminary study on beam-parameter selection.

Chapter 5 and Chapter 6 are associated with the CALICE test beam data analysis. In Chapter 5 we outline the experimental set up and present its data flow, calibration and data-quality checks. Chapter 6 focuses on the energy, spatial and angular resolutions of the CALICE ECAL prototype. Here we introduce a track-free algorithm for angle measurements which could be used to measure the direction of an injection photon with ECAL hits. In Chapter 7 we summarize our results and give a brief perspective overview.

For the Higgs boson mass and cross section measurements, the $e^+e^- \to HZ \to H\mu\mu$ channel acted as the signal, with all radiation effects and SM backgrounds taken into account. The mass of the Higgs boson was assumed to be 120GeV, and the center-of-mass energy was set to 230GeV. The recoil mass method, which requires no information concerning the Higgs decay final state, was used for the mass measurement. This obviated the need for employing any potentially model-dependent cuts, rendering this model independent analysis. The precision of

the resulting Higgs boson mass measurement was 38MeV. A cross section precision of 5% was also obtained. Inclusion of some assumptions as to the Higgs decay final state (such as limiting the analysis to a SM Higgs boson or an invisibly-decaying Higgs boson) improved the mass-measurement precision to 29 MeV (and the cross section measurement precision to 4%) – about a 25% improvement as compared to the model independent analysis. A fast simulation tool that could predict the Higgs boson recoil mass spectrum was also developed and utilized in a preliminary study on beam-parameter optimization (see Chapter 4).

In the CALICE test beam data analysis, my work is focused on data-quality checks and track-free ECAL angular resolution determinations.

We collected a large amount of data in the CALICE test beam experiments. The quality of data directly affects the results from the analysis. We made a scan of almost all the data files collected in the 2006-2007 CALICE test beam experiment, searching for abnormal signals, unexpected phenomena (for example a bump in the total energy spectrum, time-dependent noise, *etc*.) and quickly fed results back to the collaboration. The data files have also been classified into different groups, making it easier for later analyses (see Chapter 5).

The energy, spatial and angular resolutions are considered as the characteristic parameters of a calorimeter. We have developed a track-free angular resolution algorithm (using only the ECAL information), and have compared results from our algorithm with previous CALICE collaboration angular-measurement results (which use drift-chamber information to reconstruct a reference track). The motivation to develop a track-free algorithm is to measure the injection direction of a photon which might be generated beyond the interaction point (for example, a FSR photon or a photon resulting from the decay of a long-lived neutral SUSY particle), see section 6.3.

Chapter 2 Higgs Physics at the ILC

2.1 Introduction: Higgs Particle in the SM and beyond

The origin of mass is one of the essential questions that particle physics attempts to answer. In the SM (Standard Model), particles gain their mass through the interactions with the Higgs field. The Higgs field is an isodoublet complex scalar field which breaks the electroweak symmetry to the electromagnetic symmetry ($SU(2)_L \times U(1)_Y \rightarrow U(1)_{EM}$) by acquiring an non-zero vacuum expectation value through its self-interactions. Masses are generated for the gauge bosons of the weak interaction ($W^{\pm}$, Z) when they absorb three would-be Goldstone bosons, and the fermions get their mass through Yukawa couplings with the Higgs field. The sole remaining degree of freedom from the Higgs field forms the Higgs particle.

A Spontaneous Symmetry Breaking (SSB) mechanism, which necessitates the existence a Higgs sector, is the way to generate mass in many physics models beyond the SM, for example, the MSSM (Minimal Supersymmetric Standard Model) or the Little Higgs models. Now let's review the Higgs sectors in these two highly-popular beyond-the-SM physics models [10].

In the MSSM, two Higgs isodoublets have eight degrees of freedom. After SSB, three degrees of freedom have been absorbed and act as the longitudinal degrees of freedom of the gauge bosons ($W^{\pm}$, Z), and the remaining five degrees of freedom remain as Higgs particles. So instead of the one neutral CP-even Higgs particle in the SM, five Higgs particles in the MSSM: two charged Higgs particles ($H^{\pm}$), two CP-even Higgs particles (h and H; where h is the lighter Higgs particle) and one CP-odd Higgs particle (A). The upper limit of the lightest Higgs (h) mass ranges from ~100GeV to ~140GeV, depending upon the choice of various input parameters, while the masses of the other MSSM Higgs particles range from 240GeV to 1TeV.

In Little Higgs models, Higgs particles are viewed as Goldstone bosons generated via a SSB process. As described by the Goldstone theorem, a Goldstone

boson always has zero mass, so the mass of the Higgs particles should be much lower than the energy scale of the SSB process ---- which means there exist some new SSB-associated interactions at an energy scale much higher than the TeV-scale. These new interactions (perhaps SM-like) bring with them a family of new particles.

Up to now, the SM has had myriad success in explaining nearly all experimental phenomena, but the predicted Higgs particle has not yet been discovered in the laboratory. This Higgs particle is the only particle predicted by the SM which has not yet been directly found. So searching for Higgs particle and precisely measuring its properties is one of the central tasks for the LHC and ILC. In experimental particle physics, the key problems about Higgs particle are:

Is there a Higgs particle? How can we detect it in the laboratory?

What is the nature of the Higgs particle? Is there any physics beyond the SM?

In this chapter we will introduce the SM Higgs boson and the measurements of its properties at the ILC.

2.2 The SM Higgs Particle

The SM Higgs particle is a spin-parity 0^+ particle, and its mass is the only unknown parameter in the symmetry-breaking sector of the SM. There are strong constraints on the Higgs boson mass: the lower limit on the SM Higgs boson mass is 114GeV at 95% CL [11], given by the LEP experiments; if the SM is valid up to scales near the Planck scale, the Higgs boson mass is constraint to lay within the 130-190GeV range. If the mass of the Higgs particle lies beyond this constraint, new interactions are expected to occur between ~1TeV to the Planck scale: the heavier the Higgs particle is, the lower the scale of new physics is. If the Higgs particle were to be as massive as 1TeV, then we would expect to observe new interactions at the TeV scale. (So the unique capability of ILC – fully scan for new interactions at the TeV scale – is very attractive.)

In the SM, the masses of other particles are proportional to their couplings to the Higgs particle, and the mass of Higgs particle constrains the

daughter particles into which it may decay. Thus, in the SM, the decay branching ratios and the total width of the Higgs particle are completely determined by the mass of Higgs particle. See Figure 2.1[2]. For the analyses reported in this thesis, the Higgs boson mass was assumed to be 120GeV.

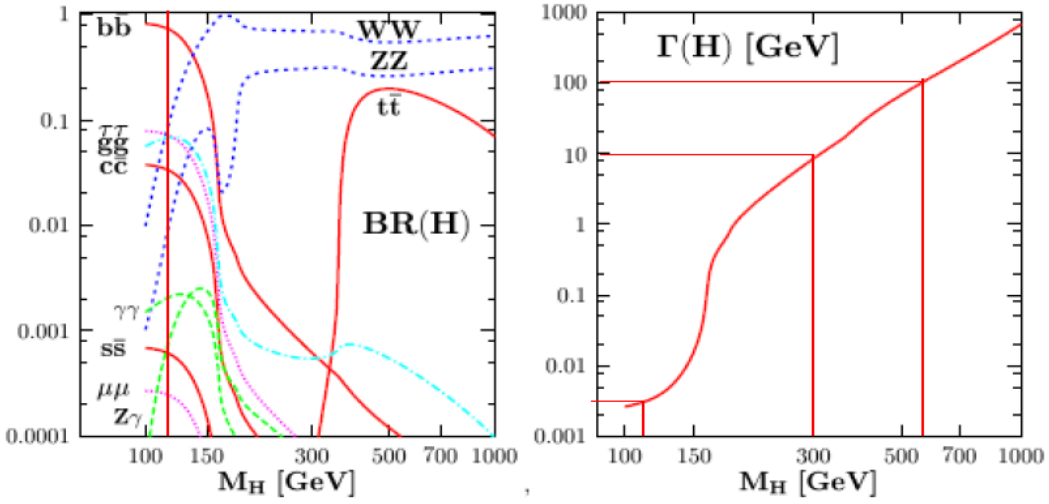

Figure 2.1 Relationship between the Higgs boson mass and the Higgs boson decay branching ratios and total width [2]

As shown in Figure 2.1, if the Higgs mass is lower than 150 GeV, the Higgs will mainly decay into a pair of b, c quarks or τ leptons; it could also decay into a pair of gluons or photons via a heavy quark loop. The total width of the Higgs particle with a mass below 150GeV is very small. If the mass of the Higgs particle reaches 150 GeV, the Higgs particle will be able to decay into a pair of W bosons, and its width increases rapidly. Similar phenomena occur when the Higgs mass is increased to the Z boson and the top quark thresholds – for a 500GeV Higgs particle, the width grows to ~100GeV.

The spontaneous breaking of electroweak symmetry in the SM is realized through the quartic self-interactions of the Higgs field (known as the Higgs potential), which lead to a non-vanishing vacuum expectation value [10]. This means that there are trilinear and quartic vertices for the Higgs particle (mark the coupling constants with λ_{HHH} and λ_{HHHH} respectively). As shown in follow equation, the

corresponding couplings are proportional to the square of Higgs boson mass. Direct measurement to the Higgs boson self-coupling (λ_{HHH}) would be the most decisive experimental confirmation of the SM framework

$$V(\phi) = -\mu^2|\phi|^2 + 0.5\lambda|\phi|^4$$
$$\lambda_{HHH} = 3\sqrt{\sqrt{2}G_F}M_H^2, \quad \lambda_{HHHH} = 3\sqrt{2}G_F M_H^2.$$

Next let's introduce the measurements of Higgs particle properties at the ILC.

2.3 Measurement of the SM Higgs particle mass at the ILC

The ILC energy range (90GeV-1TeV) covers the entire allowable mass spectrum for a SM Higgs boson. At the ILC, the Higgs particle will be produced mainly through the W-fusion process ($e^+e^- \to Hvv$) and the Higgs-strahlung process ($e^+e^- \to HZ$). The corresponding Feynman diagrams are shown in Figure 2.2. As the center-of-mass energy is increased, the cross section for the Higgs-strahlung process drops as *1/s* (typical of an S-wave process), while the cross section for W-fusion process increases as $log(s/M_H^2)$. Thus, in the low energy region, the Higgs-strahlung process is more important, while for higher center-of-mass energies the W-fusion process dominates (see Figure 2.3).

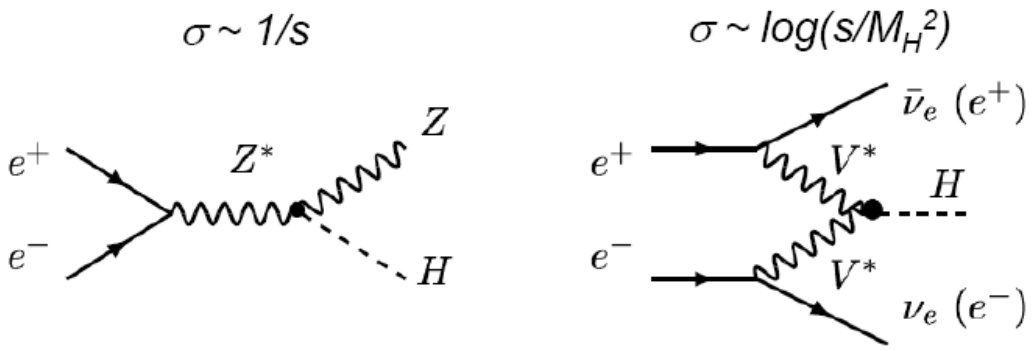

Figure 2.2 Leading-order diagrams for Higgs particle production at the ILC [2]

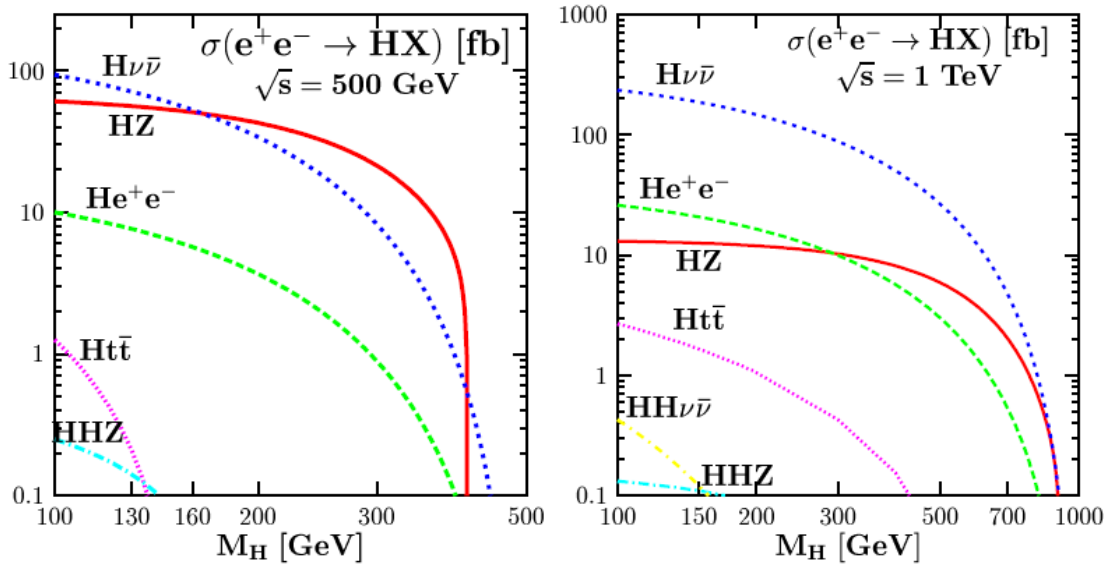

Figure 2.3 Cross sections of processes with Higgs boson production on the ILC [2]

The final state of the Higgs-strahlung process contains a Z-boson, which has a probability of 3.3% to decay into either an electron-positron pair or a muon-antimuon pair. Since we know the central-of-mass energy quite precisely at the ILC, and since the momenta of the electrons and the muons can be highly accurately measured by the detector (especially for muons which radiate far less than electrons), the mass of the Higgs particle may be very precisely determined via the recoil mass method [12].

According to the energy-momentum conservation law, the 4-momentum of Higgs particle can be expressed as

$$(\sqrt{s} - (E_1 + E_2),\ -(P_1^x + P_2^x),\ -(P_1^y + P_2^y),\ -(P_1^z + P_2^z)), \tag{2.1}$$

here (E_1, P_1), (E_2, P_2) are the 4-momenta of the two leptons. Thus the invariance mass of Higgs particle is

$$m_h^2 = s + m_{dileptons}^2 - 2(E_1 + E_2)\sqrt{s}\,. \tag{2.2}$$

Simultaneously knowing the number of $e^+e^- \to HZ$ events, which enables us to measure the cross section for this process, then allows us to calculate the coupling

between the Higgs particle and the Z boson: $g^2 \propto \sigma = N / L\varepsilon$.

Figure 2.4 shows the correlation between the cross section and the center-of-mass energy. The cross section increase rapidly above the threshold (210GeV with 120GeV Higgs mass) and then taper off slowly as *1/s* as is typical for an S-wave process [12]. The cross section is maximal at a center-of-mass energy of 240GeV. Figure 2.4 also illustrates how beam polarization and the ISR (initial state radiation) affect the cross section. As is well known, in the SM the left hand and right hand fermions have different quantum numbers, and thus their couplings to the Z boson are different; also the S-wave process requires the total angular momentum of the system be equal to 0. Thus if we use an achievable polarization at the ILC, 80% polarized electron beam and a 60% polarized positron beam, the cross section for Higgs-strahlung process will increase by 58%. According to phase-space restrictions and the cross section – center-of-mass energy dependence, the ISR will suppress the cross section for center-of-mass energies lower than 300GeV, and increase the cross section a little for higher center-of-mass energies [13] (in Figure 2.4 the beamstrahlung effect is not taken into account).

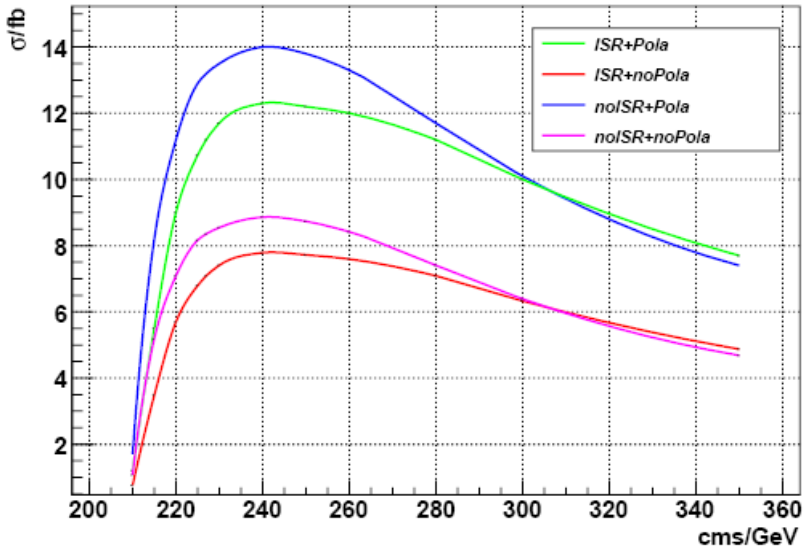

Figure 2.4 Cross section of Higgs-strahlung process as a function of center of mass energy at the ILC (80% polarized electron beam and 60% polarized positron) [13]

The momentum of a charged particle is measured through the bending of its track in the magnetic field of the detector. This means that lower energy tracks yield better track momentum resolution, so that using a smaller center-of-mass energy would result in a gain in the Higgs boson mass resolution. In this thesis, with assuming a 120GeV Higgs boson mass, we set the center-of-mass energy equal to 230GeV, which is slightly less than the energy at which the cross-section reaches its maximum value. With an integrated luminosity of $500fb^{-1}$, the Higgs boson mass can be measured to a precision of 38 MeV (model independent analysis) or 29 MeV (model dependent analysis) see Chapter 4.

Besides the recoil mass method, the Higgs boson mass could also be measured via a constraint fit method with the $e^+e^- \to HZ \to b\bar{b}q\bar{q}$ process – by measuring directly the jet momenta from the Higgs boson decay [14]. The Higgs boson mass determination relies on a kinematical 5-C fit imposing energy and momentum conservation and requiring the mass of the jet pair closest to the Z mass correspond to M_Z. The main advantage of this constraint fit method is the large statistics available with this process. And, since the relative error on the Higgs boson mass measurement is proportional to the relative error on the jet energy resolution, this method yields better results as the center-of-mass energy is increased. Given a 350GeV center-of-mass energy and $500fb^{-1}$ of integrated luminosity, the precision of the Higgs boson mass measurement is 70 MeV. Results from such a fit are shown in Figure 2.5.

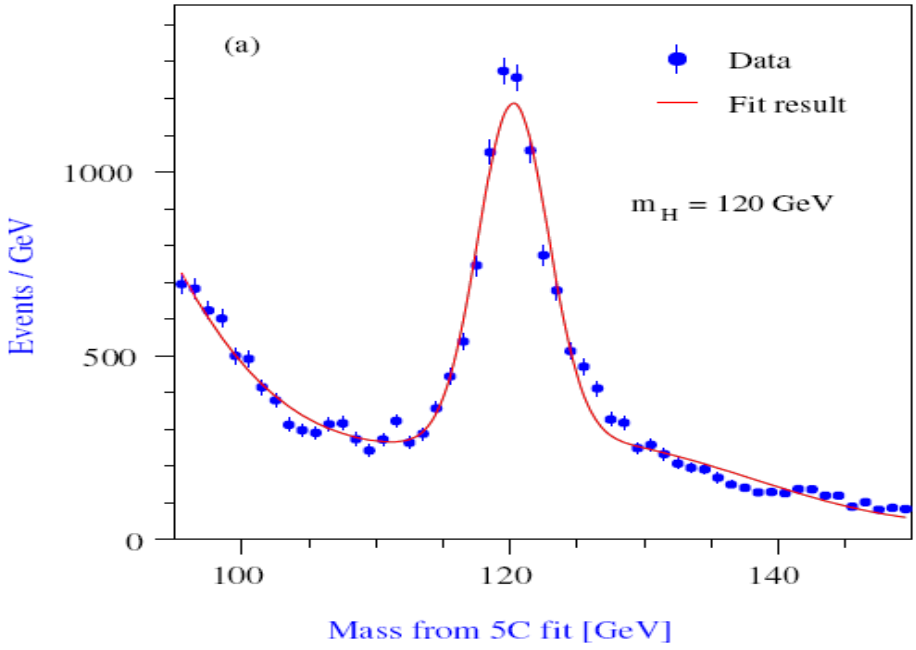

Figure 2.5 Higgs boson mass measurement via a constraint fit to the $e^+e^- \to HZ \to b\bar{b}q\bar{q}$ process [14] at 350GeV center-of-mass energy

2.4 Measurement of other SM Higgs observables at the ILC

Large numbers of events containing Higgs bosons are expected to be collected at the ILC, making it possible to precisely measure Higgs boson properties. Besides the Higgs boson's mass, other observables include its spin, parity, lifetime (width), decay branching ratios (or the coupling strengths of the Higgs boson to other particles) and the self-coupling constant (λ_{HHH}) of the Higgs boson. Here we succinctly introduce the methods and the expected accuracies/precisions for each of these measurements.

2.4.1 Measurement of the Higgs boson's spin and parity

In the SM the Higgs particle is a CP-even scalar particle. The parity of the Higgs boson can be inferred through measurement of the parities of the daughter particles into which it decays. The Higgs boson's parity can also be determined through measurement of the angular distribution of $e^+e^- \to ZH$ events. As shown in the left plot of Figure 2.6, for an even-parity Higgs particle, $e^+e^- \to ZH$ events will

concentrate in the region of large polar angles, while for an odd-parity Higgs particle, events predominately be located in the forward region. Herein an odd-parity pseudoscalar Higgs particle event will be written as A, as with the CP-odd Higgs particle of the MSSM, making the production process $e^+e^- \to ZA$ [2, 15].

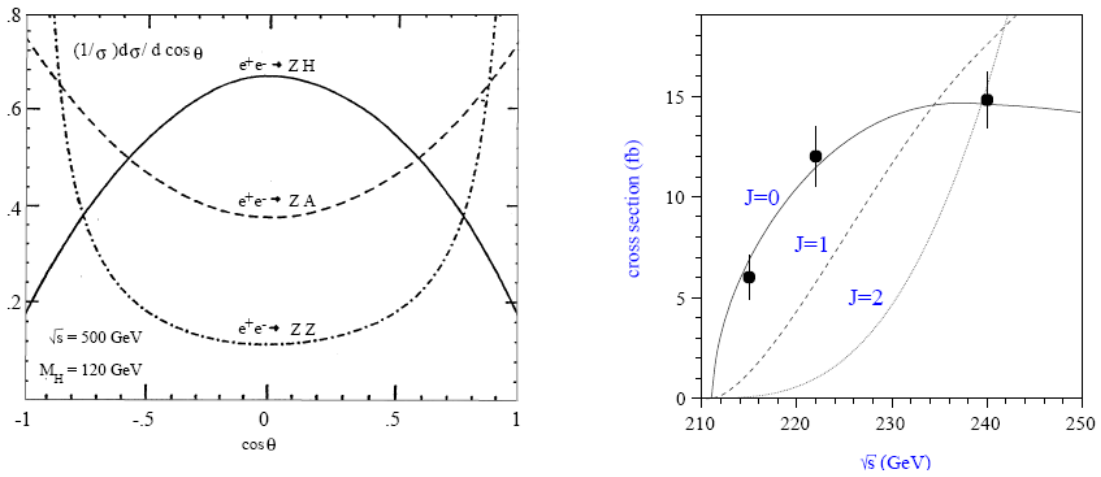

Figure 2.6 Measurement of the Higgs particle's parity [16] (for different parity we have different dσ/dcosθ) and spin [17] (by measure cross section at different $\sqrt{s}$) utilizing the $e^+e^- \to ZH$ channel

The spin of the Higgs particle may also be measured via the $e^+e^- \to ZH$ channel. For Higgs particles with different spins, the dependence of the cross-section on the center-of-mass energy differs. Thus by measuring the cross section at different center-of-mass energies, we are able to measure the spin of the Higgs particle. As shown in the right plot of Figure 2.6, for a 120 GeV Higgs boson, measurements of its cross section at three different center-of-mass energies (with 20fb^{-1} of integrated luminosity at each point) easily determine the spin of the Higgs particle [2, 16, 17].

2.4.2 Measurements of the decay branching ratios and total width

Measurements of Higgs boson decay branching ratios (equivalent to determining the coupling constants of other particles to the Higgs boson) are very important; these can be used to check the validity of the SM and to explore the nature of the Higgs particle. For example, by comparing the coupling constants of a Higgs particle to the positively-charged quarks (u, c, t) and the negatively charged quarks (d, s, b), we can check whether an observed Higgs boson is consistent with a SM Higgs boson or, if not, with one of the Higgs bosons expected within SUSY scenarios.

The measurements of the coupling constants between the Higgs boson and the W, Z gauge bosons are straight-forward. These may be determined by measuring the cross sections of the W-fusion and Higgs-strahlung processes. The precision of the coupling constants measurements could reach 1%-2% level [2].

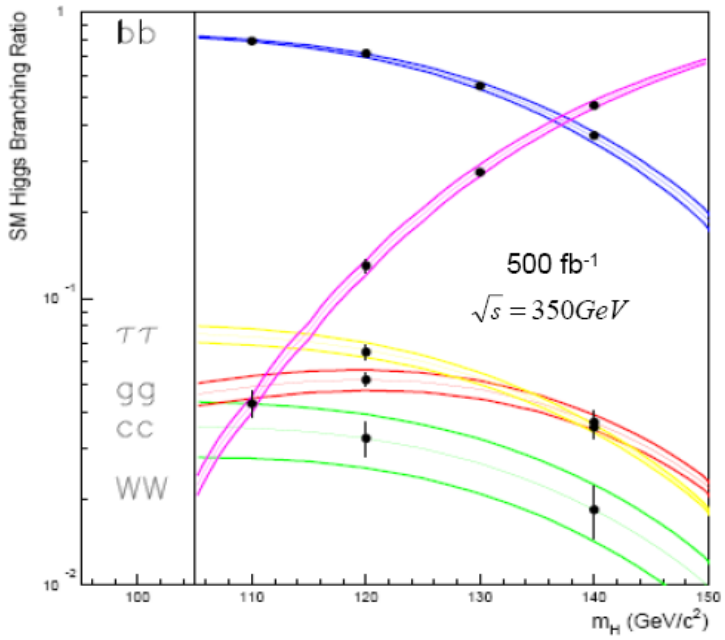

Figure 2.7 SM Higgs boson decay branching ratio [18]

A light Higgs boson is most likely to decay into a pair of b, c quarks or τ leptons. The corresponding branch ratios can be measured with efficient particle identification and jet flavor-tagging. In Figure 2.7, the expected Higgs boson decay branching ratios

are shown as functions of the Higgs boson's mass. The widths of the color-coded curve for each decay channel indicate the expected precision of the measurements [18].

Since the top quark is massive, the coupling constant of the Higgs particle to the top quark is the largest of all the Higgs-fermion couplings in the SM. If the Higgs particle is heavier than 350GeV, it is allowed to decay into a pair of top quarks, and then we could directly measure the coupling constant. For example, if the Higgs particle has a mass equal to 400GeV, assuming a center-of-mass energy of 800 GeV and an integrated luminosity of $1ab^{-1}$, then the coupling between the Higgs particle and the top quark could be measured to a relative precision of 4%[19].

The coupling of a light Higgs boson to the top quark could be measured through the $e^+e^- \to t\bar{t}H$ process (as show in the diagram to the right). The top quarks would each immediately decay into a W-boson and a b-quark, while a light Higgs boson, as we know, will dominantly decays into a pair of b quarks. So the final state for this process would predominantly be *WWbbbb* – if the W-boson decays into a pair of quarks, there may be eight jets in a single event. If the mass of the Higgs boson is larger than 150GeV, we need to consider the possibility of the Higgs particle decaying into a pair of W-bosons (perhaps with one W-boson off mass-shell), so that the final state would be *WWWWbb*. Combining together results from different Higgs boson decay channels and final states, for a Higgs boson mass within the range of 120GeV to 200GeV, the Higgs-top quark coupling measurement precision could reach the 10% level (assuming a center-of-mass energy equal to 800GeV and an integrated luminosity equal to $1ab^{-1}$), see Figure 2.8 [20].

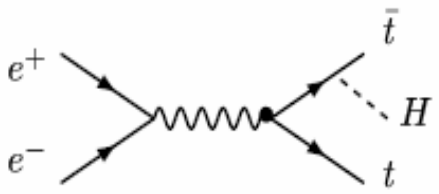

Because of the large number of Higgs boson-containing events expected at the ILC, the possibility of measuring the coupling between the Higgs boson and the μ lepton is now being considered.

With a center-of-mass energy equal to 230GeV and an integrated luminosity of $500fb^{-1}$, about 30 $H \to \mu^+\mu^-$ events are predicted by the SM, making this measurement feasible. A direct application of such a result would be the comparison of the H-μ coupling to the H-τ coupling, which could be checked for consistency with

SM predictions.

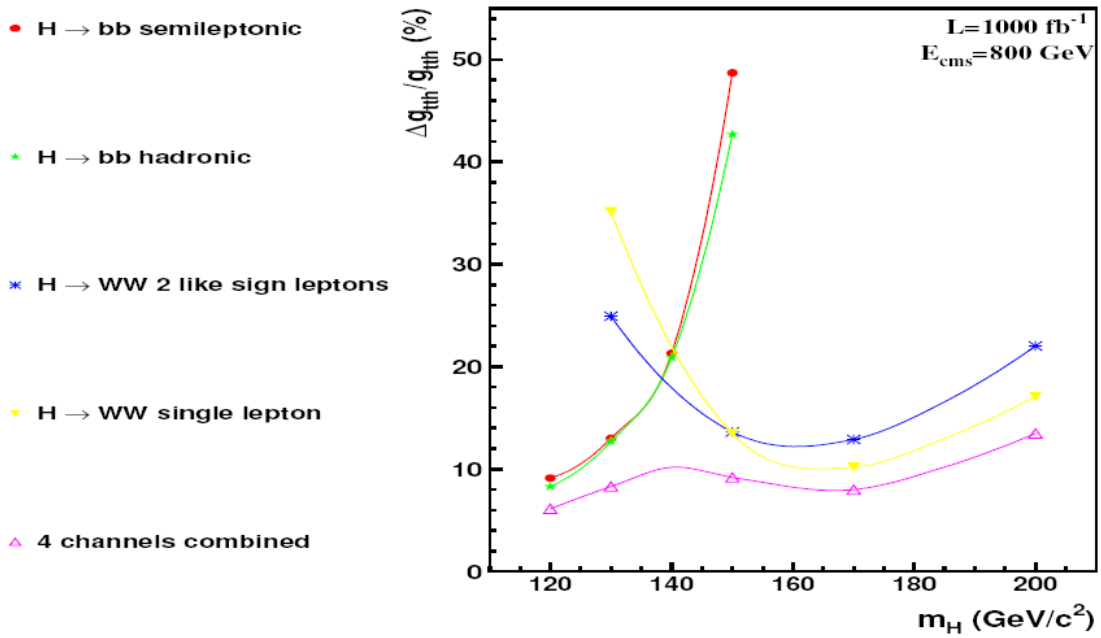

Figure 2.8 Measurement of coupling between the Higgs boson and the top quark [20]

For a Higgs particle with a mass > 200GeV, we can directly measure its width. For a light Higgs boson, the width value could be obtained by measuring the width for one of the Higgs boson's decay modes (usually $H \to WW^*$) and the corresponding branch ratio of the process [2].

In this section, we have systematically introduced the measurements of the coupling constants between the SM Higgs boson and other SM particles as well as the measurement of the Higgs particle's total width. In the next section, we will discuss the measurement of the Higgs boson's self-coupling, which is of essential importance in checking the validity of the SM.

2.4.3 Measurement of the Higgs boson's self-coupling

The measurement of the trilinear Higgs boson self-coupling (λ_{HHH}) constant will be the first non-trivial probe of the Higgs potential and probably the most decisive test of the Electroweak Symmetry Breaking (EWSB) mechanism[2]. This measurement could be performed using the double-Higgs-strahlung process ($e^+e^- \to HHZ$, see Figure 2.9). It is very hard to measure λ_{HHH} at the LHC; perhaps it will be possible at the proposed high-luminosity up-graduated version of the LHC, the VLHC [2].

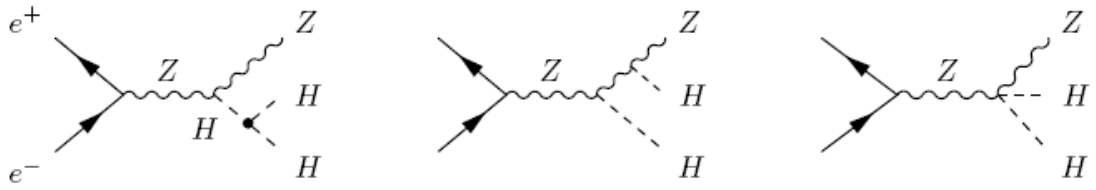

Figure 2.9 Feymann diagrams for the double-Higgs-strahlung process, only the diagram on the left is useful in measuring λ_{HHH} [2]

The double-Higgs-strahlung process requires a high center-of-mass energy; *i.e.*, 500GeV, 1TeV or even higher. Its cross section is on the order of 0.1fb, meaning we will collect roughly 100 events. Since a light Higgs boson (with a mass < 150GeV) will dominantly decay into a pair of b quarks, the final state of $e^+e^- \to HHZ$ process will most probably be $4b+2l$ or $4b+2q$. The backgrounds are mainly 4-jet or 6-jet events, which may arise from processes such as $e^+e^- \to t\bar{t}$, whose production rates at the ILC will be enormous. This means that in order to measure the trilinear Higgs-self-coupling, extremely efficient flavor-tagging will be essential along with very precise jet energy resolution capabilities. For a 120GeV SM Higgs particle, assuming a 500GeV center-of-mass energy and 1ab^{-1} of integrated luminosity, λ_{HHH} could be measured to a precision of 22% level [21, 22].

If the mass of the Higgs particle is large than 150 GeV, the Higgs particle will dominantly decay into a pair of W-bosons, so that the final states of the double-Higgs-strahlung process will be $4W+2l$ (10%) or $4W+2q$(70%) and also $4W+2\nu$(20%).

If the center-of-mass energy is higher than 500GeV, the process $e^+e^- \to HH\nu\nu$ (shown diagrammatically to the right), from which we could also obtain λ_{HHH}, becomes important. By combining the results from $e^+e^- \to HHZ$ and $e^+e^- \to HH\nu\nu$ processes together, assuming a Higgs boson with a mass between 100GeV and 200GeV, λ_{HHH} could be determined to within 13%-15% , see Figure 2.10[23] (with 1TeV center-of-mass energy and 1ab^{-1} of integrated luminosity).

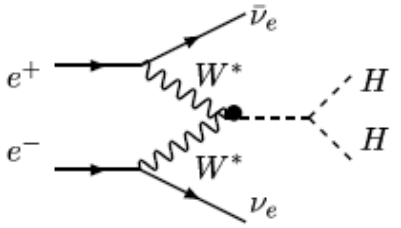

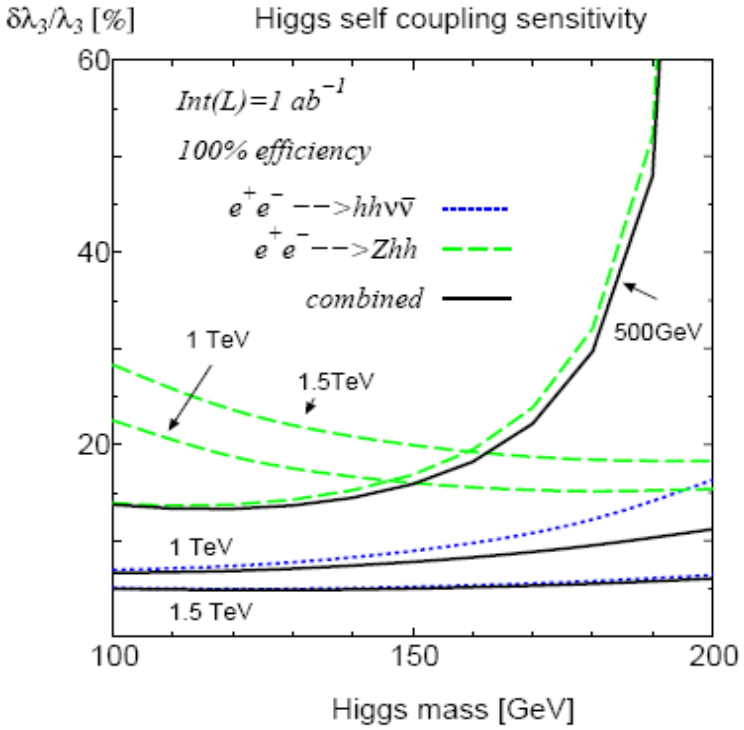

Figure 2.10 The precision of λ_{HHH} measurement versus mass of the Higgs boson [23]

2.5 Summary

In this chapter we have briefly introduced the Higgs physics at the ILC; *i.e.*, measurements of properties of the SM Higgs boson. These parameters include its mass, lifetime, spin, parity, couplings to other SM particles and the trilinear Higgs boson self-coupling (λ_{HHH}).

We have examined two methods useful in determining the Higgs boson mass at the ILC: the recoil mass method utilizing the $e^+e^- \to HZ \to H\mu\mu$ channel and the constraint fit method employed for hadronic final states of the $e^+e^- \to HZ$ process. The former performs better at low center-of-mass energies while the latter becomes important for higher center-of-mass energies. Assuming the mass of the Higgs boson to be 120GeV, and for a 230GeV center-of-mass energy with 500fb^{-1} of integrated luminosity, the first method enables the Higgs boson mass to be measured to a precision of 30-40 MeV. On the other hand, if the center-of-mass energy is 350 GeV, then the second method would allow us to achieve a mass measurement precision of 70 MeV.

The parity of the Higgs particle could be determined by studying the angular distribution of $e^+e^- \to HZ$ events. By measuring the cross section of the $e^+e^- \to HZ$ process at different center-of-mass energies, we could ascertain the spin of the Higgs particle. In the SM, the width (lifetime) of the Higgs particle is determined by its mass. If the mass is larger than 150 GeV, then the Higgs boson's width is wide enough to be measured directly; on the other hand, if the mass is smaller than 150 GeV, its total width could be calculated from the measurements of the partial width of one decay mode (usually $H \to WW^*$) and the corresponding branching ratio.

In the SM, the coupling of any other particle to the Higgs boson is proportional to the mass of the particle. Since the leading processes for Higgs particle production at the ILC are $e^+e^- \to HZ$ and $e^+e^- \to H\nu\nu$, the couplings of the Higgs boson to the Z, W bosons could be directly determined from respective measurements of these two processes, for which we should be able to easily reach precisions at the 1%-2% level. A light Higgs boson will mainly decay into a pair of b, c quarks or τ leptons, so the couplings of these

three fermion flavors to the Higgs boson can be determined with the support of effective jet flavor-tagging and particle identification, and the measured precisions could reach the 2%-10% level.

The situation concerning the measurement of the coupling of the Higgs particle to the top quark is a little more complex. Since the top quark has a huge mass, the Higgs particle needs to be at least as massive as 350 GeV to decay directly into a pair of top quarks, which would allow for a direct measurement of the top-Higgs coupling. Otherwise, if the Higgs boson is too light, we can determine the coupling via the $e^+e^- \to t\bar{t}H$ process – with a center-of-mass energy equal to 800GeV and an integrated luminosity of $1ab^{-1}$, the precision for determining the top-Higgs coupling via this channel could reach the 10% level for a Higgs boson with a mass between 120GeV and 200GeV.

Determining the value of the trilinear Higgs boson self-coupling is one of the most exciting challenges in the ILC physics. A measured value for this coupling will probably be the first non-trivial probe of the Higgs potential as well as the most decisive test of EWSB. With an integrated luminosity of $1ab^{-1}$ and a center-of-mass energy of 500GeV (1TeV), precision for the determination of the trilinear Higgs boson self-coupling could reach the 22% (15%) level using the double-Higgs-strahlung process (both $e^+e^- \to HHZ$ and $e^+e^- \to HHv\nu$ processes).

As we have discussed in this chapter, the ILC will have the capability to provide precise measurements for almost all SM Higgs boson properties if the Higgs boson's mass is below 1TeV. The ILC should also present a decisive test for the SM (and the EWSB mechanism). In Chapter 4, we will continue our discussion on the Higgs boson mass and cross section measurements via the $e^+e^- \to HZ \to H\mu\mu$ channel.

Chapter 3 Introduction to the ILC accelerator, detector and software

3.1 Introduction

As the next generation of linear collider, the ILC project is a great challenge to the current technique on accelerator and detector. As for the accelerator, it is required that [24]:

Continuously tunable center-of-mass energy from 200GeV to 500GeV, with the capability to be upgraded to 1TeV;

High luminosity with peak value as high as $2\times10^{34}cm^{-2}s^{-1}$, reaching an integrated luminosity of $500fb^{-1}$ in the first four years;

Polarized beam; more than 80% electron polarization and more than 60% positron polarization at the Interaction Point (IP);

An energy stability and precision of 0.1% level;

Capabilities of electron-electron and photon-photon collisions.

For the detector, it needs to have the capability of effectively identify the basic quanta (quark, lepton and Mediate Gauge bosons) and precisely measure their 4-momentum [25]. In other words, for the detector it requires:

Precise jet energy resolution;

Effective jet flavor tagging;

Very high precision on charged track momentum measurement (e, μ, π);

Full solid angle coverage.

In this chapter we give a brief introduction to the ILC accelerator, detector and its software system. Chapter 3.2 is the introduction to the current four ILC detector concepts, chapter 3.3 will mainly present the emergence of International Large Detector (ILD) group and the corresponding progress and organization on the

detector optimization study. Chapter 3.4 focuses on the detector model utilized in our full simulation study (LDC01_Sc) and gives corresponding parameters. Chapter 3.5 outlines the ILC accelerator and the beam-beam effect, and in chapter 3.6 we briefly present our software system, and it use the grid technique in the CALICE experiment. A short summary comes in chapter 3.7.

3.2 Current four ILC detector concepts

Four ILC detector concepts emerged from preliminary detector studies, the SiD, LDC, GLD and 4th [25]. In order to meet the requirement we mentioned in the introduction, these four concepts shares many patterns in common. For example:

- Full and hermetic solid angle coverage;
- Vertex detector supported with the silicon-strips pixels technique, providing the capability of precisely measure charged track and reconstruct the vertex – excellent heavy quark identification;
- Highly efficient tracking, aiming a charged particle momentum resolution of $\delta P / P^2 \approx 5 \times 10^{-5} / GeV^{-1}$;
- High magnetic field, with field strength from 3 Tesla to 5 Tesla;
- Putting the calorimetry system inside of the magnetic coil to ensure high precision jet energy measurement. For all the four concepts, the di-jet mass resolution could reach 3% level.

Of course, as four independent detector concepts, they also have many different patterns. Now we start to introduce them one by one.

3.2.1 The SiD concept

The SiD concept, as well as the LDC and GLD concepts, adopts the particle flow calorimeter, where highly segmented electromagnetic calorimeter (ECAL) and hadron calorimeter (HCAL) allow the separation and identification of energy deposition from different sources (charged track, photons and neutral hadrons).

For the SiD concept, highly pixilized silicon-tungsten ECAL and

multi-layered, highly segmented hadron calorimeter have been adopted. Since the calorimetry system is very expensive, the SiD concept utilizes the highest field solenoid (5 Tesla) of all the four concepts to reduce the cost. The SiD concept is illustrated in Figure 3.1[25]. Moving from small to large radii, the SiD baseline detector has the following components:

Vertex tracker: silicon pixel detector, beginning at radius of 1.4cm and extending to 6.1cm. It has 5 layers in the barrel region and 4 layers in each end cap, ensuring large solid angle coverage.

The main tracker consists of 5 layers of silicon mircostrip sensors, Each individual layer has only 0.8% X_0 (radiation length) thick. This is the most characteristic design in the SiD detector concept: for a charged track, the main tracker will provide a few spatial points but each point is measured with very high precision.

The ECAL begins at a radius of 1.27m and extends 29 X_0 deep. The ECAL is divided into 30 layers with silicon pixel sensors and tungsten absorber. The pixel area is about 14 mm^2 each. The HCAL follows the ECAL, begin at a radius of 1.41m. The HCAL is composed of 40 layers of Iron-RPC (Resistive Plate Chambers) structure. The RPC is fragmented into cells with 1 cm^2 area. The depth of the HCAL is four interaction lengths.

The 5-Tesla superconductive coil begins at radius 2.5m and extends to 3.3m. Outside the coil is the YOKE, with radius from 3.33m-6.45m. The YOKE provides the flux return and supports the muon system. The forward system consists of a luminosity calorimeter, a beam calorimeter (BeamCal) and a gamma calorimeter (GamCal), to measure the beam-strahlung pairs and gammas, which can provide robust complementary information and monitor the luminosity.

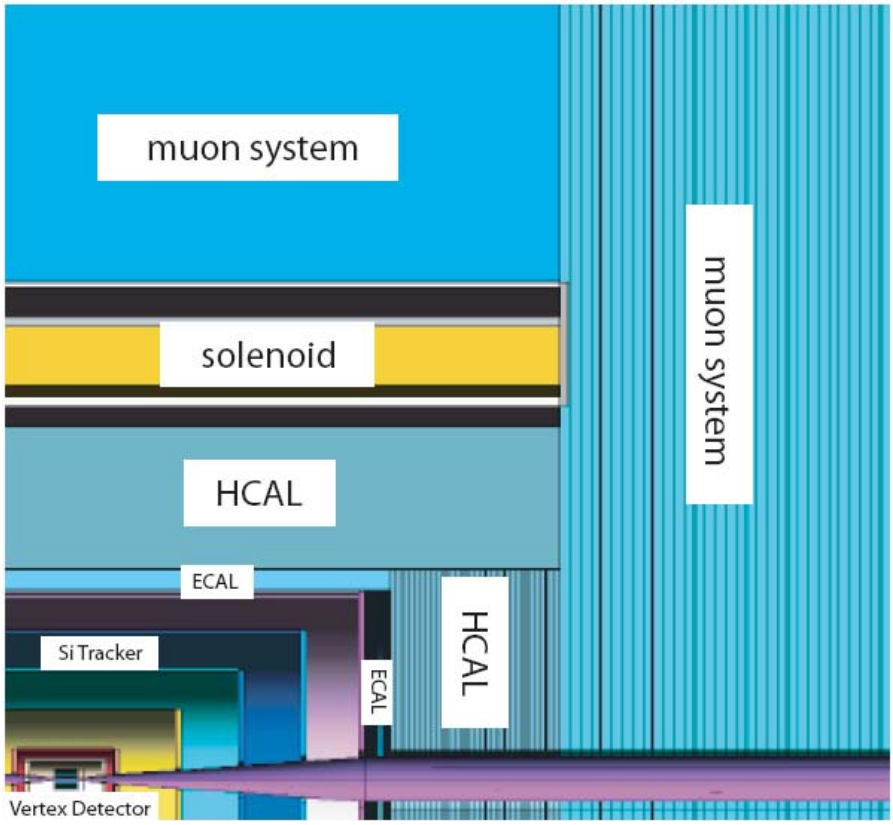

Figure 3.1 Illustration of a quadrant of the SiD concept[25]

3.2.2 The LDC concept

The LDC concept takes a very high precision and robust tracking system and a particle flow strategy based calorimetry system. The LDC concept utilizes a large volume of tracking chamber with 4 Tesla field strength and high granularity calorimetry system. The schematic view of one quarter of the LDC detector is shown in Figure 3.2 [25]. Moving from small to large radius, the LDC detector consists of those following components:

A five-layer pixel-vertex detector (VTX);

A system of silicon strip and pixel detectors beyond the VTX detector: In barrel region, there are 2 layer of silicon strip detector; and in the forward region there are 7 pairs of front tracking disks of silicon pixels and silicon strips. This provides tracking coverage to small polar angles.

The main tracker is a large volume of Time Projection Chamber (TPC), which provides as many as 200 precisely measured spatial points for a high energy charged track.

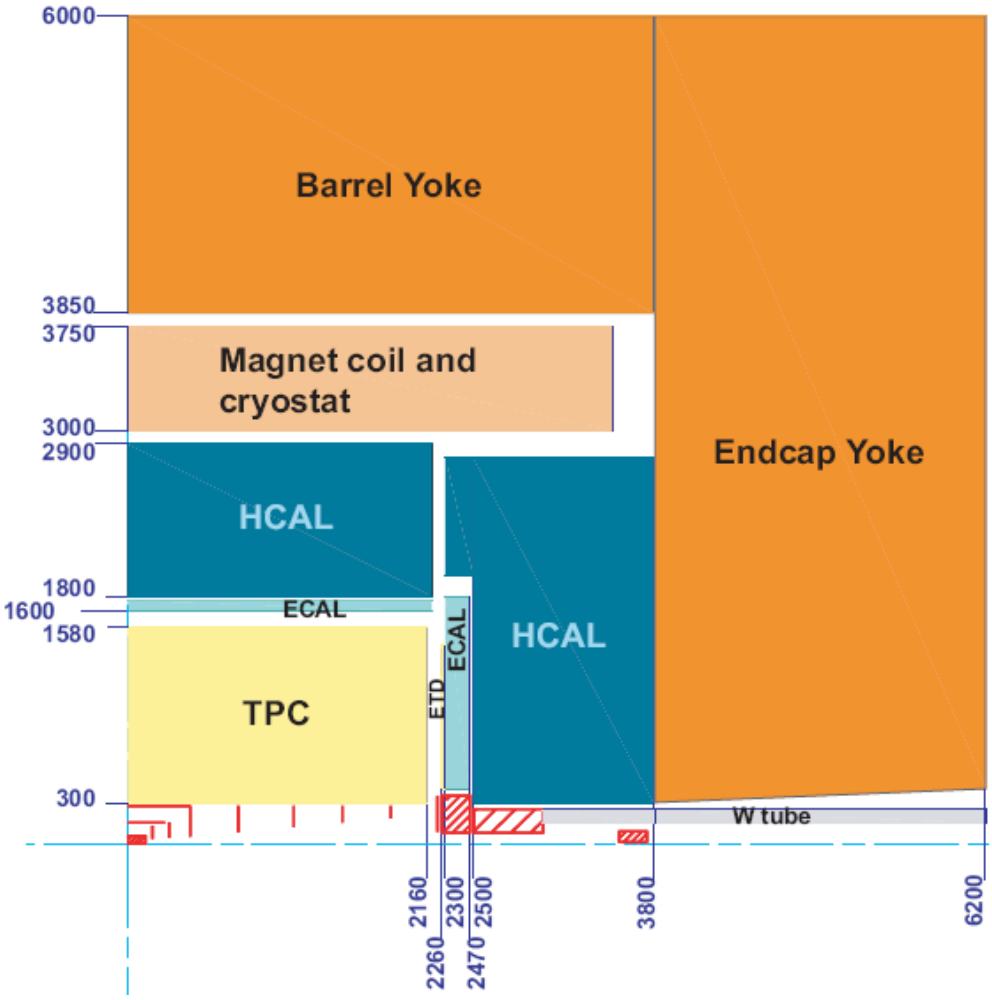

Figure 3.2 Schematic view of a quarter of the LDC detector [25]

In between the TPC and the ECAL, there exists a system of "linking" detector based on silicon strip technique. There is Silicon External Tracker (SET) in the barrel region and External Tracking Disk (ETD) in the endcap region. The SET and ETD are only available for some recent versions of the LDC concepts. In the concept utilized in our full simulation study, the LDC01_Sc has no SET or ETD subdetectors.

The ECAL consists of 30 layers of silicon (sensor) and tungsten

(absorber) structure. The ECAL has very high spatial granularity: the silicon sensor is segmented into 0.55cm×0.55cm cells on each layer (or 1cm×1cm cells in some early versions). The front ending chips are installed into the silicon sensor to save the space.

The HCAL consists of 40 layers of Iron-scintillator (or Iron-RPC) sandwich structure. The HCAL also has high spatial granularity, while the inner layer sensors are divided into 3cm×3cm cells (and 6cm×6cm or 12cm ×12cm for outer layers). This design is so called the Analog HCAL (AHCAL). There also exists another design of the HCAL sensor with extremely high spatial granularity: utilizing $1\times1cm^2$ cells, while for each electronic channel we use only one bit to record the information if this cell is hit or not. This design is called the Digital HCAL (DHCAL).

Outside the HCAL is the superconducting coil, which creates a 4-Tesla longitudinal B-field. The flux return system is also the YOKE, which acts as muon detector by interspersing some tracking detectors among the iron plates (for some early version, there is no muon detector in the YOKE).

In the forward region there also has a system of extremely radiation resistance calorimeters, to measure luminosity and to monitor the quality of the collision. This system consists of LumiCal, BCAL and LHCAL.

The LDC concept has integrated into ILD concept. See section 3.3.

3.2.3 The GLD concept

The GLD concept [25] has many things in common with LDC concept. Both concepts choose TPC as the main tracking system, both utilize high spatial granularity calorimetry system, which is optimized for the Particle Flow Algorithm (PFA).

In the GLD concept, the field strength is 3 Tesla, which is the smallest of the four concepts, at the meantime, it has the largest volume. The structure of GLD concept is illustrated in Figure 3.3.

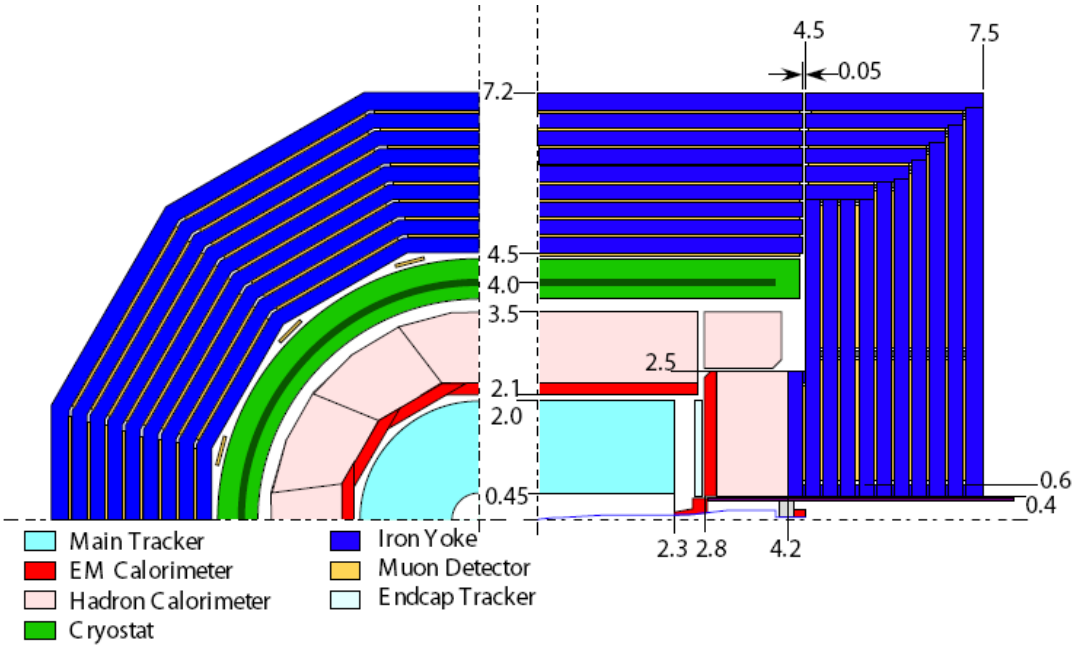

Figure 3.3 Schematic view of a quarter of the GLD concept[25]

From small to large radii, the GLD detector is composed of the following subdetectors;

A precise silicon micro vertex detector and a silicon inner tracker (SIT) in the barrel region and endcap tracker (ET) in the forward region;

A TPC as a large gaseous central tracker;

A highly segmented ECAL with tungsten-scintillator structure and a highly segmented HCAL with lead-scintillator sandwich structure;

Superconductive coil and YOKE system provide the magnetic field and the flux return. The YOKE also serves as the muon detector;

In the very forward region, there also have BCAL, FCAL.

The GLD concept has also integrated into ILD concept. See section 3.3.

3.2.4 The 4th concept

The 4th concept is a latercomer among all the four concepts and a very different design idea. The schematic view of 4th concept is illustrated in Figure 3.4[25]. Comparing to other concepts, there are two most characteristic features of the 4th concept.

First, the 4th concept chooses a dual-readout calorimetry system (Scintillator + Cerekov) instead of a calorimetry system with high spatial granularity, which has been used in all three other concepts.

Second, replace the massive YOKE flux return system with a secondary coil, which will generate a field in the opposite direction to the inner coil. The field strength is 3.5 Tesla in the inner part and roughly 1.5 Tesla in between the 2 coils. This design has two significant benefits:

1st, save a lot of space; in the forward region, this allows people to install the Final Focusing (FF) system much closer to the Interaction Point (IP), such that one could have more powerful focusing and achieve higher luminosity.

2nd, the muon detector (maybe also other stuffs in the future) could be installed in the space between this two magnetic coil, since there is no massive YOKE system, there multiple scattering caused by the materials will be highly reduced, and much better muon momentum resolution could be achieved.

From small to large radii, the 4th concept detector consists of following subdetectors:

A silicon pixel vertex detector;

A TPC;

Dual-readout crystal calorimetry system;

Superconductive coil system;

As a brief summary of the introduction to these 4 concepts, we list the main parameters of these 4 concepts in Table 3.1. All of those 4 concepts have been simulated in corresponding simulation software, the full simulation and

detector optimization study is undergoing to make sure they could achieve the corresponding goal of physics measurement.

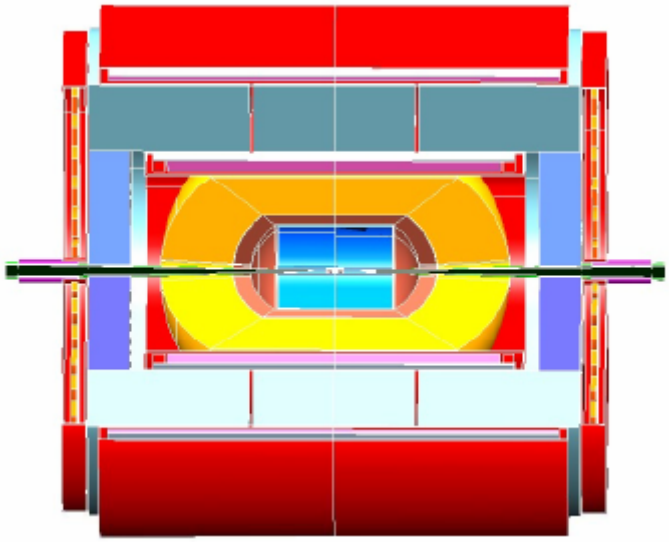

Figure 3.4 Schematic view of 4th Detector concept, Blue, TPC; Yellow, Calorimetry system; Red, the coil system [25]

Concept	Tracking Technology	Solenoidal Field (Tesla)	Radius, Length of Solenoidal (meters)	R_{VTX} (mm) R_{in} TPC	R_{ECAL} L_{ECAL} (meters)	R_{max}, 0.5L (meters)
GLD	TPC	3	4, 9.5	20	2.1, 2.8	7.65, 8.0
LDC	TPC	4	3, 6.6	15.5	1.58, 2.3	5.08, 5.60
SiD	Silicon	5	2.5, 5.5	14	1.27, 1.80	6.45, 5.89
4th	TPC	3.5/-1.5	3.0/5.5, 4.0/6.0	15	1.50, 2.40	5.50, 6.50

Table 3.1 Comparison of the main parameters of the 4 ILC detector concepts [25]. (For the 4th detector, there are both inner and out Solenoidal)

3.3 The emergence of the ILD concept group and current status of the ILD detector optimization study

Because the LDC and GLD concepts shall many things in common, it was decided to merge these two concepts into one, thus forming the ILD concept group[26]. The ILD group attempts to search for an optimized design of the ILC detector with the detector optimization study.

The first task for the ILD collaboration is to fix the baseline of the ILD detector, i.e. fix the basic geometry and parameters of the ILD detector. As shown in Table 3.2, two of the most important parameters are the radius of the main tracker and the magnetic field strength.

The detector optimization study, in one word, is to express the total physical measurement performance in terms of pivotal parameters of the detector. In the meaning while, the building cost could also be expressed as a function of these parameters – our task is to search for a group of these parameters, achieve the best physical performance and at the same time reduce the cost as much as possible.

	LDC		GLD	ILD ?
Tracker	TPC		TPC	TPC
R =	1.6 m		2.1 m	1.5–2.0 m ?
B =	4 T		3 T	3–4 T
ECAL	SiW		Scint	SiW or Scint
HCAL	Steel	RPC / Scint	Scint	yes

Table 3.2 The choice of basic parameters in the ILD concept[27]

The physical performance, for a subdetector, is the acceptance and efficiency of the sub detector, as well as the characteristic resolution accuracy – the accuracy of the energy, the spatial and the time measurement. In a further step, the physical performance can also be shown in terms of the accuracy of measurement of the position or 4-momentum of the track, the cluster and the vertex – the accuracy of the position and 4-momentum of the reconstructed particles. The final goal of high

energy physics experiment is to calculate some parameters from the physical model, like the mass and decay branching ratio of the Higgs particle, these parameters could be expressed as a function of the 4-momentum of the associated reconstructed particle. The most important questions about the detector R & D are: Could we measure these parameters? What accuracy could we achieve with current detector concepts?

In practical, the detector optimization is a complex process. It is very hard to express directly the physical performance in term of the characteristic parameters of the detector (while the cost estimation is usually much simpler). The Monte Carlo simulation is needed (or some fast simulation tools based on the experiment or full simulation result) to get the detector performance with certain detector parameters. In principle, we could use the simulation tools to scan over all the parameter spaces with certain step length – but this is almost impossible with our current computing capability: for the full simulation approximately we could simulate one event with one CPU in one minute – while we have many benchmark channels with at least 10k events each – these requirements on the computing resource could not be achieved even with the support of the grid technique. The simulation work needs to be organized in some priority (of those parameters), replace the whole parameter space scanning with a linear scanning, and save a lot of machine time.

In the detector optimization study the most important baseline parameters need to be fixed are the radius of the main tracker and the magnetic field strength. Take the jet energy resolution (with Particle Flow Algorithm) for example, Figure 3.5 shows that a large tracker radius gets better performance than a large magnetic field [27]. The optimization studies of other subdetectors are also undergoing.

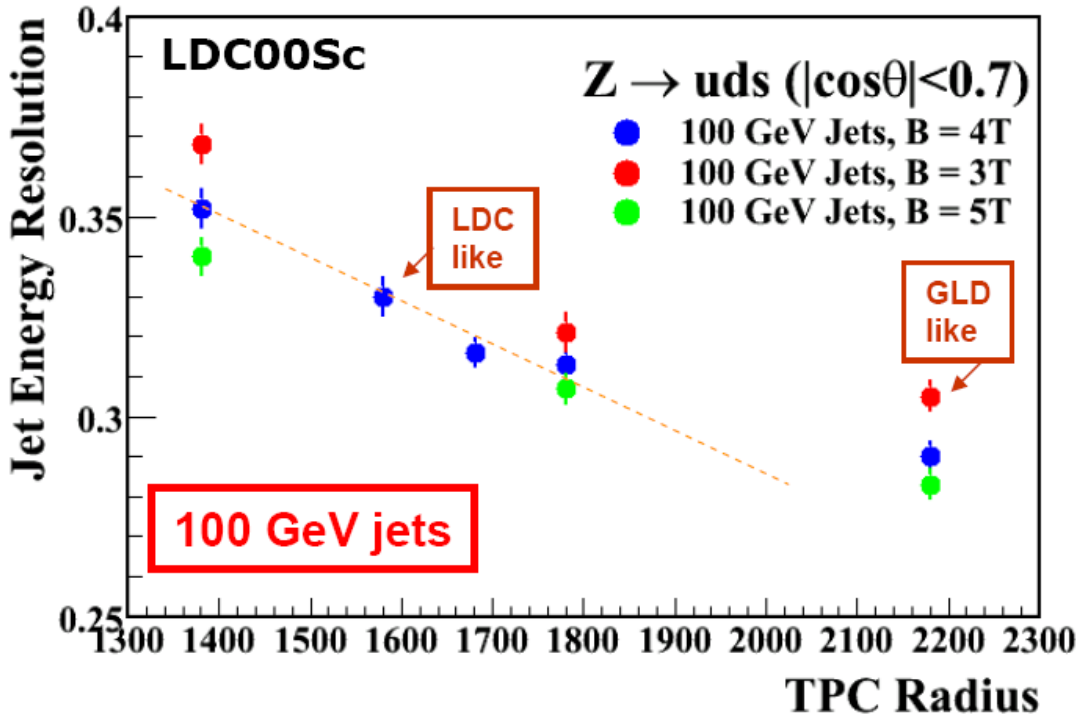

Figure 3.5 Accuracy of jet energy resolution vary with TPC radius and magnetic field strength [27]

The other strategy that the ILD optimization study adopts is to create an official database to avoid simple repetition of works. The grid computing and storing tools play an important role in this strategy. All the members of the ILD collaboration have access to the database. The database includes all the data generated or used in the full simulation study with given detector geometry, the generator file, the simulated detector hits, the reconstructed physical events, etc. And for the reconstructed physical events, there exist at least two versions, one minimal version which contains only the MC truth and the reconstructed particles information, and a maximal version which contains all the mediate collections in the simulation & reconstruction process. As we can imagine, the minimal version of reconstructed files is very convenient for the physics analysis. Figure 3.6 lists some of the benchmark processes to be simulated (with different experimental settings). Last but not least, those processes are not all the processes people interested in on the ILD detector, people are encouraged to add new valuable processes into this wishing list. One of the main works in this thesis, the measurement of the Higgs mass and cross section on $e^+e^- \to HZ \to H\mu\mu$ channel

could also be regarded as part of the ILD detector optimization study.

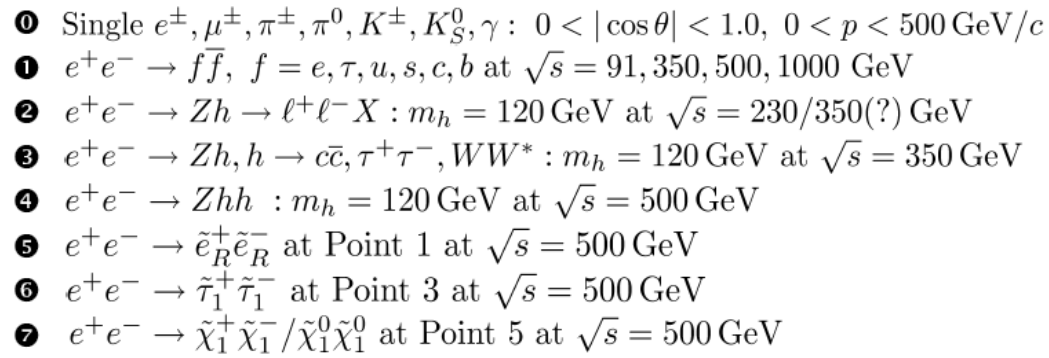

Figure 3.6 Benchmark processes in the ILD detector optimization study [27]

Until now, the ILD detector optimization study is well organized and progresses smoothly. The ILD Collaboration has a weekly phone meeting and keeps upgrading/maintaining the software system. We believe that in the foreseen future, we will have a more reliable, realistic and good performance detector concept.

3.4 Introduction to the LDC01_Sc concept

Our full simulation study on the Higgs mass measurement is based on the detector concept LDC01_Sc [28]. It is a minimal version of all the LDC detector concepts, which is slightly smaller in size than the original version LDC00 – for the TPC, there are only 184 layers instead of 200 layers (as in LDC00). There is no SET or ETD in between the TPC and the ECAL, and no μ detector installed in the YOKE. The sensor in the HCAL is scintillator (that's why we have a "Sc" in its name, an alternative choice is to use the RPC as the HCAL sensor). The structure of the LDC01_Sc is illustrated in Figure 3.7, from small to large radii, the LDC01_Sc consists of the following subdetectors:

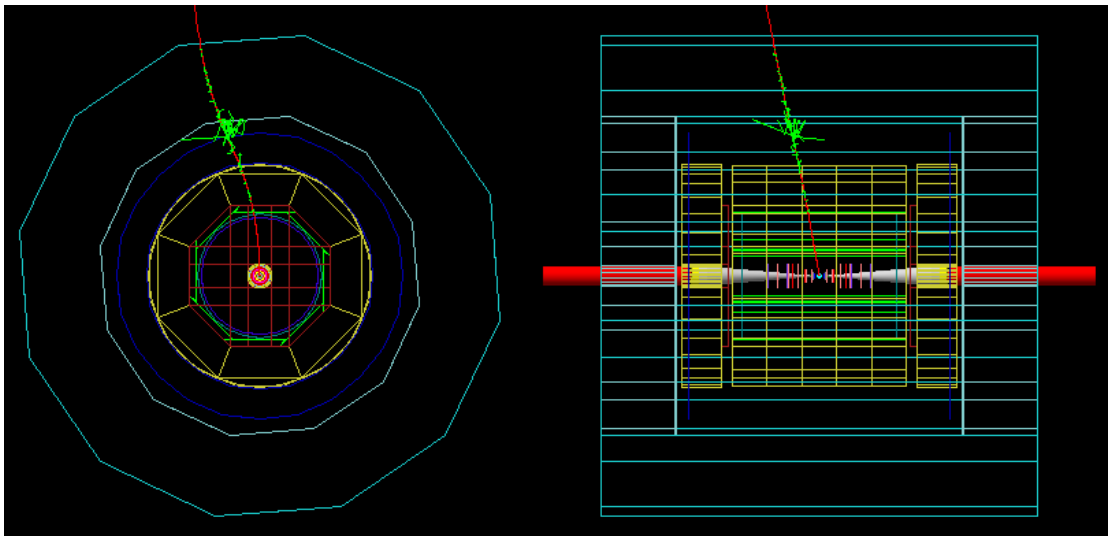

Figure 3.7 LDC01_Sc concept (with a 50GeV μ shot at 80° polar angle)

The tracking system: including a 5-layer silicon-pixel vertex detector (VTX), a 2-layer silicon inner tracker (SIT) and a 184-layer TPC. To ensure good track momentum resolution at small polar angle, there exist 7 pairs of front tracking disks based also on silicon strips pixel technique and the front chambers of TPC in the forward region.

The calorimetry system: an ECAL with silicon-tungsten sandwich structure. The ECAL is divided into 30 layers longitudinally, and segmented into 1cm×1cm cells transversely. The HCAL has Iron-Scintillator sandwich structure, and divided into 40 layers longitudinally, while transversely segmented into 3cm×3cm cells for inner layers, and 6cm×6cm or 12cm×12cm for the outer layers.

The coil and YOKE system: The superconductive coil creates a 4-Tesla longitudinal magnetic field in the inner part of the detector. No μ tracker has been installed into the YOKE: the YOKE only plays the rule of flux return.

Now let's discuss the tracking and calorimetry system.

3.4.1 Tracking System

The tracking system of LDC01_Sc concept is illustrated in Figure 3.8. It is divided into three parts, the inner tracking system (VTX + SIT, shown in Figure 3.9), the main tracking detector, (TPC, shown in Figure 3.10) and the front tracking system (FTD, shown in Figure 3.11). Now we give the relevant parameters of each subdetector.

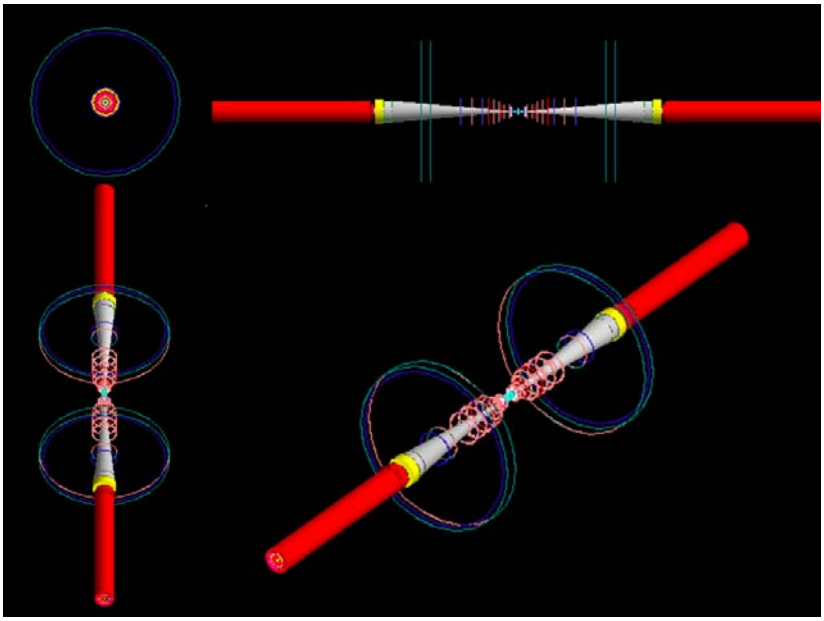

Figure 3.8 Tracking System of the LDC01_Sc concept

Inner tracking system (Figure 3.9):

Parameters of the VTX detector：

Number of layers: 5

Radius of each layer: 15.5mm, 27.0mm, 38.0mm, 49.0mm, 60.0mm

Length of each layer: 50.0mm, 125.0mm, 125.0mm, 125.0mm, 125.0mm

Accuracy of spatial resolution: $\delta R_{\varphi} = 4\mu m$， $\delta R_{Z} = 4\mu m$

Parameters of the SIT detector：

Number of layers: 2

Radius of each layer: 160.0mm, 300.0mm

Length of each layer: 380.0mm, 660.0mm

Accuracy of spatial resolution: $\delta R_{\varphi} = 10\mu m$， $\delta R_{Z} = 10\mu m$

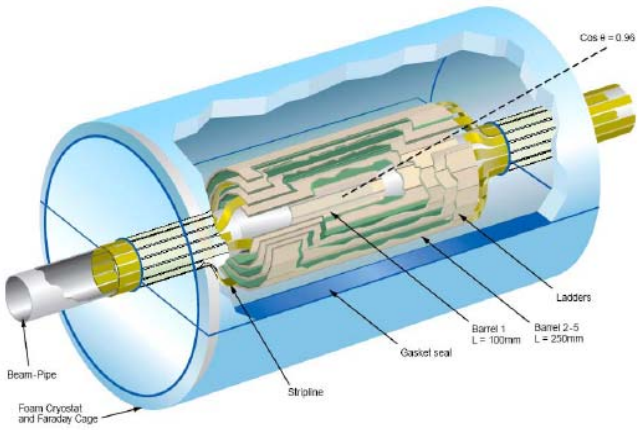

Figure 3.9 Inner tracking system of LDC01_Sc concept

TPC, the main tracking detector (Figure 3.10)

Parameters of the TPC detector:

Number of layers (Transverse number of pixels): 184

Inner/outer radius: 305mm/1580mm；

Maximal drift length: 1970mm；

Magnetic field strength: 4 Tesla

Spatial resolution for each point:

$\delta R_{\varphi} = \sqrt{66 \times 66 + 4 \times L_{drift}} = 66 \sim 95\mu m$， $\delta R_{Z} = 500\mu m$

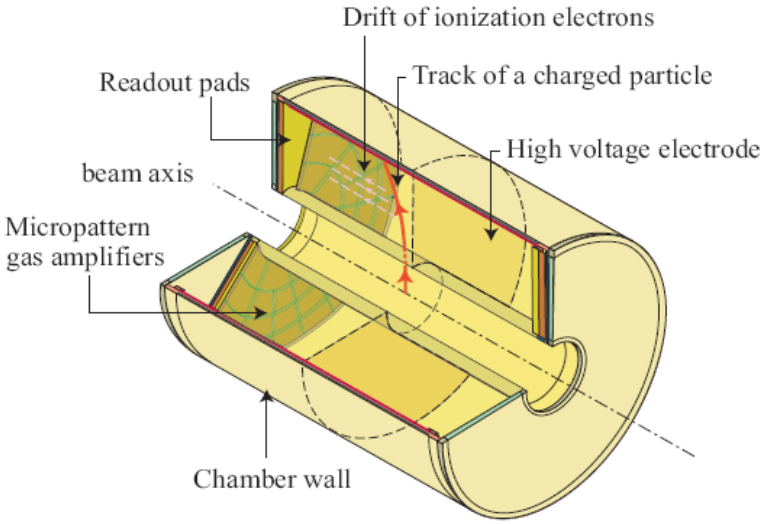

Figure 3.10 illustration of the structure of TPC

Front tracking system: 7 pairs of front tracking disks, FTD

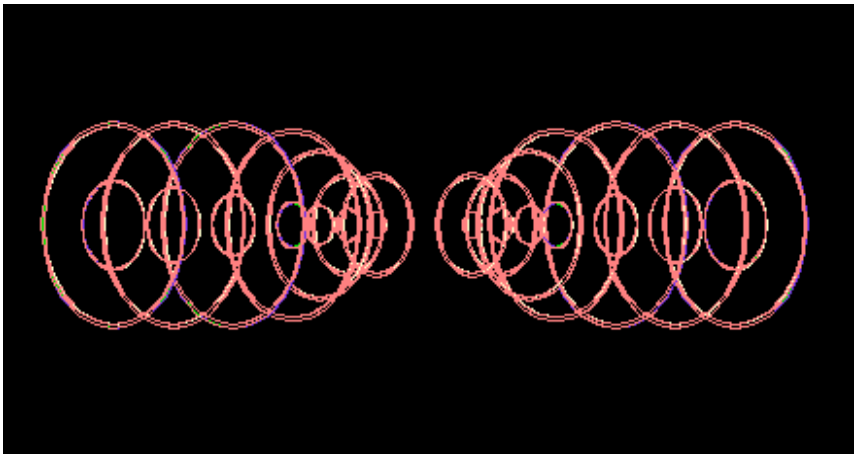

Figure 3.11 illustration of the front tracking system

Number of FTD pairs: 7

Z coordinates of each FTD (mm, take the value of one side since the structure is symmetrical):

200.0, 320.0, 440.0, 550.0, 800.0, 1050.0, 1300.0

Inner/outer radius for each FTD (mm):

Inner radius: 38.0, 48.0, 59.0, 68.0, 90.0, 111.0, 132.0

Outer radius: 140.0, 140.0, 210.0, 270.0, 290.0, 290.0, 290.0

FTD thickness: 0.3mm

Accuracy of spatial resolution:

$\delta R_{\varphi} = 10 \mu m \quad \delta R_{Z} = 100 \mu m$

LDC01_Sc tracking system has good spatial resolution and a large coverage of the solid angle, which ensures good momentum resolution for charged particles with polar angle in a large range. Now let's discuss the error on μ momentum measurement.

3.4.2 The μ momentum measurement accuracy and the fast simulation tool

The error on Higgs mass measurement could be expressed as a function of the error on the μ momentum measurement (see formula 3.1), which could be studied with the simulation software (MOKKA). So when knowing the error of the μ momentum measurement, we are able to predict the error on the Higgs mass measurement, and by convoluting the error to the MC truth, we can get the expected spectrum after reconstruction. In our analysis, we developed a fast simulation package, and the result is comparable with the full simulation result.

We use the particle gun to shoot a μ particle into the detector with different energies and polar angles. 10 energies (10GeV – 100GeV, with step length 10GeV) and 7 polar angles (10^{o}, 15^{o}, 20^{o}, 30^{o}, 40^{o}, 60^{o}, 80^{o}) have been scanned, in total 70 simulated data files with 10k statistics each were generated. The corresponding accuracy of the μ momentum measurement (δ(1/P)) has been summarized in Figure 3.12.

It is shown in Figure 3.12 that smaller δ(1/P) achieved with larger μ

energy, since the perturbation from multiple scattering goes relatively smaller at higher energy. When the polar angle is smaller than 40°, the track could not hit all the 184 layers in the TPC (the condition for an energetic enough track to hit all the TPC layers is its polar angle θ should satisfy θ>arctan(1580/1970)~38.7°), and the momentum resolution gets worse when we move to smaller polar angle. The best momentum resolution is achieved at about 40° polar angle, because, first, the track hit all the TPC layers; second, the TPC spatial resolution goes worse when you have longer drift distance; also there is a sin(θ) factor in the track momentum resolution formula (δ(1/P)=δ(1/Pt)sin(θ)). With the LDC01_Sc concept the overall momentum resolution reaches the goal of $\delta P / P^2 \approx 5 \times 10^{-5} / GeV^{-1}$.

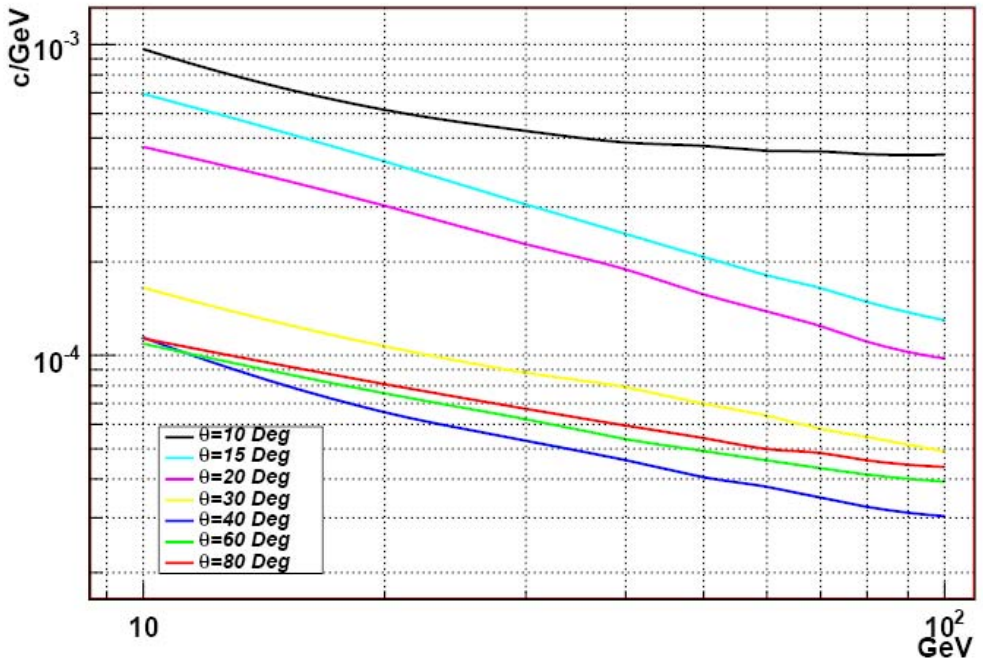

Figure 3.12 Accuracy of μ momentum as a function of energy and different polar angles

Formula 3.1 shows the relation between the error on the Higgs recoil mass and the error on the μ momentum. Here E is the beam energy, p_1 and p_2 are the momenta of the two muons. $k(p_1)$ and $k(p_2)$ are the corresponding

momenta measurement constants ($\delta p / p^2 = k(p)$).

$$\delta m_H^2 = \sqrt{[(4Ep_1 - m_Z^2)p_1 k(p_1)]^2 + [(4Ep_2 - m_Z^2)p_2 k(p_2)]^2} \qquad (3.1)$$

For a μ with an arbitrary momentum and angle, the expected accuracy on the momentum resolution could be calculated with the interpolation method (knowing the momentum resolution of the four nearest points). Then we could calculate the expected error on the Higgs recoil mass measurement with above formula. With this idea a fast simulation software package is developed, it reads in the μ momentum truth from the generator file, calculates the expected error on the Higgs mass measurement, and convolutes the expected error to the true value of the Higgs recoil mass.

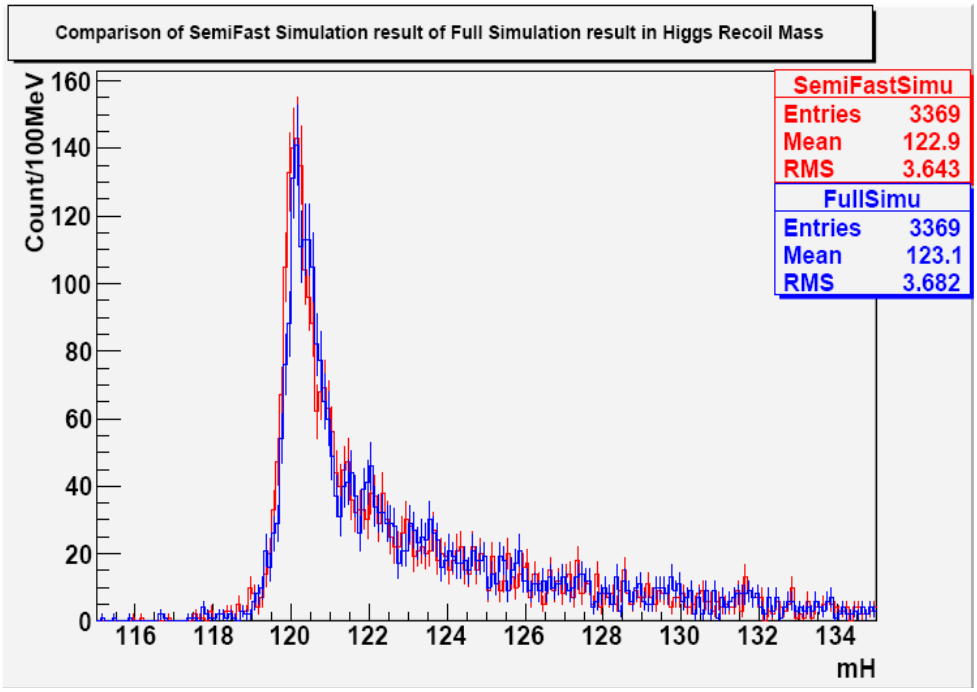

Figure 3.13 Comparison of Higgs recoil mass spectrum between the full simulation and fast simulation

Figure 3.13 shows that the fast simulation (red color plot) agrees nicely with the full simulation result (blue color plot). This fast simulation tool has

been applied in our beam parameter optimization study, see chapter 4.6. This study is also a direct check on the tracking system performance. Now let's go back to the calorimetry system of the LDC01_Sc concept.

3.4.3 The calorimetry system

The LDC01_Sc detector concept adopts the high spatial granularity calorimetry system, with silicon-tungsten sandwich structure ECAL and Iron-Scintillator structure HCAL [28]. Figure 3.14 shows the calorimeter structure of the LDC01_Sc, here the ECAL in blue and HCAL in green.

The ECAL barrel region is organized with octagon structure, the inner radius is 1600mm and the Z coordinate of the most outside layer is 2199.5mm. Transversely the silicon sensors are divided into 1cm×1cm cells, and longitudinally the ECAL is divided into 30 layers. For the first 20 layers, the absorber is 2.1mm thick tungsten, while for the last 10 layers, the thickness of absorber increase to 4.2mm. The distance between each sensor and absorber is assumed to be 1.5mm, so the total longitudinal thickness is 129mm: equivalent to 25 radiation lengths.

The ECAL end caps have an inner radius of 200mm and an outer radius of 1771mm. The Z coordinate for the inner layer is 2299.5mm, the micro structure is the same as the ECAL barrel region, i.e. 1cm×1cm cells and 30 layers in Z direction.

There are in total over 20 million channels of electronics in the ECAL. To save the space and avoid to the massive cables system, the front-ending electronics are installed inside the sensor layers of the ECAL, while the result from the CALICE test beam experiment confirmed the feasibility of this design [29].

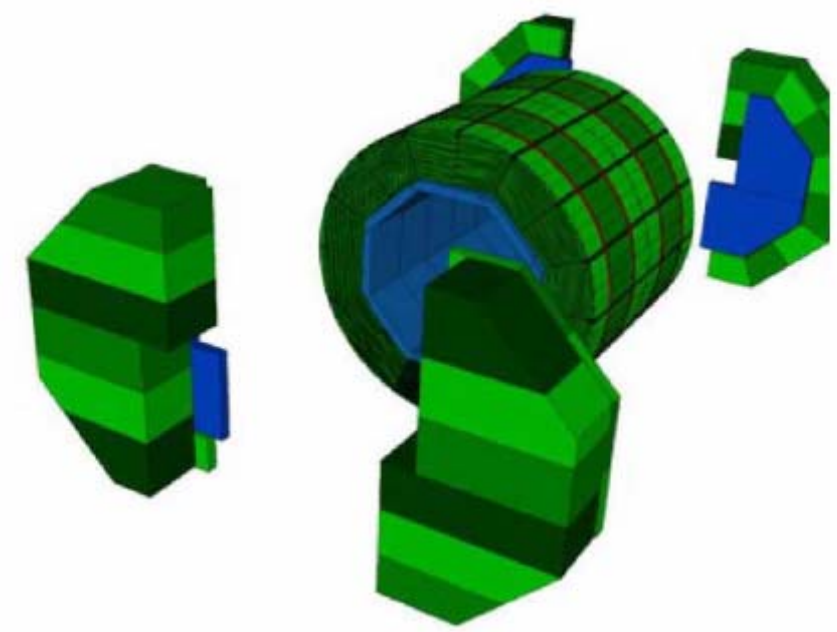

Figure 3.14 The calorimetry system in the LDC concept

Same as the ECAL, the HCAL also has high spatial granularity. The HCAL was divided into 40 layers in the longitudinal direction and each layer has a thickness of 24.5mm, including an 18mm thick iron absorber. The sensor is segmented into 3cm× 3cm cells for the inner layer. In the barrel region, the inner radius for the HCAL is 1800mm, while the Z coordinate is 2201.5mm. And on the end caps, the inner radius is 300mm, while the outer radius is 2800mm. The total number of electronic channels on the HCAL is 4.5 million.

We stop our introduction to the ILC detectors here. In the next section, we will introduce the accelerator.

3.5 Introduction to the ILC accelerator and beam parameters

3.5.1 The ILC accelerator

The ILC accelerator has a designed length of 31 km, it will be installed in the tunnels located over hundreds of meters underground. With the support of laser and cryogenic techniques, the ILC accelerator could provide electron and positron beams with power as high as 420 MW. The structure of the ILC accelerator is illustrated in figure 3.15, including the electron/positron source, the damping ring, the main Linac, the Beam Delivery System (BDS) and the Final Focusing system (FF). For the ILC project it is planned to have two detectors to cross check the measurement result[24]. Since there is only one interaction point for the linear collider, it is planned to stop the machine and replace one detector with another after a certain period of data taking. This is so called the push-pull system.

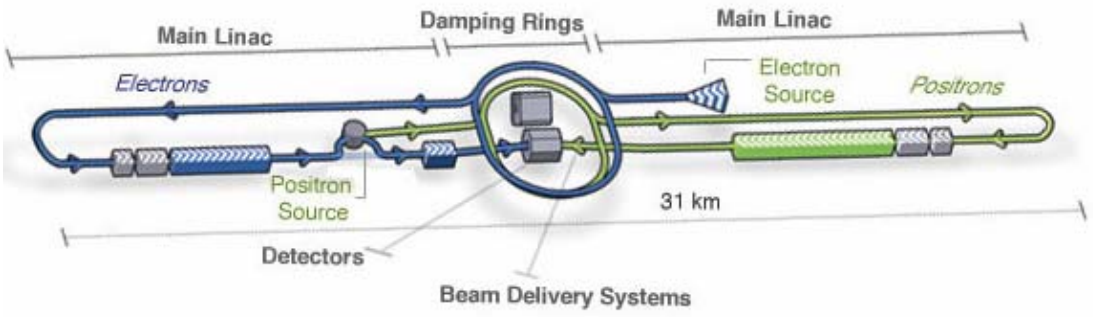

Figure 3.15 Schematic view of the ILC [1]

Now following the time sequence of accelerating the electron/positron, we give a short introduction to each part of the accelerator here.

The electron source consists of two independent DC gun. By illuminating laser into the photocathode in the DC gun the electron source could generate highly polarized electron beam. The electron beam will first be accelerated to 76MeV in a normal-conducting structure (which also bunch the electron beam), then delivered to a super-conducting linac and accelerated to 5GeV. After the spin rotation in superconducting solenoids, the beam is injected into

the damping ring. The damping ring has a total length of 6.7km, and could largely reduce the beam emittance. After the damping ring, the beam is delivered to the main linac by the Ring to the Main Linac (RTML) system. At the same time, the RTML system compresses the beam bunch length, and accelerates the beam from 5GeV to 13-15GeV. The electron beam will be accelerated to 250GeV by the main linac and delivered to the interaction point through the BDS system. The FF system will greatly compress the beam size to achieve high luminosity. There is a 14mrad angle between the main linac of electron and positron, making it easier to dump the beams after the collision.

A small episode happens when the electron beam has been accelerated to 150GeV. The 150GeV electron beam is delivered to a Helical Undulator, generate the free electron laser. Then the electron beam (with energy about 147GeV) is transported back into the main linac and accelerated to the interaction point. The free electron laser (with photon energy ~ 10MeV) will hit onto a Ti-alloy target about 500 meters downstream, producing a beam of electron-positron pairs. This beam is then accelerated to 150MeV with a normal conductive L-band RF, while the electrons and photons are separated from the positrons with a solenoid-focusing capture system and then dumped. The positron beam is then accelerated with 2 L-band RF to 5GeV and then transported to the damping ring. The positron source is shown in figure 3.16.

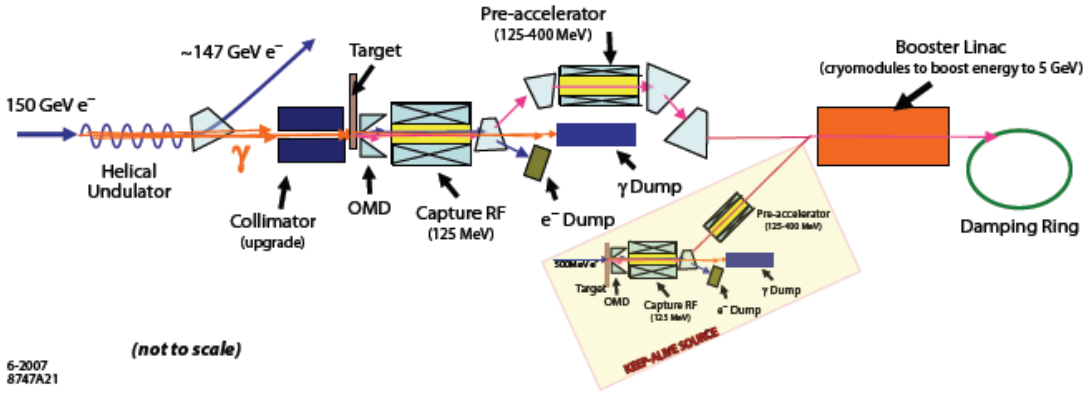

Figure 3.16 Positron source of the ILC [24]

The 9-Cell RF cavities (Figure 3.17) constructed with pure niobium material play a central role in the beam acceleration. Its working frequency is 1.3GHz, the microwave is injected into the cavity and creates extremely strong electro field (34.5MV/m). The RF cavities are supposed to work with 2K temperature (requirement from super conductive) so it is totally embedded in the liquid helium shower.

Figure 3.17 9-Cell RF cavities [24]

The main linac is constructed with 37.956 meter long RF units (Figure 3.18), each consists of three SCRF cryomodules and has in total 26 nine-cell cavities. Each RF unit has an independent RF source, which includes a high-voltage (120 kV) modulator, a 10 MW multi-beam klystron and a waveguide system. The main linac for the positron beam has 278 RF units, while there are 282 RF units for the electron main linac: since the electron beam loses about 3GeV energy in the positron source.

According to the RDR, the main linac components are located in two paralleled tunnels, an accelerator tunnel and a service tunnel, each of which has an interior diameter of 4.5 meters (Figure 3.19). The RF source is housed mainly in the service tunnel to facilitate the maintenance and limit radiation exposure. The tunnels are located several hundreds meters underground.

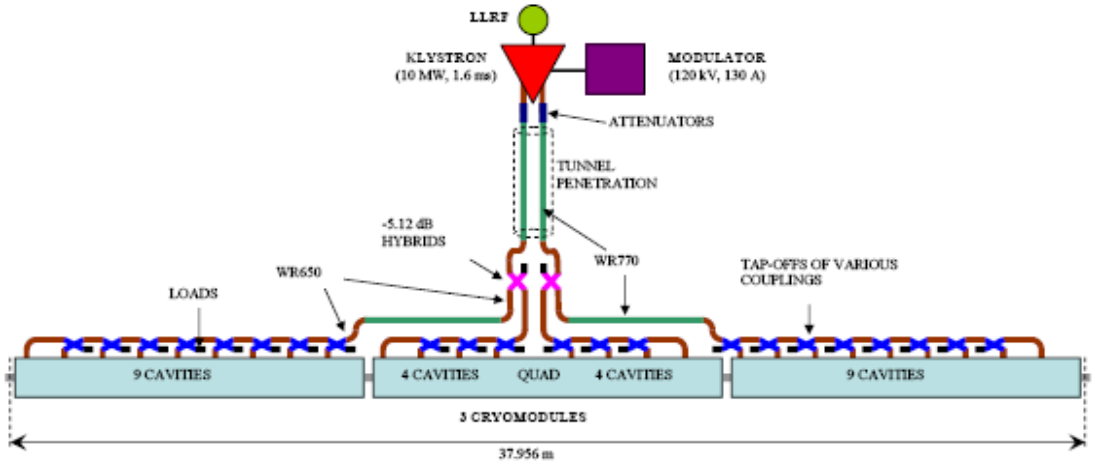

Figure 3.18 The RF Unit of the ILC linac[24]

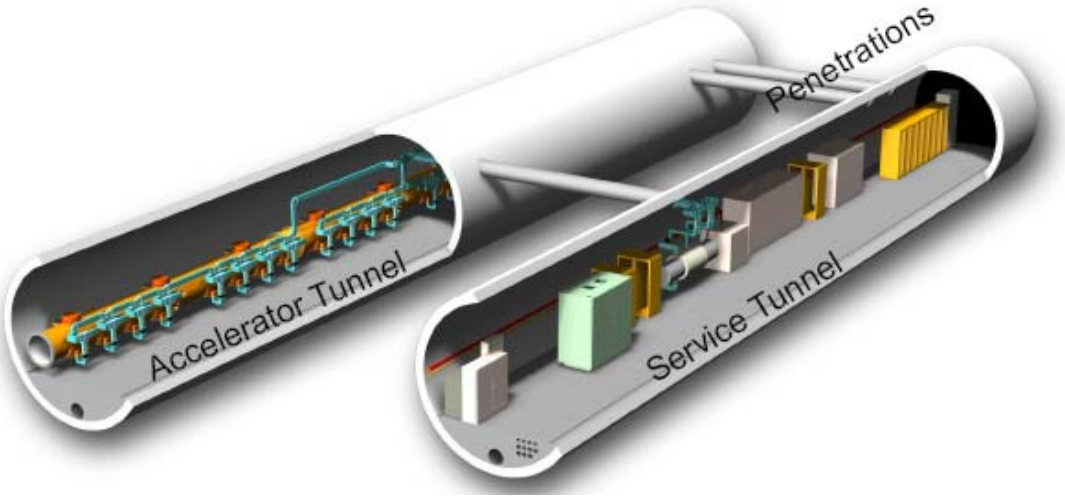

Figure 3.19 Cutaway view of the linac tunnels [24]

3.5.2 The Beam parameters and the beam-beam effects

When beams collide at the interaction point a mixture of classical and quantum physics effects occur there [30]. For example:

Bunches are deformed by the electromagnetic attraction;

Synchrotron radiation caused by the high beam-beam filed: beamstrahlung;

Secondary background, minijets; $\mathbf{e^+e^-} \rightarrow \gamma\gamma \rightarrow \mathbf{e^+e^-/qq}$

Depolarization effect of electron/positron;

These effects certainly affect our measurement. The most important effect is the beamstrahlung effect, which will cause about 3% of the energy loss at the ILC. To achieve good measurement accuracy, we need to find out a set of beam parameters, which simultaneously achieves high luminosity and low beamstrahlung.

Parameter	Symbol/Units	Nominal	Low N	Large Y	Low P
Repetition rate	f_{rep} (Hz)	5	5	5	5
Number of particles per bunch	N (10^{10})	2	1	2	2
Number of bunches per pulse	n_b	2625	5120	2625	1320
Bunch interval in the Main Linac	t_b (ns)	369.2	189.2	369.2	480.0
in units of RF buckets		480	246	480	624
Average current in the Main Linac	I_{ave} (mA)	9.0	9.0	9.0	6.8
Normalized emittance at IP	$\gamma\epsilon_x^*$ (mm·mrad)	10	10	10	10
Normalized emittance at IP	$\gamma\epsilon_y^*$ (mm·mrad)	0.04	0.03	0.08	0.036
Beta function at IP	β_x^* (mm)	20	11	11	11
Beta function at IP	β_y^* (mm)	0.4	0.2	0.6	0.2
R.m.s. beam size at IP	σ_x^* (nm)	639	474	474	474
R.m.s. beam size at IP	σ_y^* (nm)	5.7	3.5	9.9	3.8
R.m.s. bunch length	σ_z (μm)	300	200	500	200
Disruption parameter	D_x	0.17	0.11	0.52	0.21
Disruption parameter	D_y	19.4	14.6	24.9	26.1
Beamstrahlung parameter	Υ_{ave}	0.048	0.050	0.038	0.097
Energy loss by beamstrahlung	δ_{BS}	0.024	0.017	0.027	0.055
Number of beamstrahlung photons	n_γ	1.32	0.91	1.77	1.72
Luminosity enhancement factor	H_D	1.71	1.48	2.18	1.64
Geometric luminosity	$\mathcal{L}_{geo}$ $10^{34}/\mathrm{cm}^2/\mathrm{s}$	1.20	1.35	0.94	1.21
Luminosity	$\mathcal{L}$ $10^{34}/\mathrm{cm}^2/\mathrm{s}$	2	2	2	2

Table 3.3 Nominal beam parameters at the ILC [24]

Table 3.3 shows the nominal beam parameters at 500GeV center-of-mass energy at the ILC. In the Z direction, the beam particles are formed into bunches and then grouped into bunch trains. For the nominal beam parameter, a bunch consists of 2×10^{10} (N) particles and has a length of 300 μm near the interaction point. The distance between bunches is 110.76 meters (369.2ns, t_b). 2625 (n_b) bunches form a bunch train, which has a length of 290.7km (equivalent to ~1ms in time). The frequency of the bunch train is 5Hz (f_r), means that there is 200ms distance between bunch trains.

With the above information, we can easily calculate the beam current at the ILC:

$$I = 2\frac{Nf_r n_b F}{N_A} = 2*\frac{2*10^{10}*5*2625*96500}{6.023*10^{23}} = 0.84mA$$

.

The power of the electron and position beams is 420MW for 500GeV center-of-mass energy. As we mentioned in the accelerator chapter, the main linac consists of 560 RF sources (10MW each), so the total energy transition efficiency for the main linac is roughly 7-8%.

The basic parameters to describe the geometry of bunch are the emittance and beta function in both X and Y direction. The emittance has a dimension of meter, which means the area of angular-position phase space the particles in a bunch have occupied (1 σ). So lower emittance means the bunch particles are more concentrated in the phase space. A more straightforward description for the spatial concentration of bunch particles is σ_x、σ_y, which means the geometrical size of the bunch. There has a simple relation with the beta function and emittance: $\sigma \propto \sqrt{\varepsilon\beta/\gamma}$.

Disruption describes the effect of the EM field surrounding each bunch during the collision: each beam acting as a thin focusing lens and changing the opposite beam trajectory. Disruption is determined by σ_x、σ_y in the following way [30]:

$$D_{x,y} \equiv \frac{2Nr_e\sigma_z}{\gamma\sigma_{x,y}(\sigma_x+\sigma_y)}$$

Similar as the disruption, the geometrical luminosity of collider is also determined by σ_x and σ_y. We have:

$$\mathcal{L}_{geo} = \frac{N^2}{4\pi\sigma_x\sigma_y} f_r n_b$$

The actual luminosity of collider is equal to its geometrical luminosity multiplied by a factor ηH_D:

$$\mathcal{L} = \mathcal{L}_{geo} H_D \eta = \frac{N^2}{4\pi\sigma_x\sigma_y} f_r n_b H_D \eta$$

Here η refers to the luminosity reduction caused by the wake field, it increases with the center-of-mass energy. For 500GeV nominal beam the wake field reduction is very small and the value of η is about 1 (and for 230GeV center-of-mass energy we used in the full simulation, $\eta \sim 0.78$). H_D describes the beam-beam self-focusing effect, for electron-position collider, H_D is always larger than 1: we have $H_D = 1.71$ for the nominal beam.

The beamstrahlung effect is illustrated in Figure 3.20. When two bunches collide, the direction of charged particles are curved and cause the synchrotron radiation[30]. The beamstrahlung effect will result in the emittion of energetic photons and the energy/luminosity loss at the interaction point. For 500GeV nominal beam, 1.32 photons are emitted for each electron/positron in the beam, and in total 2.2% beam energies are lost through the beamstrahlung effect.

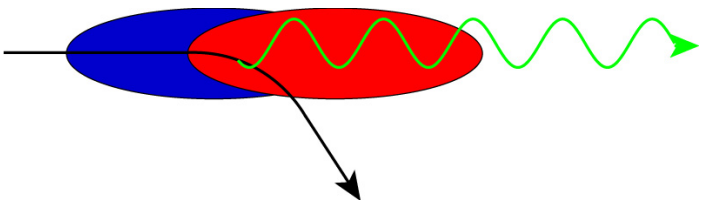

Figure 3.20 Illustration of the beamstrahlung effect [30]

The beamstrahlung parameter Y is introduced to describe the strength of beamstrahlung effect, which has the physical meaning of the field strength seen by the beam particle at its rest frame.

$$\Upsilon_{ave} \approx \frac{5}{6} \frac{N r_e^2 \gamma}{\alpha \sigma_z (\sigma_x + \sigma_y)}$$

The luminosity is thus proportional to $1/\sigma_x\sigma_y$, while the strength of beamstrahlung effect is proportional to $1/(\sigma_x+\sigma_y)$. By setting $\sigma_x >> \sigma_y$, we can achieve high luminosity and low beamstrahlung at the same time (for the nominal beam we have $\sigma_x = 639$nm，$\sigma_y = 5.7$nm).

The beam-beam effect could be simulated through the Guinea-Pig software package [31]. Figure 3.21 illustrates the energy spectrum of 500GeV nominal beam at the interaction point. The beamstrahlung effect causes a long tail at the low energy side. In our full simulation study of the Higgs recoil mass measurement, we will use Guinea-pig to simulate the beam energy at interaction point, and use this energy as the input of event generator.

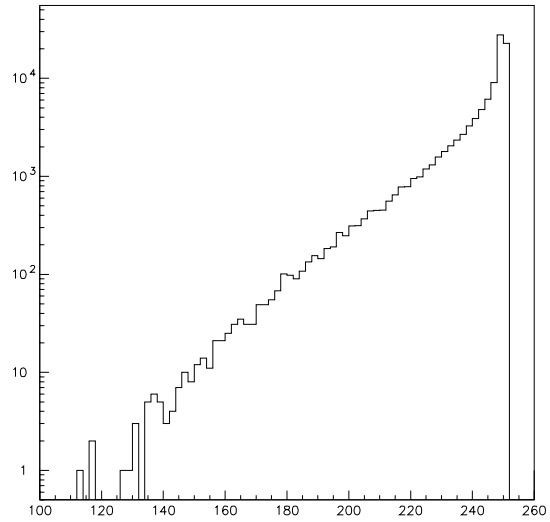

Figure 3.21 Energy loss caused by beamstrahlung effect (500GeV nominal beam)

3.6 Introduction of the ILC software

Before going to the next chapter, let's have a brief review of our software system [32].

3.6.1 LCIO and MARLIN

The most important packages in the ILC software is LCIO (Linear Collider Input and Output)[33] and MARLIN (Modular Analysis & Reconstruction for the Linear Collider)[34], LCIO defines the data format and provides the IO (Input and Output) standard, while MARLIN is an analysis framework and a module manager.

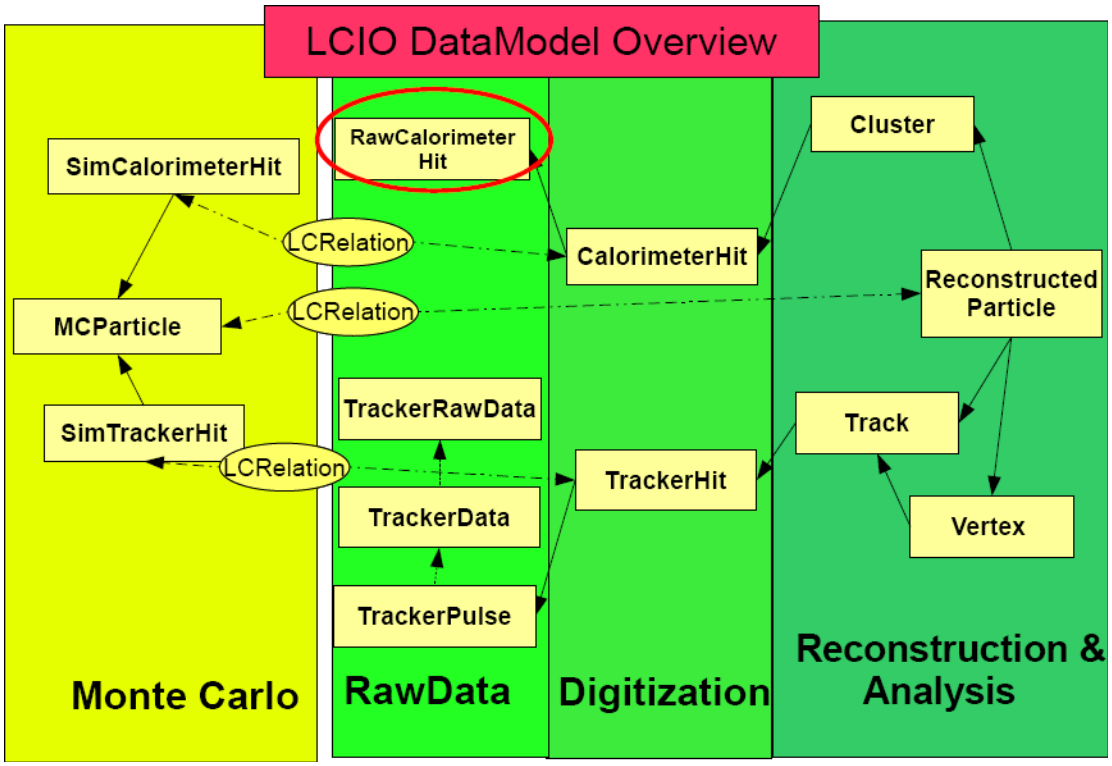

Figure 3.22 Different classes defined in the LCIO [35]

The format of the ILC data file is slcio. The information is stored into different collections. Each collection is corresponds to one or more classes defined by LCIO (see Figure 3.22). For example, we have the MCParticle collection to record the MCTruth information in the generator. LCIO also defines a special class called

LCRelation to record the connection between elements in different collections, with which you can easily test the performance of the reconstruction software.

MARLIN uses slcio files as its input and output file. As a module manager, each module could access all the information in the data file (as well as the information stored in the collections generated by previous modules), and write new collections into the data file. The users are allowed to drop any collections in the output step to reduce the size of output data file. MARLIN could be compiled with ROOT (our analysis platform), making it possible to write the information into a root file for later analysis.

Now let's introduce the software chain that we have used in our full simulation analysis.

3.6.2 From the generator to the analysis: The ILC simulation, reconstruction and analysis software

Generator: Whizard [36] and Pythia [37]

The generators we used in our full simulation study are Whizard and Pythia. We use Whizard to simulate our signal process, and use Pythia to simulate the background. Whizard stand for W, Higgs, Z and respective decays, it could be used to simulate all the processes with less than six final state particles at parton level (within the framework of both the SM and the MSSM). Whizard needs to be compiled with the library files of Pythia to realize the fragmentation process.

The generators read in the beam energy in the output file of Guinea-pig [31] (with which we can change the beam parameters), and by setting objective physics channel and corresponding physics parameters, the generators calculate the 4-momentum of the final state particles and write these informations into the output file with the stdhep format [38].

Simulation: Geant4 [39] and MOKKA [28]

We use Geant4 and MOKKA to do the full simulation. The output of the generators is a collection of final state particles (electron, muon, photon, Kaon…) with their 4-momentum and position information. MOKKA reads in the information (or use particle gun) and simulates their interaction with the detector. This process is realized in two steps: first, the processes of different particles interact with different materials; these are summarized into corresponding Geant4 library files (with huge size); second, different materials are organized to be a detector with certain geometry given by MOKKA (in other word, MOKKA is the ILC geometry plug-in of Geant4).

MOKKA supports many different detector concepts, including a set of the LDC and SiD detector concepts as well as the CALICE test beam experimental setting up (Figure 3.23 [40]), etc. When a detector concept is selected, users are allowed to drop the sub-detectors that are not really needed to accelerate the simulation process, i.e., we drop all the calorimetry system when we doing the μ momentum measurement study. The detector geometry parameters are organized by MySQL software [41] .

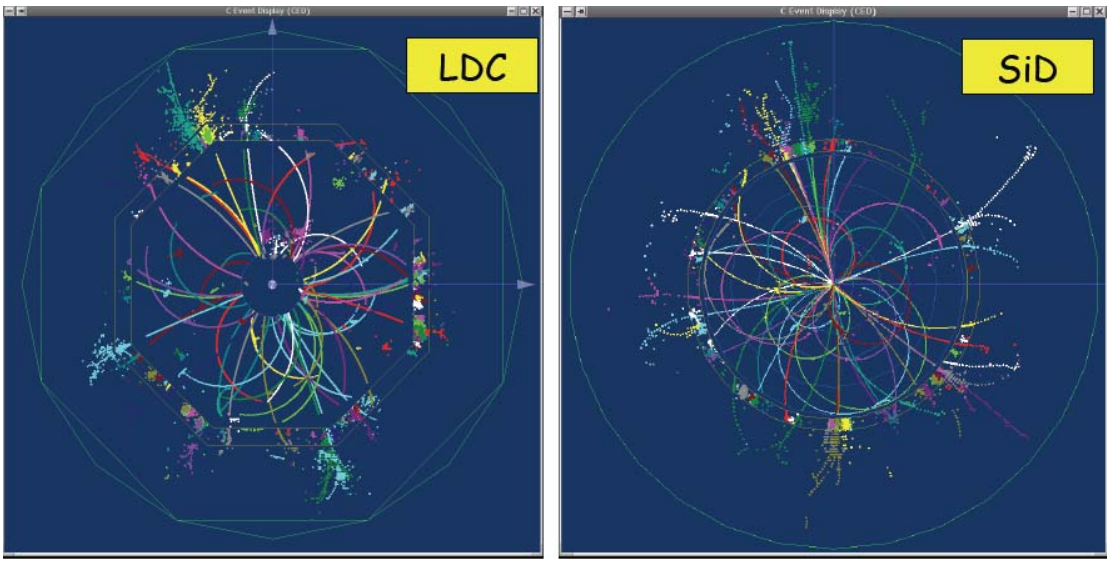

Figure 3.23 MOKKA: Simulation of $e^+e^- \to t\bar{t}$ process with the LDC and the SiD detector concepts [40]

MOKKA could be compiled with LCIO and is able to output the simulation

result in format of slcio file. MOKKA could also be compiled with GEAR [42], which enables the output of the detector geometry in an xml file, which could be used in the later reconstruction process.

Reconstruction: MARLIN and MarlinReco [43]

The reconstruction is realized through a set of modules organized by MARLIN. These modules constitute the MarlinReco package, a typical reconstruction process is shown in Figure 3.24.

The output slcio file of MOKKA could be used directly as the input file for MarlinReco. What is also needed is an xml file describing the detector geometry, which could be generated using GEAR. The detector hits stored in the input data file are first digitized and then reconstructed into tracks and clusters, and the PFA package (or called PFlow) reconstructs the tracks and clusters into the 4-momentum and position of reconstructed particle.

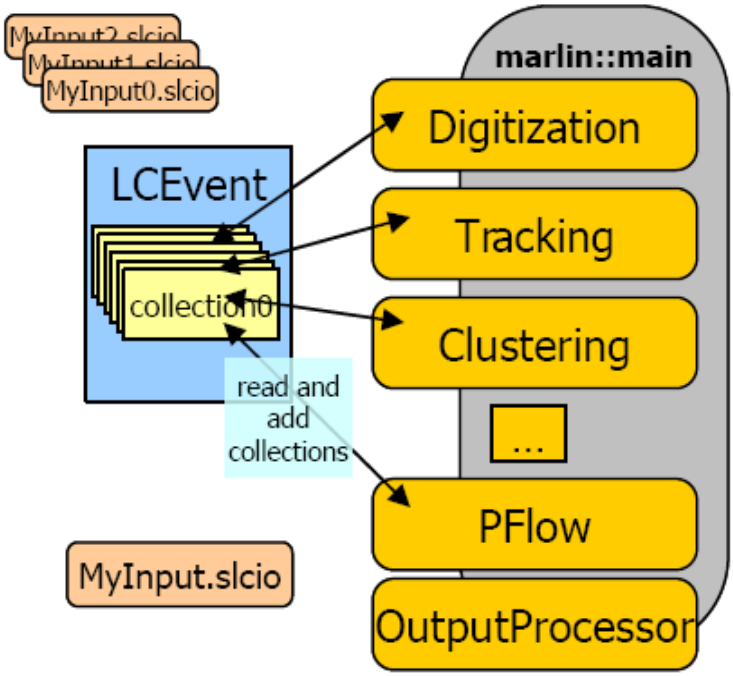

Figure 3.24 Reconstruction process in MarlinReco [40]

The default PFA module in MarlinReco package is WOLF [44]. But

currently PandoraPFA [45] is much more frequently used.

Particle identification and analysis:

Currently the official version of MarlinReco doesn't contain the PID module, so the development of high-efficiency PID module is of vital importance in the ILC software development. O.Martin (DESY) and Du S.X (LAL/IHEP) have made many efforts on it [46].

After the PID each reconstructed particle is assigned with a type. The information as well as its 4-momentum and position can be easily written to a ROOT file (for MARLIN could be compiled with ROOT), with which it's very convenient to do the analysis. The simulation and reconstruction software and its dependency are summarized in Figure 3.25.

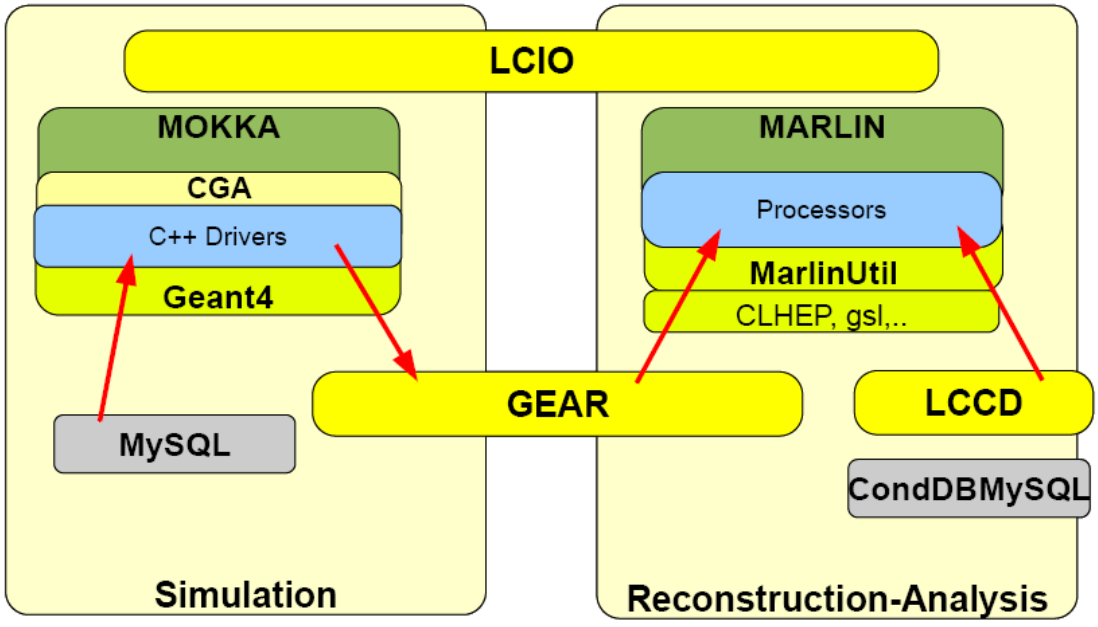

Figure 3.25 Simulation and reconstruction software framework [40]

3.6.3 Grid：massive computing and storing tool [47]

Full simulation and reconstruction make a huge requirement on the computing & storing resources. This could be satisfied through the grid tool.

The basic units of grid are computing element (CE) and storing element (SE). All the files stored on grid will be given a unique logical file name (LFN), for example:

/grid/calice/tb-cern/rec/rec_v0406/Run331666_rec.000.slcio.

The grid provides some basic operation as upload, download, job management, etc. These operations could be organized into scripts for different purposes. A typical grid computing process is shown in Figure 3.26. The CE downloads the executable file, the steering file and the data files from the SE, executes the executable file locally and uploads the output data file back to the SE. With the grid, a job could be executed on thousands of CPUs at the same time and stored in the SE all over the world. Our computing capability has been largely boosted by the grid tool.

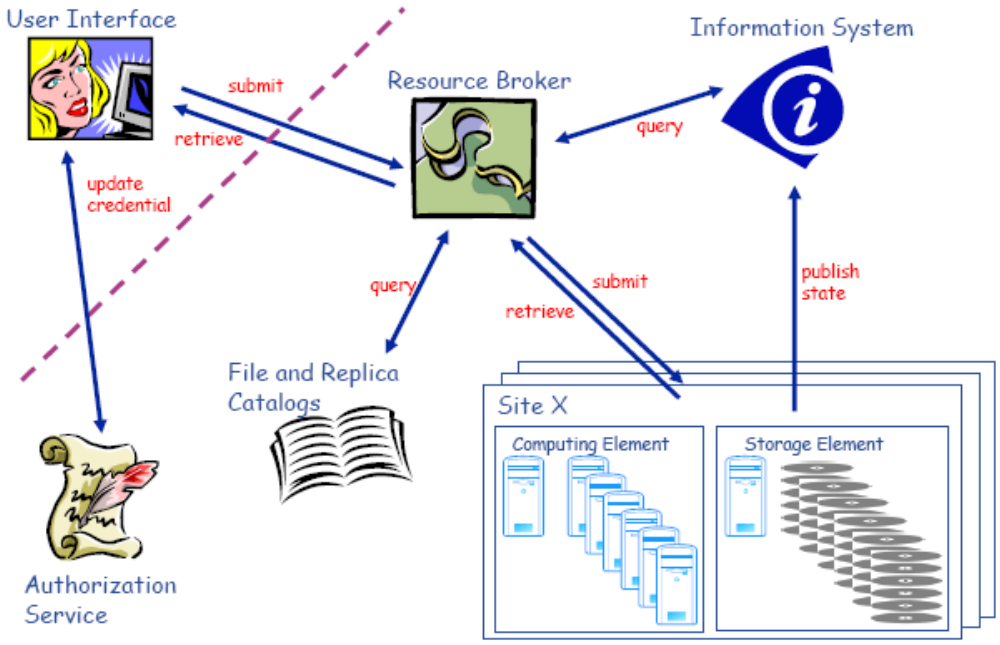

Figure 3.26 Grid computing process [47]

3.6.4 CALICE software：

Besides the ILC software we introduced above, the CALICE collaboration developed two packages to support the test beam experiment and data analysis, named Calice_reco and Calice_userlib [50]. Together with other database software (MySQL [41]，LCCD [48]，CondDBMySQL [49]), the Calice_reco package reconstructs the ADC value of each channel into calorimeter hit; and Calice_userlib provides library files of frequently used functions, making it easy for people doing analysis. Usually, if a member of the CALICE collaboration developed some software module, the source file will be submitted to the CALICE software coordinator, and the coordinator will combine the source file to the Calice_userlib package. The software coordinator is also in charge of the maintenance and updating of the software.

3.6.5 Discussing

There are in total over twenty different ILC software packages with complex dependency, especially, the ILC software is also in the R&D phase, which means that one needs to update his software from time to time. It is not a trivial work to install all the ILC software ---- a full installation (compile every package from the source file) of all the ILC software on a computer with CERN Scientific Linux 3.0 operation system needs at least 4 hours. Now people at DESY have developed a script called ilcinstall [51] supported by A File System (AFS) and Cmake. To install all the ILC software, in principle one only needs to modify the parameters according to his personal needs, and executes the script.

The software we introduced is the European version of the ILC software. Actually in American and Japan there exist similar software systems. The Japanese version of the ILC software also takes LCIO as the data format, while the simulation and reconstruction software are called Jupiter and Satellites. With the emergence of the ILD collaboration, the software system will be changed and upgraded. As a first test, some cross check on the software system have been made and the results are

reasonable and agree with each other (Figure 3.27).

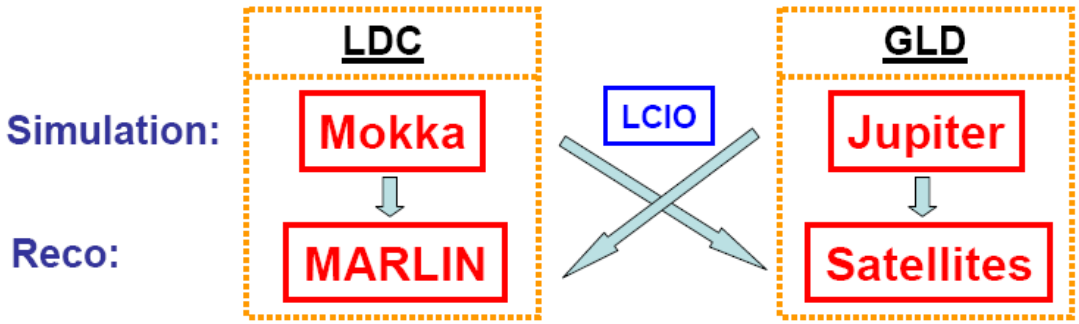

Figure 3.27 Cross check between European and Japanese version of the ILC software [27]

3.7 Summary

In this chapter, we introduced the ILC detector, accelerator and the ILC software system.

On the ILC detector, we presented current four detector concepts, the emergence of the ILD concept and current status of the ILD optimization study. Then we introduced the LDC01_Sc detector concept, which has been utilized in our full simulation study. With the LDC01_Sc detector geometry we also studied the μ momentum measurement accuracy, based on which we have developed a fast simulation package for the Higgs recoil mass measurement. As for the ILC accelerator, we discussed the main components of the accelerator, beam parameters and beam-beam effects. Also we gave a general view of the ILC software system.

In the next chapter, we will switch to our full simulation study on the Higgs recoil mass measurement through $e^+e^- \to HZ \to H\mu\mu$ channel.

Chapter 4 The Higgs recoil mass and cross section measurement through $e^+e^- \to HZ \to H\mu\mu$ channel

4.1 Introduction

At the ILC most of the Higgs particles will be generated through the Higgs-strahlung process ($e^+e^- \to HZ$) and the W fusion process ($e^+e^- \to Hvv$)[2], see Figure 2.2. For the Higgs-strahlung process, 10 percents of the Z bosons will decay into a pair of leptons (the chances for each generation of leptons are identical, about 3.3% each). Because the momentum of μ/electron can be precisely measured by the tracking system, we could measure the recoil mass of the Higgs particle through the $e^+e^- \to HZ \to H\mu\mu$ and $e^+e^- \to HZ \to Hee$ processes; and, since when passing through the material the electron has much stronger radiation effect than the μ, we use $e^+e^- \to HZ \to H\mu\mu$ process as our signal.

Assume the Higgs mass is 120GeV. The center-of-mass energy is chosen to be 230GeV, about 10% above the product threshold. As shown in Figure 2.3, the cross section is very close to its maximal at 230GeV center-of-mass energy. Because the error on Higgs recoil mass is proportional to the muon momentum squared, smaller center-of-mass energy means better Higgs mass resolution per event [12]. For non polarized beam, the cross section for our signal process is about 6.62fb, meaning we will have about 3310 events with 500fb^{-1} integrated luminosity.

As we have discussed in Chapter 2.2, here we apply the recoil mass method to measure the Higgs particle mass. The μ momentum could be preciously measured by the tracking system, take $k(P) = \delta P / P^2 \approx 5 \times 10^{-5} / GeV^{-1}$, for a 60GeV μ, the momentum measurement accuracy is about 180MeV. With formula 3.1 we can calculate the expected error on the Higgs recoil mass from the error on μ momentum measurement: assume the Z boson decays into a pair of μ with identical momentum (symmetric case), so $p_1 \approx p_2 \approx 51GeV$; taken $k(p_1) \approx k(p_2) \approx 5 \times 10^{-5}$, then for a single event, the mass measurement accuracy

could reach 228MeV; if the Z decays along its momentum direction (the most asymmetric case), the mass measurement accuracy will be 360MeV per event – so with totally 3300 events, the accuracy of the Higgs recoil mass measurement could reach 6MeV level!

The above estimation is obviously too optimistic. First, for μ with small polar angle, the momentum measurement could be much worse than its average level (see Figure 3.11). While in equation 3.1, we know that the error on Higgs recoil mass measurement is dominated by the larger error of two μ momentum measurements. If we require both μ to be in the "good region" of the detector, i.e., both μ with polar angle bigger than 40 degree, that we will lose almost half of our events. Second, because of the radiation effect (including beamstrahlung, initial state radiation (ISR) and final state radiation effect (FSR)), the Higgs recoil mass spectrum is not a central symmetric distribution: the energy loss caused by any radiation effect increases the recoil mass, creates a very long high energy tail on the recoil mass spectrum, see Figure 2.2. Both effects caused the error on the Higgs mass measurement increased to 30MeV level. In section 4.2 we will discuss in detail the radiation effect and its effect on the result.

In the recoil mass method we use no information from the Higgs decay final state. So in principle we could have a model independent Higgs mass measurement by avoiding using any cut based on Higgs decay final state information (including the total energy, the multiplicity, the isolation angle, etc). Alternatively, with some assumptions of the physics model, we could apply some additional cuts to achieve a better result in the model dependent analysis.

Now we will begin our discussion on radiation effect.

4.2 The Radiation effect

The recoil mass method is very sensitive to the radiation effect. The beamstrahlung effect (BS) causes the decrease of the center-of-mass energy, while the μ particle loses some of its energy through the ISR and FSR effects. All those three effects increase the recoil mass, making a high energy tail on the recoil mass

spectrum (Figure 2.2). Since the radiation effect is of extremely importance in our study, we briefly introduce the corresponding simulation tools/method to those effects and estimate their effect.

As mentioned in Chapter 3, we simulate the Beamstrahlung effect with Guinea-Pig software, while the output beam file (containing the information of beam energy with Beamstrahlung effect corrections at the interaction point) is used as the input file for Pythia and Whizard (Our generator).

The ISR is a very important radiation effect, which can in some case totally change the physics picture, for example, in $e^+e^- \to \mu\mu\gamma$ events (one of our main background), by radiating a high-energy photon, the ISR effect could reduce the energy of mediate Z boson to the Z threshold, and make the distribution of two μ invariant mass peak at the Z pole. For the $e^+e^- \to HZ \to H\mu\mu$ process, besides the high energy tail on the recoil mass spectrum, the ISR effect will affect the cross section, see Figure 2.4. At center-of-mass energy equal to 230 GeV, the ISR effect will suppress the cross section (according to the subtraction of phase space) by 20%. Our generator software, Whizard and Pythia could directly simulate the ISR effect.

Comparing to the ISR effect, the FSR effect is a smaller correction. Also since the mass of μ is about 200 times the electron mass, the FSR effect is much weak in $e^+e^- \to HZ \to H\mu\mu$ channel than in $e^+e^- \to HZ \to Hee$ channel. In our study, the FSR effect is simulated with Pythia (in Whizard the FSR effect is simulated in the fragmentation step, which is realized by calling Pythia libraries). We need to mention here that Pythia has not yet considered the interference between the ISR and FSR effect.

In our analysis, three radiation effects are independently simulated. The reconstructed recoil mass spectrum could be regarded as a convolution of the true recoil mass spectrum with the radiation effects and resolution, meaning:

$$Spec(Full) = Spec(true) \otimes Spec(radiation) \otimes resolution \quad (4.1)$$

First, let's study the resolution term in equation 4.1 with our fast

simulation tools (Chapter 3.4). To understand the detector resolution, we generate a sample without any radiation correction (if ignore the Higgs width, the recoil mass spectrum truth is a δ function peaking at 120GeV). Because our signal process is an S-wave process, the angular distribution of the final state Z boson is isotropic, while some of the μ particles decay from Z will hit the forward region of the detector, these μ particles have significant worse momentum resolution than the μ hit in the barrel region, and will result in a wider Gaussian distribution in the Higgs recoil mass spectrum – so, the spectrum could be regarded as an overlay of a narrow Gaussian with a wider Gaussian (the Probability Distribution Function is shown in Figure 4.1), which is quite often seen in high-energy physics.

Making a Gaussian fit to the core part (narrow Gaussian) of Figure 4.1, the width is about 280MeV. This value is within our estimation (228-360MeV). Now let's consider the radiation effect at MC-Truth level. Shown in Figure 4.2, the blue histogram corresponds to the Higgs recoil mass with FSR effect only, the red histogram has only the ISR effect and the green one has considered all three radiation effects. In Figure 4.2 it is also quite clear that the FSR effect is much smaller than the ISR effect.

For the ISR effect (red histogram in Figure 4.2), about 60% of events have no ISR effect or the ISR photon with energy less than 250 MeV (statistics in the first bin). If it radiates a photon with energy higher than 20GeV, the remaining energy is not sufficient to generate a Higgs boson and a Z boson. That causes a significant bump on the recoil mass spectrum (at 140GeV). For the FSR effect, more than 70% of events have no FSR photon or the FSR photon has energy less than 250MeV, indicating also the FSR effect is weaker than the ISR effect. While the high energy tail caused by the FSR effect is much smooth than the one with ISR: no bump pattern is observed in the recoil mass spectrum with the FSR effect only.

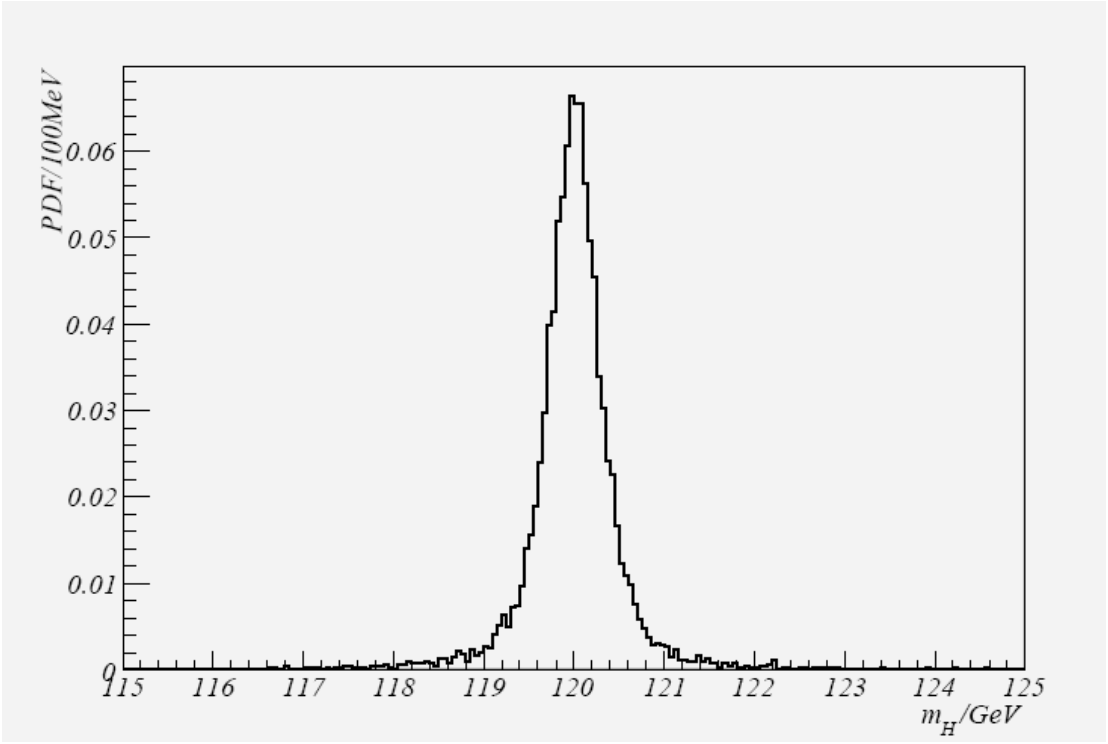

Figure 4.1 PDF of Higgs recoil mass spectrum without radiation correction

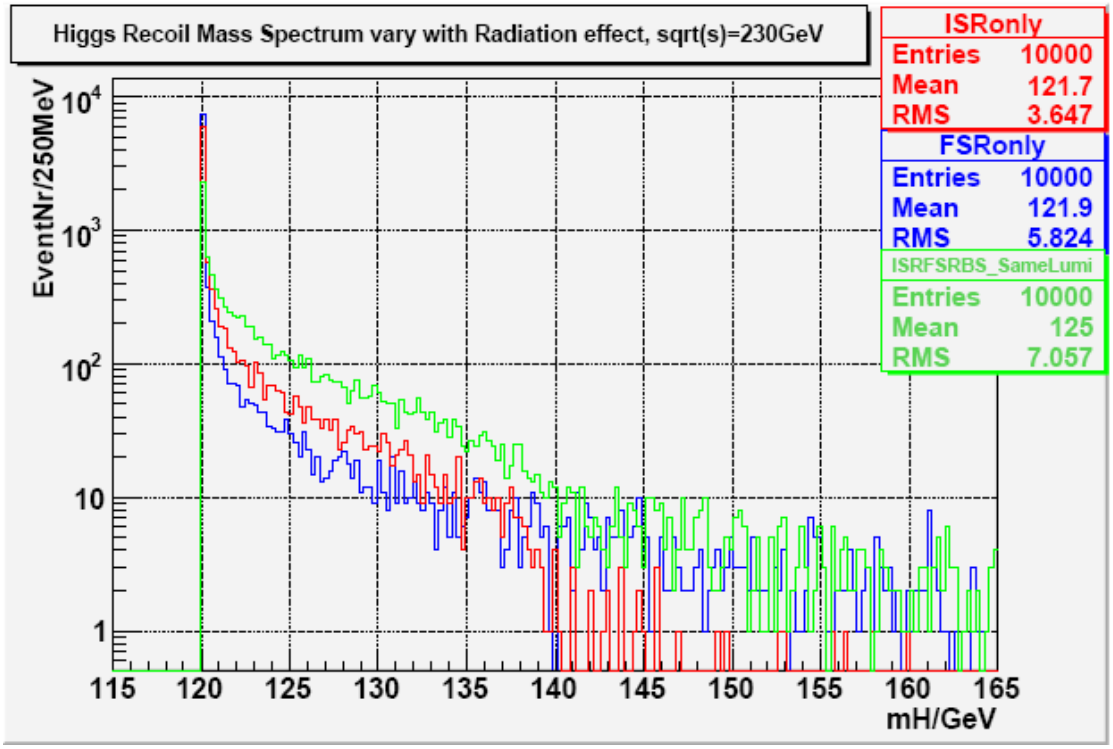

Figure 4.2 Recoil mass spectrum at MC truth level (with different radiation effects)

If we consider all radiation effects together, about 15% of events will radiate photon with a total energy larger than 250MeV. That means the BS effect is very significant. Since the strength of the BS effect depends only on the beam parameters, for different physical purpose, there exist also an optimum set of beam parameters (besides the center-of-mass energy). We will discuss a preliminary study on the beam parameter selection in the last section of this chapter.

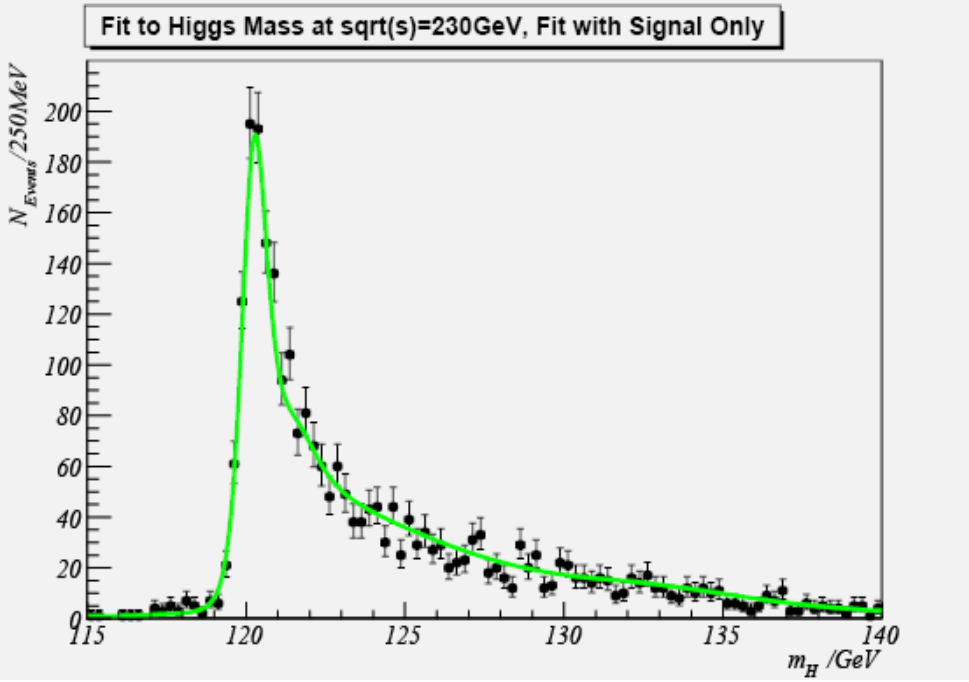

Figure 4.3 Reconstructed Higgs recoil mass spectrum (signal only)

The reconstructed recoil mass spectrum is shown in Figure 4.3. As we mentioned above, only 15% of events have radiation correction less than 250MeV, those events corresponding to the 120GeV peak in the reconstructed recoil mass spectrum, and play the most important role in our Higgs mass measurement. That means, statistically, if we use only those events, the expected mass resolution is about $280/\sqrt{0.5*3310*0.15} \sim 20MeV$ (here the factor 0.5 is caused by the truth that we could only rely on the information of the low-energy part of 120GeV peak). This estimation agrees with our result.

Now let's begin our discussion on the background and event selection.

4.3 Main backgrounds and precut

In a model independent analysis, the backgrounds include all the processes which have two energetic π/μ particles in the final states (π is taken into account for current PID has about 1% chance to misidentify a π as a μ). In Table 4.1 we list all the backgrounds and their Feynman diagrams are shown in Figure 4.4.

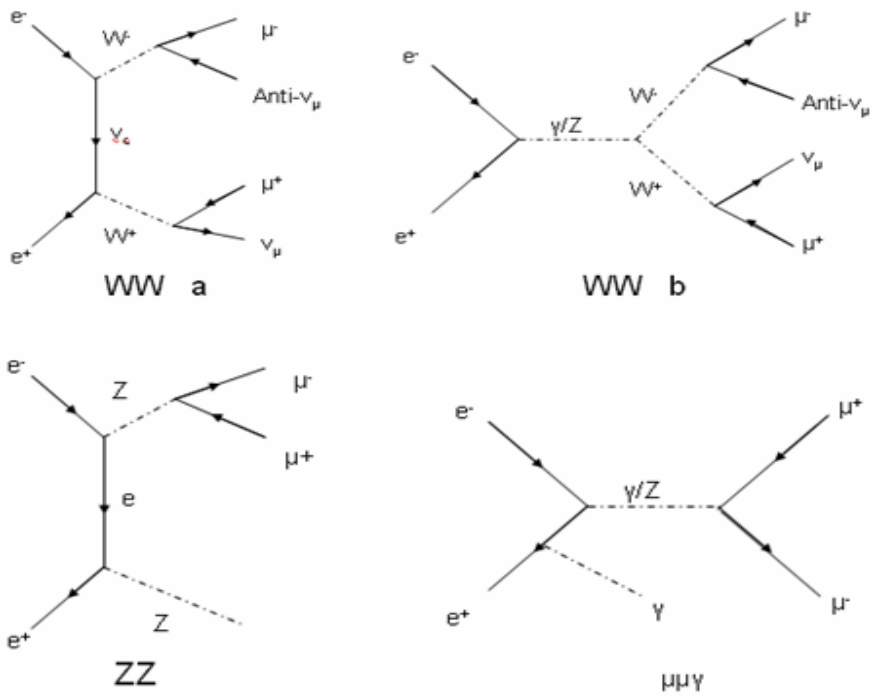

Figure 4.4 The Feynman diagrams for backgrounds. The majority of WW background is generated in T channel

$\sqrt{s}$ /GeV	230GeV	250GeV	350GeV
$\sigma(e^+e^- \to HZ) \times Br(Z \to \mu\mu)$ /fb	6.62(3310evt)	7.78 (3890)	4.87 (2435)
$\sigma(e^+e^- \to ZZ)$ /fb	1.34k (672k)	1.27k (635k)	0.856k (428k)
$\sigma(e^+e^- \to WW)$ /fb	15.86k (7.93M)	15.61k (7.81M)	1.155k (5.77M)
$\sigma(e^+e^- \to q\bar{q})$ /fb	57.6k (28.8M)	52.2k (26.1M)	22.63k (11.3M)
$\sigma(e^+e^- \to \mu\mu\gamma)$ /fb	5.38k (2.69M)	4.34k (2.17M)	2.20k (1.1M)

Table 4.1 Main background and corresponding cross section (fb) and the expected event number at 500fb^{-1} integrated luminosity (with radiation effect correction)

The $e^+e^- \to ZZ$ process and $e^+e^- \to WW$ process have quite a chance to generate directly into two energetic μ or generate a lot of π in the hadronic decay final state (see Figure 4.5). The $e^+e^- \to q\bar{q}$ channel which will also generate a lot of π, as discussed above, shall also be considered as our background.

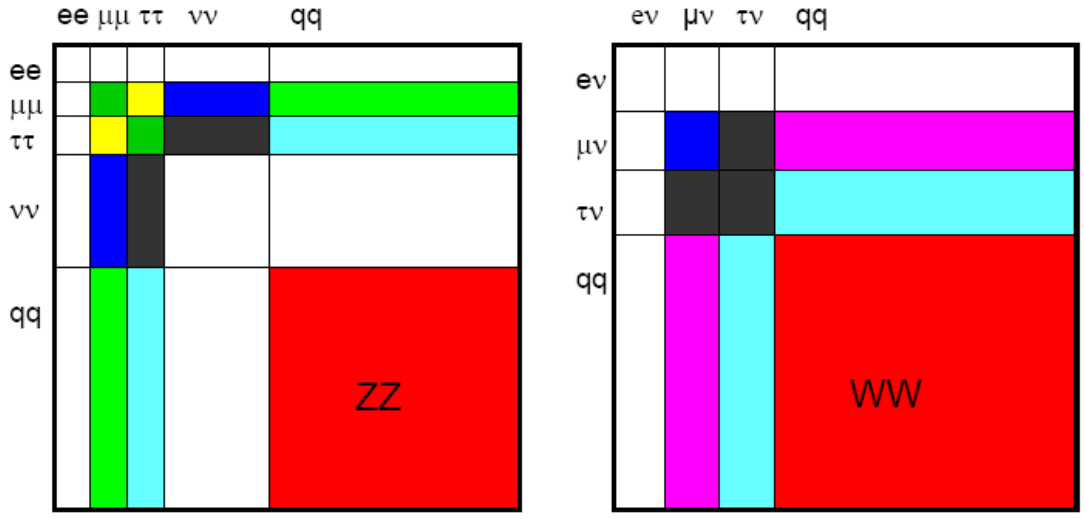

Figure 4.5 Decay final states of $e^+e^- \to ZZ$ process and $e^+e^- \to WW$ process. Here different blocks refer to different decay final states of ZZ and WW events. The size of the block is proportional to the branching ratio. The colored blocks will act as our background

As shown in table 4.1, the statistics of the backgrounds is much higher than our signal. That means it's very hard for us to do the full simulate for all the background. So before processing to full simulation, we apply some precuts at the generator level, these precuts will be replaced with much stricter cuts in latter analysis. Since we attempt to do a model independent analysis, the precuts use only the 4-momentum information of the 2 μ particles.

We introduce four precuts (see Table 4.2) here:

1、Exist at least one μ or π with energy larger than 15 GeV;

2、Select the most energetic μ/π, we require another μ/π, together with the first μ/π to form an invariance mass larger than 70GeV;

3、The two selected μ/π have their angle projection on the R-φ plane to be less than 177.6^o. This precut is mainly used to reduce the $e^+e^- \to q\bar{q}$ and

$e^+e^- \to \mu\mu\gamma$ background.

4、Kinematic restriction on the energy of the 2 selected μ/π (see Figure 4.6)

$$2E_1+E_2<180GeV \text{ and } 2E_1+3E_2>200GeV$$

here E_1 is the energy of the leading particle.

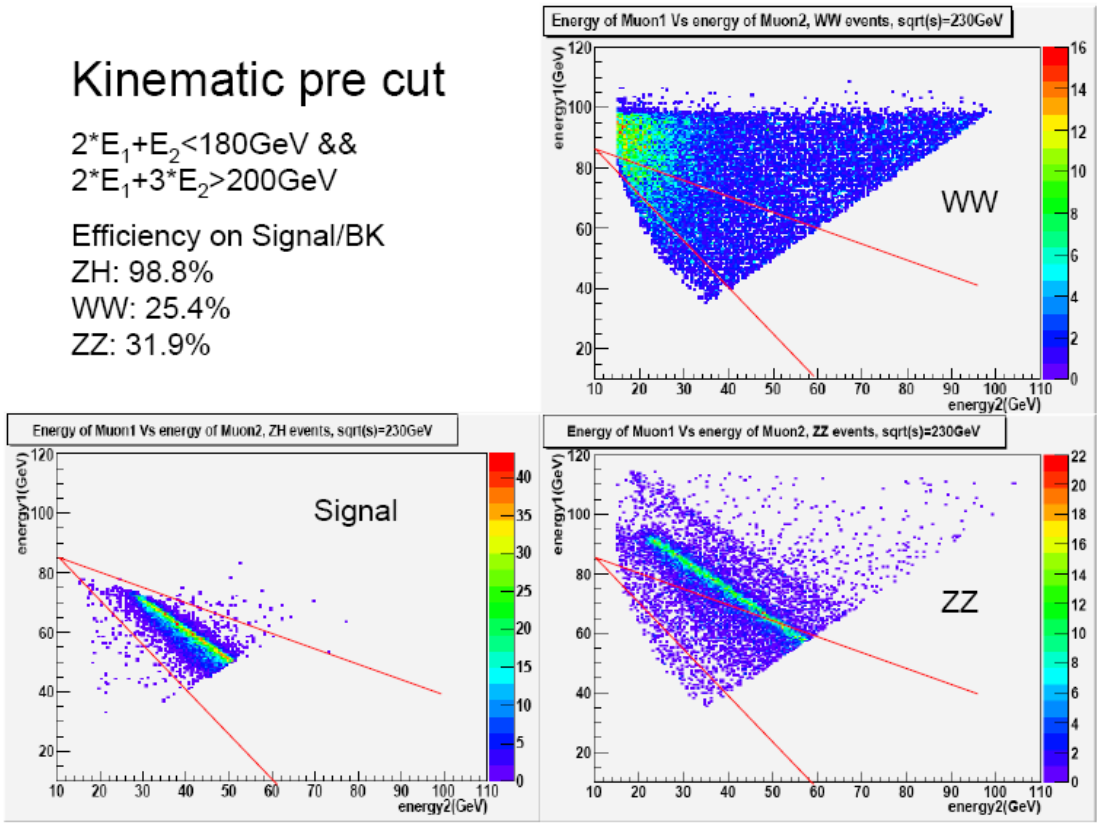

Figure 4.6 Kinematic precut selection on muon energy

Table 4.2 shows the effect of our precut. After the first 2 precuts, we lose 5% of the signal and the ZZ and WW background will be reduced by a factor of 10, while the $q\bar{q}$ events will be reduced by two orders of magnitude. About half of the μμγ events survive, for the ISR effect will make the invariance mass of μ concentrate at the Z pole. The precut $\Delta\varphi < 3.10$rad require a large transverse momentum for the μμ system. For the μμγ events, the ISR photon always have very small polar angle and could not take away large transverse momentum, while the $q\bar{q}$ events always result in two back-to-back jets. So this precut greatly reduce the remaining $q\bar{q}$

and μμγ events. The kinetic precut is introduced to suppress the statistics of the remaining ZZ and WW events, as shown in Figure 4.6, the remaining ZZ and WW background will be reduced by a factor of 2-3 with this kinetic selection. Totally with these precuts we reduced the background by 2-3 orders of magnitude, while the cost is 10% of our signal statistics.

	ZH	**ZZ**	**WW**	$q\bar{q}$	**Mμγ**
Before Precut	3310	672k	7.93M	28.8M	2.69M
E_l>15	3310	347k	5.22M	15.8M	2.69M
mZ>70	3147	43.7k	310k	169k	920k
$\Delta\varphi < 3.10$ (177.6°)	3042	42.1k	299k	62.6k	242k
Kinetic	3000 **90.6%**	17.7k **2.6%**	81.9k **1.0%**	33.8k **0.12%**	23.1k **0.86%**

Table 4.2 Precuts and their effect

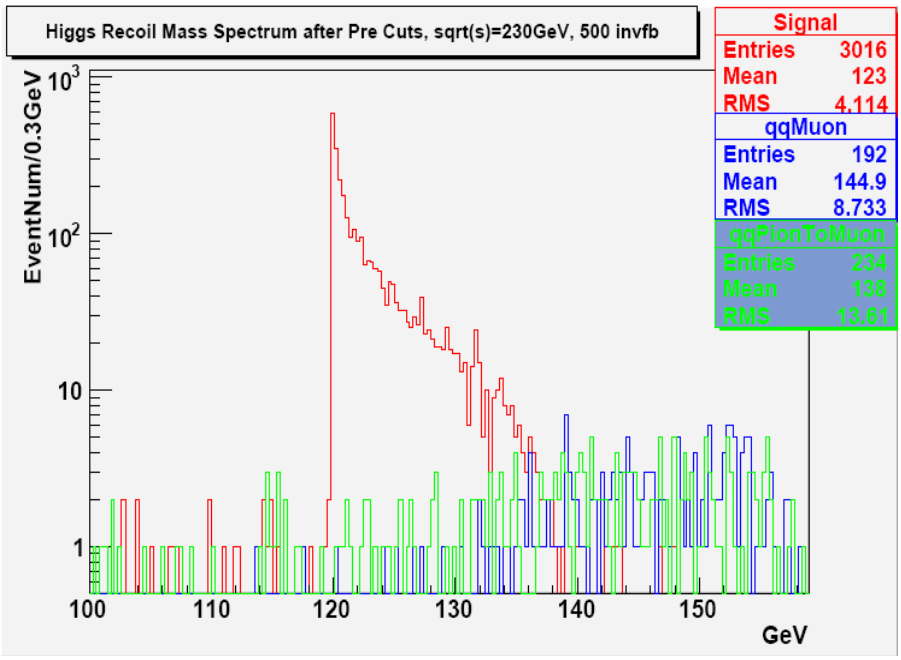

Figure 4.7 The distribution of $q\bar{q}$ background on the recoil mass spectrum. Blue, 2 μ generated; green, events with π misidentified as μ

Most of the $q\bar{q}$ events don't generate energetic μ (the only way is through semi-leptonic decay of $b\bar{b}$ events). If we require both μ to be identified in one event, there will be only few hundred $q\bar{q}$ events with recoil mass distribution far away from our signal region (See Figure 4.7) – that means we could safely neglect the $q\bar{q}$ background.

After the precut, the total events number is about 120k. It's still a large number but it's possible to be handled with the grid computing tools. Now let's introduce the model independent analysis on recoil mass measurement.

4.4 Model independent analysis on the Higgs mass and cross section measurement

4.4.1 Event selection: replacement of precuts and new variable

To make the result reliable, we require that the events dropped by the precut selection could not pass the event selection even after the detector smearing. So as the first step we need to replace precuts with much stricter cuts (here m_Z indicates the invariant mass of 2 μ):

Precut	***Cuts in analysis***
$E_1>15$	$E_\mu>20$
$2E_1+E_2<180GeV$ &&	$2E_1+E_2<178GeV$ &&
$2E_1+3E_2>200GeV$	$2E_1+3E_2>202GeV$
$\Delta\varphi < 177.6^o$	$\Delta\varphi < 175^o$
$m_Z>70$	$70 < M_a < m_Z < M_b$ （to be fixed）

In the event selection we first require both μ to be identified. With the support of dedicated tracking system, the accuracy of μ momentum resolution is about 10-100MeV, so the replacement of our first 2 precuts has at least a distance of 10σ; while the TPC has very high angular resolution, so the third precut is also safely replaced; the forth cut has not yet been fixed, we will make a cut optimization to determine the parameters in the forth cut, see next section.

After we have replaced the first 3 precuts, we have 10.9k μμγ, 5.2k WW events, 10.7k ZZ events and 2261 signal events. The distribution of the μ invariance mass is shown in Figure 4.8. There is a clear bump caused by the precut $m_z>70GeV$ (with few events smeared to the lower side of 70GeV). The distribution of the WW events is quite smooth, since most of the time the 2 μ decay independently from 2 W bosons, and there has no direct correlation in their momentums. As for the signal and the ZZ background, the majorities of those events have their two μ decay from a Z boson, and thus create a peak in the Z pole. For the μμγ events, the ISR effect causes the Z pole peak as well. Because of the FSR effect, the Z pole peak for ZH, ZZ and μμγ have larger tail on the low energy side.

After replacing the first 3 precuts, the distribution of the signal and backgrounds on the recoil mass spectrum is shown in Figure 4.9. And in the mass window we selected (115-135GeV), the corresponding statistics is 2201 ZH events, 5.7k μμγ events, 3.1k WW events and 3.6k ZZ events, while the signal represents about 15% of the total statistics. The signal peak in Figure 4.9 is quite significant.

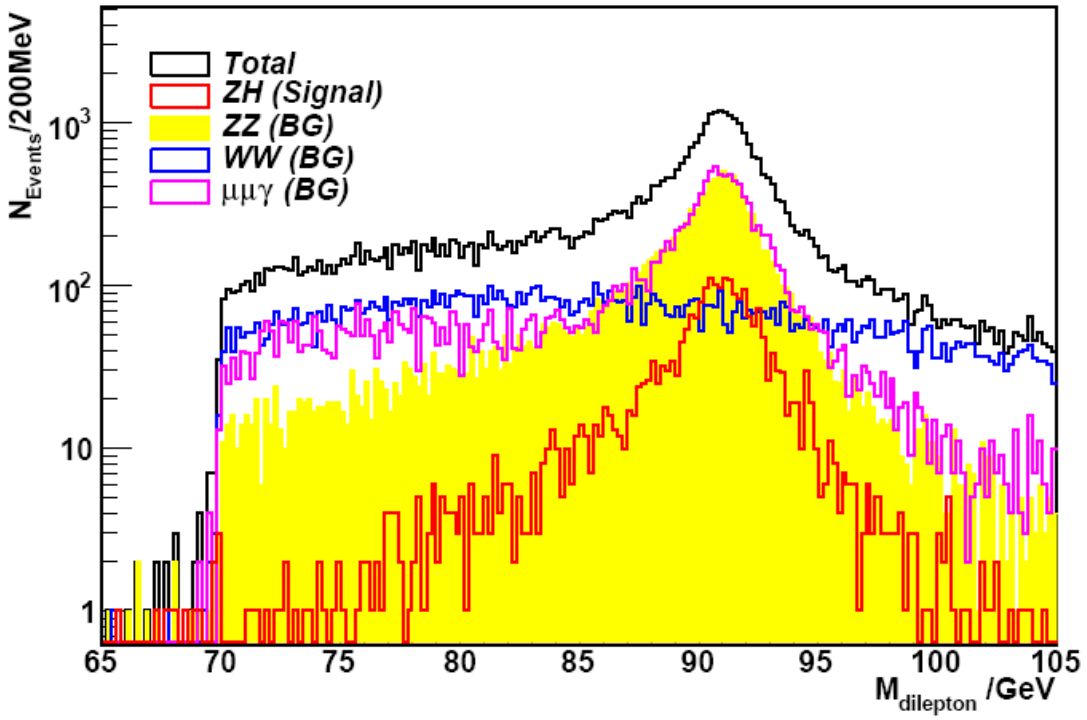

Figure 4.8 Distribution of di-lepton invariance mass

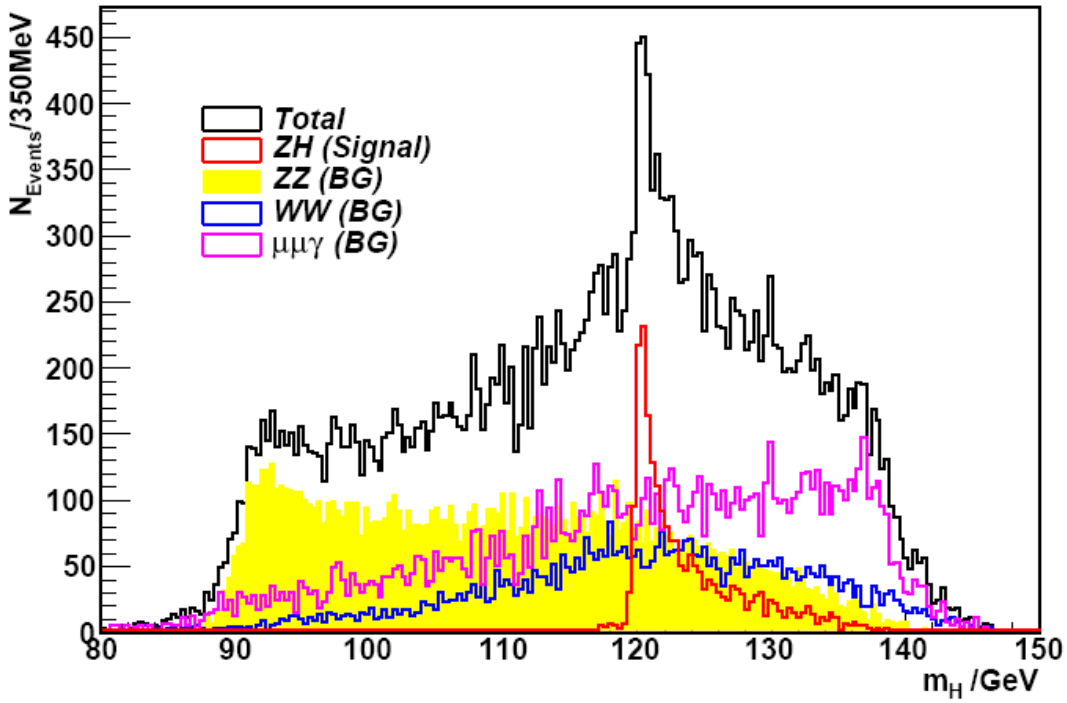

Figure 4.9 Distribution on the recoil mass spectrum (model independent analysis, with first 3 precut replaced)

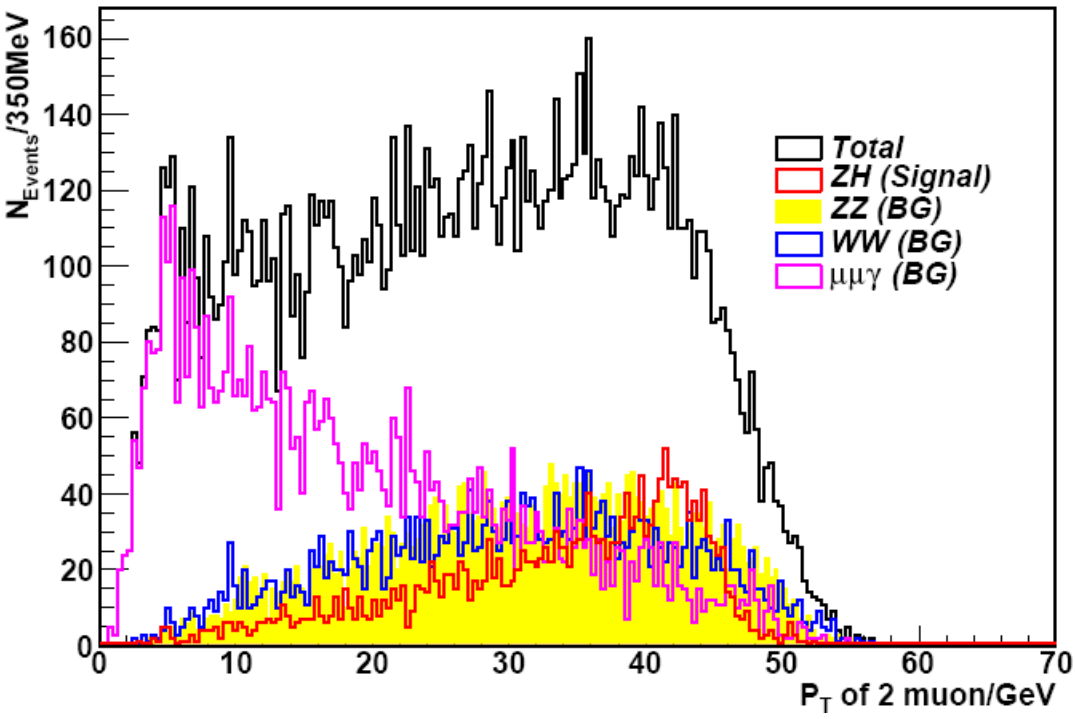

Figure 4.10 Distribution for total transverse momentum of μ system

In Figure 4.9 we notice that the μμγ background has huge statistics. We try to use some new variables to reduce it. One of the new variables we choose is total transverse momentum of the μ system, and in Figure 4.10 we show its distribution.

In Figure 4.10 we found that the total μ transverse momentum concentrates at low energy for the μμγ events, that's because the μμγ events always have an ISR photon radiated at small polar angle, and could not take away large transverse momentum. For the ZZ, WW and ZH events, the distribution is much smooth, while for signal it will slightly concentrate to the high energy side. That is because the WW and ZZ events are mainly generated in a T wave process, and the μ transverse momentum is slightly smaller than ZH events, which is generated in an S wave process. So our additional cut will be a lower limit on the transverse momentum of the μ system. We mark this lower limit with symbol $\boldsymbol{P_a}$. To summarize, the cuts on model independent analysis are:

Both particles be identified as μ
E_μ>20
$2E_1+E_2<178GeV$ and $2E_1+3E_2>202GeV$
$\Delta\varphi < 175^o$
Invariance mass of μ system should between M_a − M_b GeV/c^2; (M_a>70GeV)
Total transverse momentum of μ system should be bigger than P_a GeV

Here we introduced 3 parameters, the up and lower limit of the invariance mass of the μ system (M_b and M_a), and the lower limit of total transverse momentum of the μ system (P_a). We will give optimized values to these 3 parameters in the next section.

4.4.2 The parameter optimization for the event selection

We could tune the parameters of the event selection to get the best measured result. Here the parameters we are going to tune are M_a, M_b *and* P_a, now let's study the dependence of signal the purity, the statistics and the fit result of the Higgs mass measurement with these parameters. To simplify this process, we give different priority to these parameters and optimize them: the order is M_a, M_b *and* P_a.

First, to select an optimized value of M_a, we need first to relax the event selection conditions with other parameters. Set M_b＝105GeV，P_a＝5GeV, and table 4.3 shows under this setting, the dependence of the result for different values of M_a (the last row shows the result of a likelihood fit to the recoil mass spectrum).

1、Scan of M_a value with step length equal to 3GeV：

M_a /GeV	74	77	80	83	86	89
Purity/%	12.9	13.4	14.1	14.8	15.3	15.6
Statistics	2317	2305	2275	2223	2089	1777
Fit width/MeV	45.10	44.94	44.97	44.32	42.58	43.50

2、So we know the best M_a take value between 83－89GeV，let's start scan with 1GeV step length

M_a /GeV	83	84	85	86	87	88
Purity/%	14.8	15.0	15.2	15.3	15.5	15.6
Statistics	2223	2186	2145	2089	2025	1923
Fit width/MeV	44.32	43.39	42.40	42.58	43.24	42.96

Table 4.3 Scan of optimized M_a value with P_a＝5GeV，M_b＝105GeV

From table 4.3 we know the optimized value for M_a is 85GeV. Set P_a equals to 5GeV，Now we start to scan the optimized value for M_b:

M_b /GeV	95	98	99	100	102	105
Purity/%	16.9	16.2	16.0	15.8	15.5	15.2
Statistics	2029	2103	2117	2122	2136	2145
Fit width/MeV	42.77	41.28	41.67	40.99	42.97	42.40

Table 4.4 Scan of optimized M_b value with P_a=5GeV，M_a=85GeV

So we have M_a = 85GeV, M_b = 100GeV.

With the same idea, we could find the optimized value for P_a:

P_a/GeV	5	10	13	15	17	20
Purity/%	15.8	17.2	18.2	18.7	19.4	20.3
Statistics	2122	2079	2032	1991	1944	1860
Fit width/MeV	40.99	39.92	39.38	38.33	40.35	41.52

Table 4.5 Scan of optimized P_a value with M_a=85GeV，M_b=100GeV

So we have a set of optimized event selection parameter: M_a=85GeV, M_b= 100GeV, P_a=15GeV. Therefore the corresponding event selection conditions are:

Both particles be identified as μ

E_μ>20

$2E_1+E_2<178$GeV and $2E_1+3E_2>202$GeV

$\Delta\varphi < 175^o$

Invariance mass of μ system should between 85 - 100 GeV/c^2; (M_a>70GeV)

Total transverse momentum of μ system should be bigger than 15GeV

Set the mass windows to 115－135 GeV/c^2, the event selection efficiency is 60.2%. The recoil mass spectrum is shown in Figure 4.11.

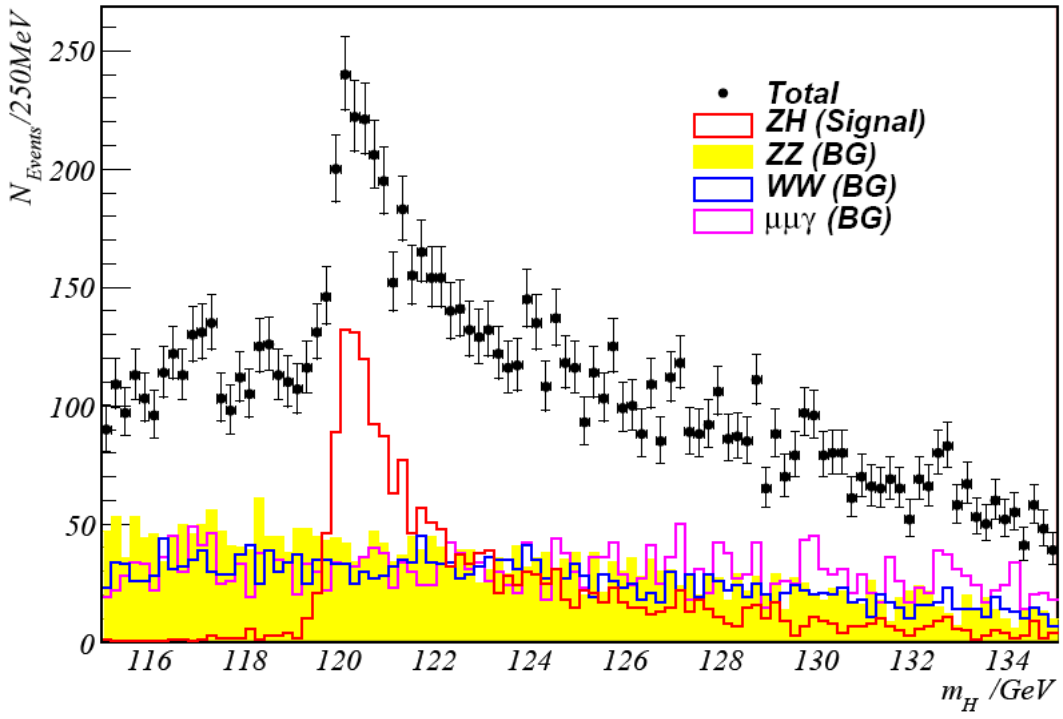

Figure 4.11 Higgs recoil mass spectrum after the event selection

In the next section, we will introduce the fit tools we have used in our analysis and show the fit result.

4.4.3 The fit method and fit result

In our analysis, the fit is performed with the likelihood method provided by Roofit [52]. Roofit is a specialized software package for fit based on ROOT framework. Its head files and libraries are included in the later version of ROOT, its function can easily be called in the analysis. The inputs for a typical fit process in Roofit are:

A distribution (always histogram) from the data;

A likelihood function (Probability Density Function, PDF) with one or more parameters to be fitted (these parameters are written into an analytic form of the likelihood function);

In our analysis, we use the smooth method provided by PAW (Physics Analysis Workstation) [53] to get the analytic form of this likelihood function. The analytic

form takes a default format of $PDF(para,x)=\exp(\sum a_i\sqrt{b_i^2+(x-c_i)^2})$, which to the 1st order could be regarded as the product of a set of Gaussians. For most of the time, we have $\sum a_i<0$, which means the value of this PDF approaches to 0 at infinite value of x. The Higgs particle mass can be written into the analytic form as a parameter to be fitted. Now given a recoil mass distribution, RooFit software could automatically fit the histogram to the likelihood function, and get the expected value and error of the parameter. Take the fit to the pure signal for example:

First, we generate a sample with Higgs mass set to 120GeV (7k statistics), with which we could get its recoil mass spectrum, and smooth it to a PDF.

Next, for an arbitrary Higgs mass m_h, we could write down its likelihood function $PDF(m_h,x)$ with known $PDF(120,x)$. Suppose the PDF has shift invariance in a small region (with this assumption the PDF is a function of $x-m_h$), we have:

$$PDF(m_h,x)=PDF(m_h+k,x+k).$$

So, if we write the Higgs mass into the form $m_h=120+\delta$ GeV, with an absolute value of δ small enough (for example, small than 1GeV), we have

$$PDF(m_h,x)=PDF(120+\delta,x)=PDF(120,x-\delta);$$
$$PDF(m_h,x)=\exp(\sum a_i\sqrt{b_i^2+(x-m_h+120-c_i)^2}).$$

Now for an arbitrary Higgs mass, we get the corresponding PDF and write the Higgs mass into the analytic form.

The distribution from data is from the full simulated data sample of our study. As the integrated luminosity is set to be 500fb^{-1} and the corresponding cross section is 6.62fb, the sample signal has 3310 events. And the fit result is (see Figure 4.3):

$$m_h=119.997\pm0.021\text{GeV}.$$

Now let's consider the histogram with both signal and background. First, the

distribution of the background could be fitted to a PDF invariant to the Higgs mass. As shown in Figure 4.12, the recoil mass spectrum of the background is quite smooth, and we simply fit it with a Gaussian (the corresponding χ^2, depending on different binning, always has its value between 1 – 1.5).

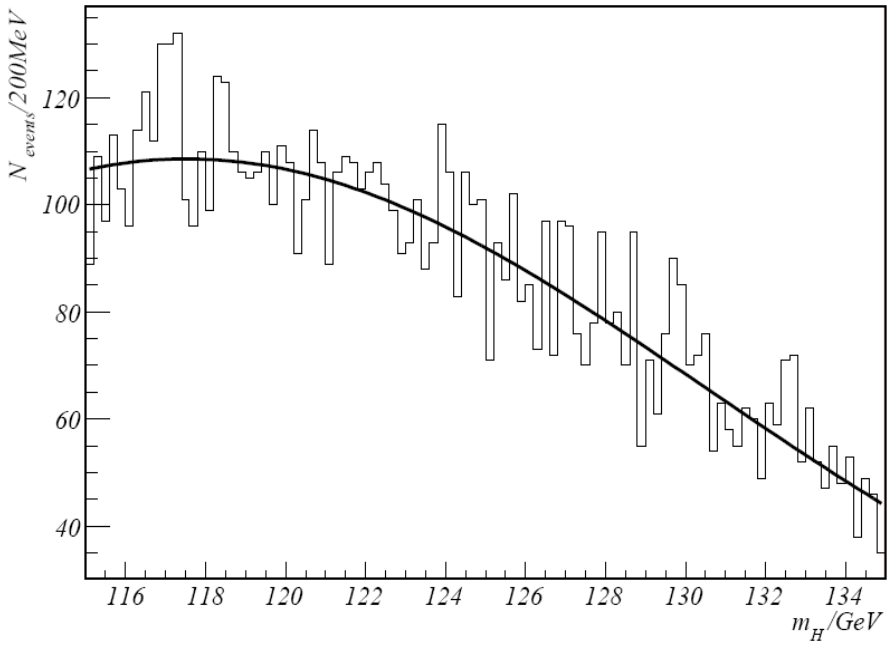

Figure 4.12 Gaussian fit to the background on the recoil mass spectrum

The histogram with both signal and background could be fitted to a PDF as a sum of the PDF of the signal and the PDF of the background:

$$PDF_{total}(m_h, x, w) = (1-w) \times PDF_{BK}(x) + w \times PDF_{Signal}(m_h, x)$$

$$f(x, m_h, w) = (1-w) \times \exp((x-m)^2 / 2\sigma^2) + w \times \exp(\sum a_i \sqrt{b_i^2 + (x - m_h + 120 - c_i)^2})$$

.

There are two parameters in the PDF; w is the weight of the signal, corresponding to the fraction of the signal in the total recoil mass spectrum (and thus corresponding to the cross section measurement); and the Higgs mass m_h (note that PDF_BK doesn't depend on the Higgs mass). Given a distribution on the recoil mass spectrum, we could fit it to this PDF, get the expectation value and corresponding

errors for both w and m_h.

The distribution depends on the event selection and we cannot take the PDF of the pure signal directly as PDF_Signal. We need to get PDF_Signal from the signal distribution after cuts to avoid bias. The result of the fit is (see Figure 4.13):

m_h - 120GeV = -8.13 ± 38.33 MeV, m_h = 119.992 ± 0.038 GeV;
w = 18.44% ± 0.97%.

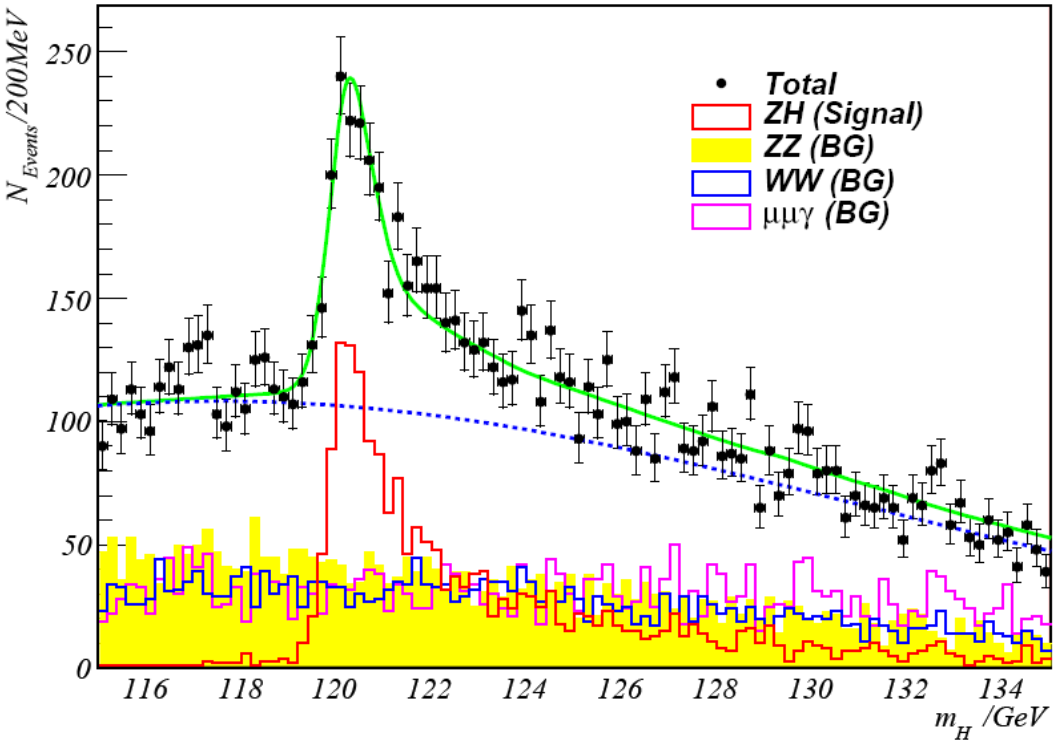

Figure 4.13 Fit to the Higgs mass and cross section in the model independent analysis

The total event number of any given distribution is easily known. Since $wN = \varepsilon \times L \times \sigma$ (N is the total event number; L is the total integrated luminosity; ε is the efficiency of event selection; and w is the fraction of the signal on the total spectrum, which could be calculated by the fit). The cross section could be expressed as $\sigma = wN/\varepsilon L$, since all these parameters are known here, the cross section could be calculated:

σ = 6.53 fb

Now let's discuss the error propagation on the cross section measurement.

$\sigma = wN/\varepsilon L$, take logarithm on both sides, we get

$\ln\sigma = \ln w + \ln N - \ln\varepsilon - \ln L$, take derivative,

$d\sigma/\sigma = dw/w + dN/N - d\varepsilon/\varepsilon - dL/L$.

In the experiment, L is measured by the LumiCal in very forward region of the detector, the efficiency ε could be estimated from the Monte Carlo simulation, and total event number N is the area of the histogram; the signal fraction w could be got from the fit. There is no direct correlation between these parameters, so the error on the cross section measurement could be expressed as follows:

$$\delta\sigma/\sigma = \sqrt{(\delta w/w)^2 + (\delta N/N)^2 + (\delta\varepsilon/\varepsilon)^2 + (\delta L/L)^2}$$

From the fit we know that δw/w is roughly 5%. At the electron-positron collider the luminosity could be preciously measured, so the term $\delta L/L$ is relatively a small number and we could ignore it here. For the efficiency ε, we could reduce its error by increase the statistics of the Monte Carlo sample, so the term $\delta\varepsilon/\varepsilon$ could also be neglected (if the systematic error is small). Reading from Figure 4.13, the total event number N here is 10655, corresponding to $\delta N/N \sim 1\%$. So the error on cross section measurement is dominated by the error on the fit of the signal fraction, w. we have:

$\delta\sigma/\sigma \sim \sqrt{(\delta w/w)^2 + (\delta N/N)^2} \sim \delta w/w$.

And the result of the fit is:

m_H = 119.992 ± 0.038 GeV

σ = 6.53 fb ± 0.35 fb (ignore the total statistic error $\delta N/N$)

or

σ = 6.53 fb ± 0.36 fb (taken into account the statistic error $\delta N/N$).

From the above analysis, we found that in the model independent analysis, Higgs mass could be measured to an accuracy of 38.4MeV, while the relative error on the cross section measurement could reach 5%. The overall efficiency on event selection is about 60%. In the next section, we will present the model dependent measurement.

4.5 The Higgs mass and cross section measurement in model dependent analysis

4.5.1 Variables used to distinguish event with SM Higgs and invisible decay Higgs

In different physics models, the behaviors of the Higgs decay are very different. Setting the Higgs mass equal to 120GeV, the majority of SM Higgs particle will decay into heavy quark (b, c) pairs or τ lepton pair. While in many other models, the Higgs could decay invisibly, i.e. the Higgs could decay into a pair of lightest SUSY particle (LSP) in some SUSY model, or it could decay into a pair of massive neutrinos. Figure 4.14 shows the comparison of Higgs decay branching ratios in the SM (right hand side [2]) and in the model with a massive neutrino (left hand side, the mass of the 4^{th} generation of neutrinos is assumed to be 50GeV here [54]).

On the left plot of Figure 4.14 we found that the majority of Higgs particle will decay into a pair of 50GeV neutrinos in a wide mass range. We could use two parameters to distinguish the decay final state of a SM Higgs and an invisible decay Higgs. They are the total measured energy in one event and the number of tracks with energy bigger than 3GeV (marked with NTrk). The distribution of these two parameters for different events is shown in Figure 4.15.

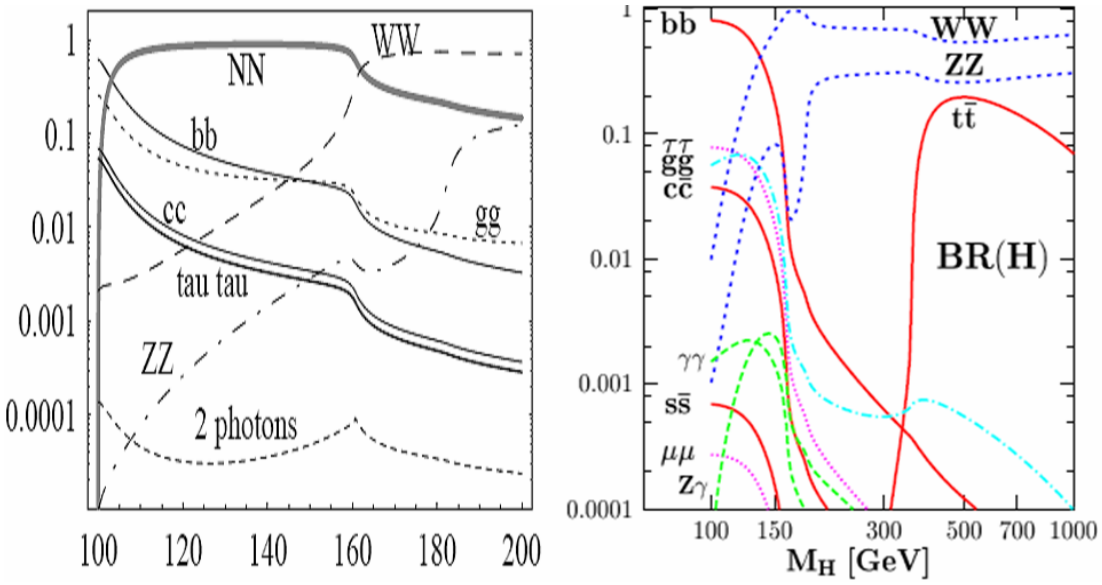

Figure 4.14 Decay branching ratios as a function of Higgs mass in different models. Left, model with a massive neutrino (50GeV); right, the SM

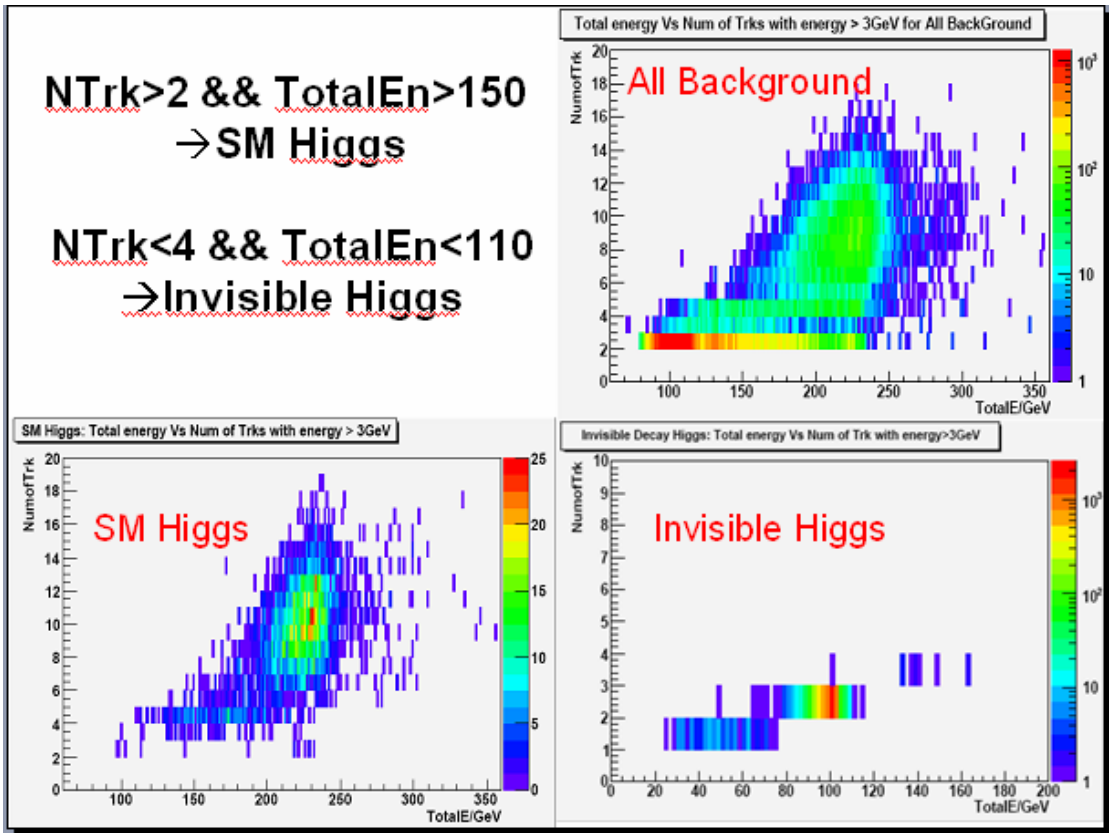

Figure 4.15 Distinguish the SM Higgs and invisible decay Higgs events with NTrk (Number of Tracks with energy large than 3GeV) and total energy

If NTrk > 2, and the total energy of the events is bigger than 150GeV, this event is regarded as a SM Higgs event (or corresponding background); on the contrary, if NTrk < 4 and the total energy less than 110GeV, this event is considered as an invisible decay Higgs event (or background). It is obvious that with the decay final state information we could have better event selection and achieve better result in our measurement. In the next section, we will discuss the Higgs mass and cross section measurement with a SM Higgs.

4.5.2 The Mass and cross section measurement for a SM Higgs

Same as in the model independent analysis, first we need to replace the precut:

2 μ particles identified	***2 μ particles identified***
E_1>15	***E_μ>20***
$2E_1+E_2$<180GeV	***$2E_1+E_2$<178GeV***
&& $2E_1+3E_2$>200GeV	***&& $2E_1+3E_2$>202GeV***
$\Delta\varphi < 177.6^o$	***$\Delta\varphi < 176.4^o$***
m_Z>70	***85 < m_Z <100***

To replace the precuts, we slightly relax the cut on ***Δφ*** in the SM Higgs analysis. Because, in the model independent analysis there is huge statistics of the μμγ background, we need a stringent cut on ***Δφ*** to reduce the μμγ background; while in the SM Higgs analysis, we could use other cuts to reduce the μμγ background. Comparing to the model independent analysis, relaxing the cut on ***Δφ*** will increase the signal statistics by 2%, while the purity is almost the same.

Followed the same sequence of the event selection parameter optimization, the event selection condition cuts for SM Higgs events are:

Both particles be identified as μ

E_μ>20GeV

$2E_1+E_2$<178GeV and $2E_1+3E_2$>202GeV

Δφ < 176.4°

The Invariance mass of μ system should between 85-100 GeV/c^2 (M_a>70GeV)

The Total event energy bigger than 150GeV

NTrk > 2 (NTrk, the number of tracks with energy > 3GeV)

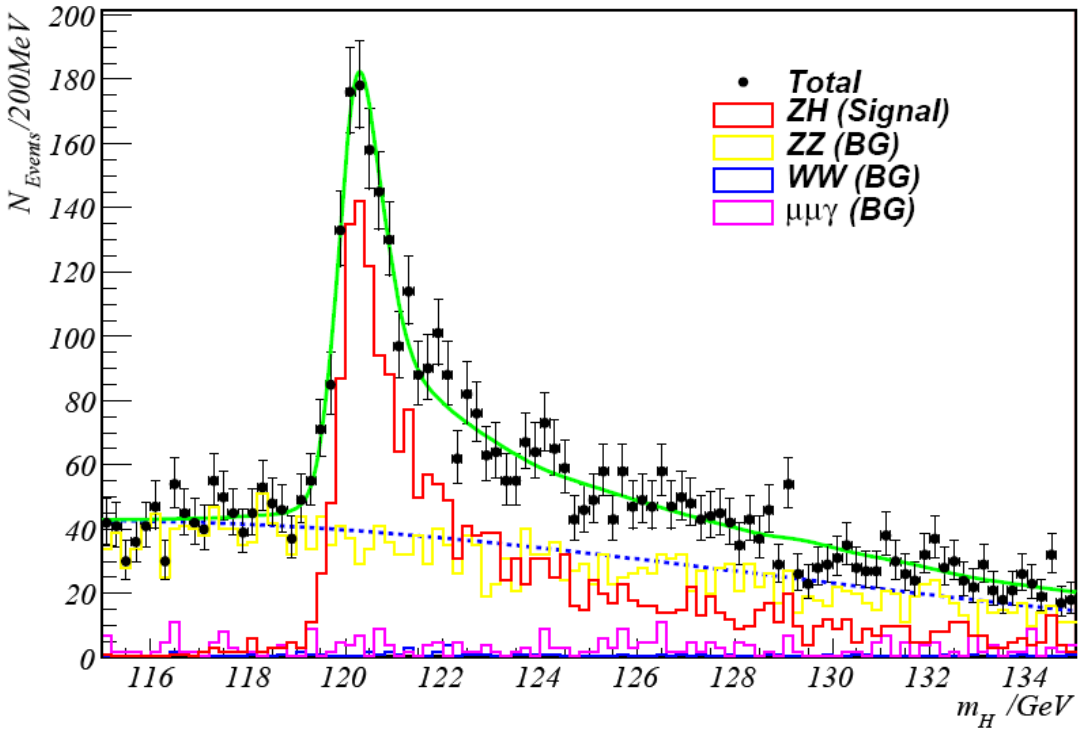

Figure 4.16 Fit to Higgs mass and cross section with SM Higgs

The total recoil mass spectrum after the event selection is shown in Figure 4.16. The background is now dominated by the ZZ events (with large recoil mass caused by the radiation effect), for the ZZ events have the same event geometry as the signal (if the Higgs mass is equal to the Z mass, we will not be able to distinguish these 2 events at all). In comparing to the model independent analysis, the statistics of the WW and μμγ background is largely reduced. This is because that the WW and μμγ events always have large missing energy (either through neutrinos or the ISR photon with very small polar angle), and cannot satisfy our requirement on the total energy.

The total event number in Figure 4.16 is 5239, with 3129 background events and 2110 signal events. The efficiency on event selection is about 64%, slightly larger

than our model independent analysis. The fit to the result is

m_h -120GeV = -13.72 ± 28.80MeV;

w = 40.46% ± 1.48% (the expectation value is 2110/5239 = 40.28%).

And the corresponding result on the mass an

d cross section measurements are:

m_h = 119.986 ± 0.029GeV

σ = 6.65fb ± 0.24fb (ignore the total statistic error)

or

σ = 6.65fb ± 0.26fb (taken the total statistic error into account).

Thus for a 120GeV SM Higgs, the mass could be measured to an accuracy of 28MeV, while the cross section measurement could reach a relative accuracy of 4% level. Comparing to the model independent analysis, this result is improved by 26%. In the next section, we will discuss the mass and cross section measurement with invisible decay Higgs.

4.5.3 The mass and cross section measurement for an invisible decay Higgs

Following the same sequence of replacing the precuts and optimizing the event selection parameters, the cuts for an invisible decay Higgs analysis are:

Both particles be identified as μ

E_μ>20

$2E_1+E_2<178GeV$ and $2E_1+3E_2>202GeV$

$\Delta\varphi < 175^o$

Invariance mass of μ system should between 85 - 100 GeV/c^2; (M_a>70GeV)

Total transverse momentum of μ system should be bigger than 15GeV

Total energy less than 110GeV

NTrk < 4

The recoil mass spectrum with the corresponding fit is shown in Figure 4.17. We have totally 4681 events with 1985 signal events.

As shown in Figure 4.17, with the assumption of Higgs invisible decay, the main background is WW events. The W boson could decay into a μ and a neutrino, so the event has a similar geometry as the signal; while the ZZ events also play an important role in the background, for the Z boson has a chance of 20% to decay into a pair of neutrinos. The μμγ background is greatly reduced by both requiring a large transverse momentum of the μ system and a small total energy (large transverse momentum of the μ system means we have an energetic photon with large polar angle, thus this photon could be detected, and the event cannot have large missing energy).

The fit result is:

m_h -120GeV = -3.95 ± 28.91MeV

w = 43.22% ± 1.59% (the expectation value is 1985/4681 = 42.4%).

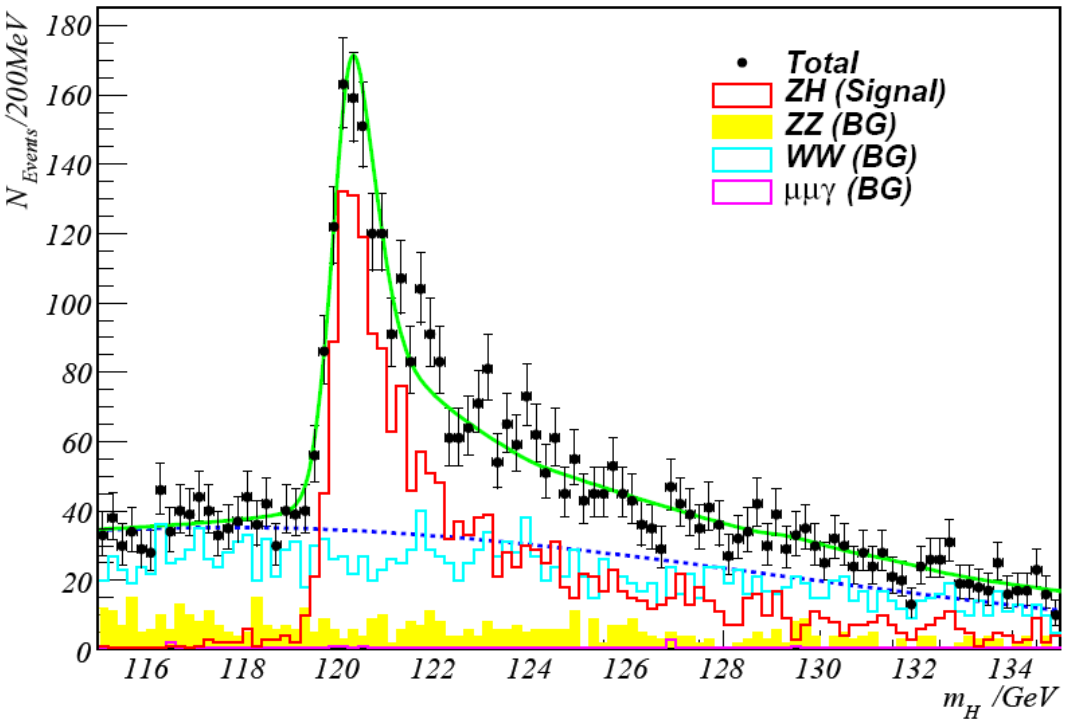

Figure 4.17 Higgs mass and cross section measurement for an invisible decay Higgs

And the corresponding results on the mass and cross section measurements are:

m_h = 119.996 ± 0.029GeV

σ = 6.80fb ± 0.25fb (ignore the total statistic error)

or

σ = 6.80fb ± 0.27fb (taken the total statistic error into account)

The result of the Higgs invisible decay analysis is comparable with the SM Higgs analysis. The accuracy of the Higgs mass measurement is 29MeV, and the relative error on the cross section measurement is 4%.

In the next section we will switch to the preliminary study of the beam parameter optimization/selection: let's consider the Higgs mass measurement in terms of machine parameters.

4.6 Preliminary study on the beam parameter optimization

Same as the detector optimization study, there exist a set of optimized beam parameters for different physical observable measurement, with which we could achieve better measurement performance and less machine time at the same time.

Our starting point for the beam parameter is the nominal beam parameter at 500GeV center-of-mass energy. As for the beam parameter optimization for Higgs recoil mass measurement (which might work at 230GeV center-of-mass energy as discussed in previous chapter), first, let's consider two different beam parameter selections.

First, keep the basic beam parameters (σ_z β_x β_y) constant for different center-of-mass energy. With this method, the luminosity is proportional to the centre-of-mass energy, while the BS effect is proportional to the square of center-of-mass energy. Thus, when we lower the center-of-mass energy from 500GeV to 230GeV, we will roughly have half of the luminosity with the same machine time (actually even less for at small center-of-mass energy we suffer more from the wake field luminosity reduction) and less than one

quarter of the beamstrahlung effect.

Second, we can scale our beam parameters with the center-of-mass energy. This method will provide us the same luminosity and the same strength of the beamstrahlung effect as for the 500GeV nominal beam. This is the method we have used in our full simulation study, which needs really strong Final Focusing (FF) system.

Of course there exist some other choices in between. Table 4.6 [55] are sets of the beam parameters the Beam Delivery System (BDS) group purposed. Their suggestion is much closer to the first method and relatively more realistic with our current technique.

There are eight sets of beam parameters in the BDS group proposal, including three center-of-mass energy (230GeV, 250GeV and 350GeV) and two sets of L*, which is the distance of the FF solenoid to the interaction point. With smaller L* the FF system could provide more powerful focus and result in larger luminosity, but the disadvantage is that we might need to install the FF system inside the detector. The CollX is also an important parameter, which is also called the field depth of the FF system. CollX<6 is regarded as a current technique limit for the FF system. η_L is the parameter we used to describe the wake field reduction of the luminosity, it increases with center-of-mass energy. The luminosity marked with the bold character is the luminosity we could achieve with the same machine time for us to achieve 500fb^{-1} integrated luminosity for the 500GeV nominal beam. And the last line of Table 4.6 (marked with blue character) is the fit result of the fast simulation (see chapter 3.4.2).

Sqrt(s)/GeV	230	230	250	250	350	350	350	350
L* /m	3.5	4.5	3.5	4.5	3.5	4.5	3.5	4.5
β_x /mm	22.7	29.2	20.9	26.9	15.0	19.2	20.3	20.5
ColliX	6	6	6	6	6	6	7.0	6.2
η_L /%	80.7	77.0	83.0	79.5	90.1	87.8	90.1	87.8
$L/10^{37}m^{-2}s^{-1}$	6.70	5.55	7.93	6.54	14.7	12.4	12.4	12.1
L /fb^{-1}	**181**	**150**	**214**	**177**	**397**	**335**	**335**	**327**
σ(Hμμ)/fb	7.03	7.06	7.81	7.83	4.80	4.80	4.78	4.80
N_events	1272	1059	1671	1386	1906	1608	1601	1570
δ(mH)/MeV	19.5	21.4	23.3	25.7	78.8	89.5	84.5	83.8

Table 4.6 Beam parameters purposed by the BDS group and the expected Higgs mass measurement accuracy [55]

By loading the beam parameters to the Guinea-Pig software package and using its output beam file as the input file for our generator, we could calculate the true value of corresponding recoil mass with all the radiation effect correction. Then, with the fast simulation package, by convoluting the true value of the Higgs recoil mass spectrum to the detector resolution, we get the expected recoil mass spectrum after reconstruction (See Figure 4.18, 4.19), and with a likelihood fit we can get the expectation value and expected measurement error on the Higgs mass.

The last line of Table 4.6 shows the expected error on the Higgs mass measurement for each set of beam parameters. When we ignore all the background, and assume the detector has a signal efficiency to 100%, we can achieve the best Higgs mass measurement at 230GeV, L*=3.5 meter. The corresponding mass measurement error is 19.5 MeV.

Interestingly, this 19.5MeV accuracy is comparable with the fit result to pure signal in our full simulation study, where we adopt the second method of beam parameter selection. Though for the latter case, we have much higher luminosity. That's because with the beam parameter purposed by the BDS group we have much

less beamstrahlung effect, and thus the events are much more concentrated to the main peak, which plays the most important role in Higgs mass measurement. Of course, with a comparable mass measurement accuracy and comparable cost, the method with higher luminosity is more attractive for we have more Higgs particles there – which will be important for the measurement of other Higgs particle properties.

And actually when we lower the center-of-mass energy, we have other methods to increase the luminosity. For example, we could increase the number of electron/positrons in the bunch, or increase the bunch number or frequency, etc. This is quite interesting and needs further study.

The beam parameter optimization, as well as the detector optimization study is very important and very complex. There are many possibilities and chances for us to achieve better physics result. For example, we could performance the same beam optimization study with fine energy bins. The optimization on beam parameters and detector parameters are the two closely related subjects, with only carefully considering together we could achieve the best performance.

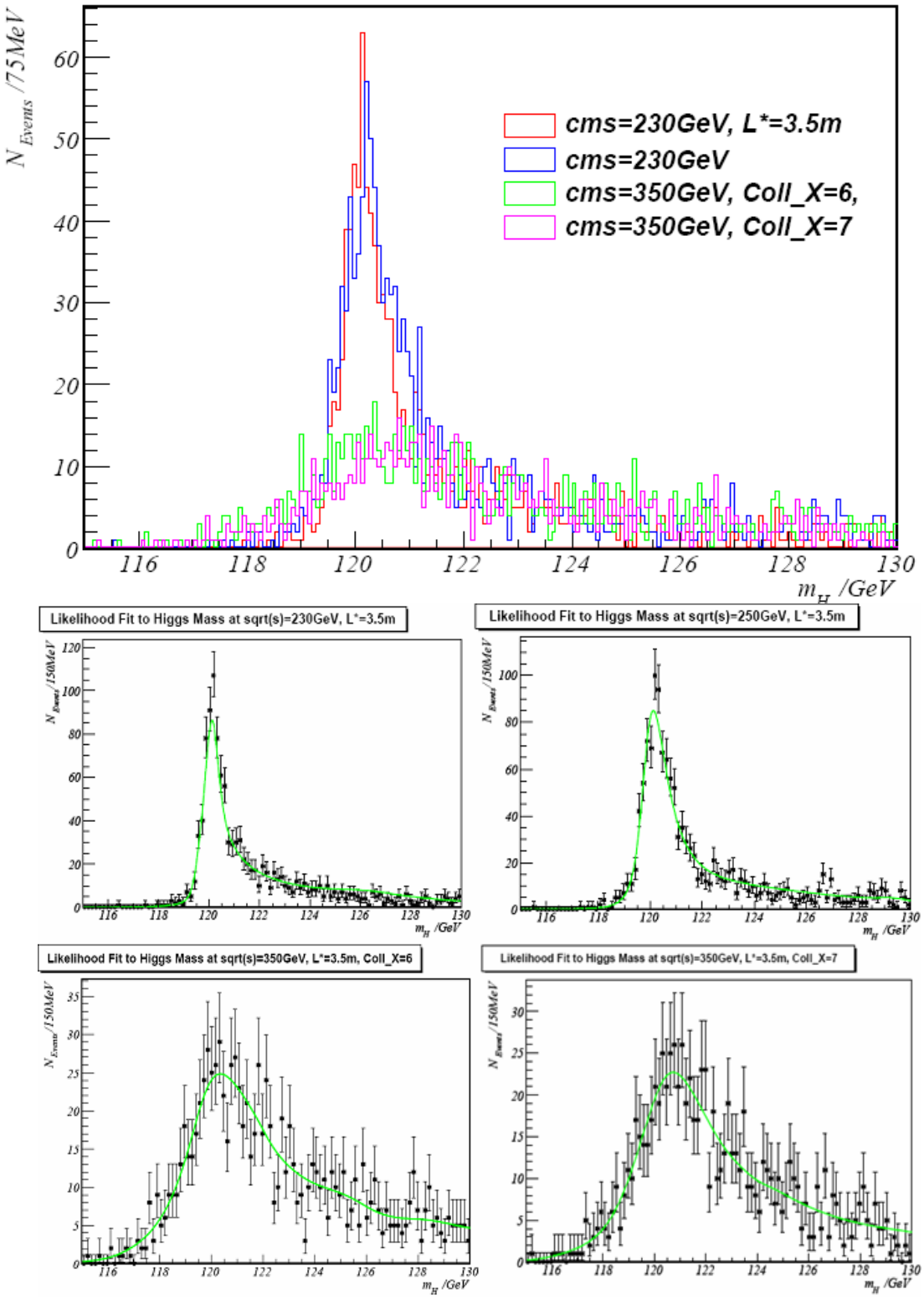

Figure 4.18 Fit to Higgs recoil mass spectrum with L*=3.5

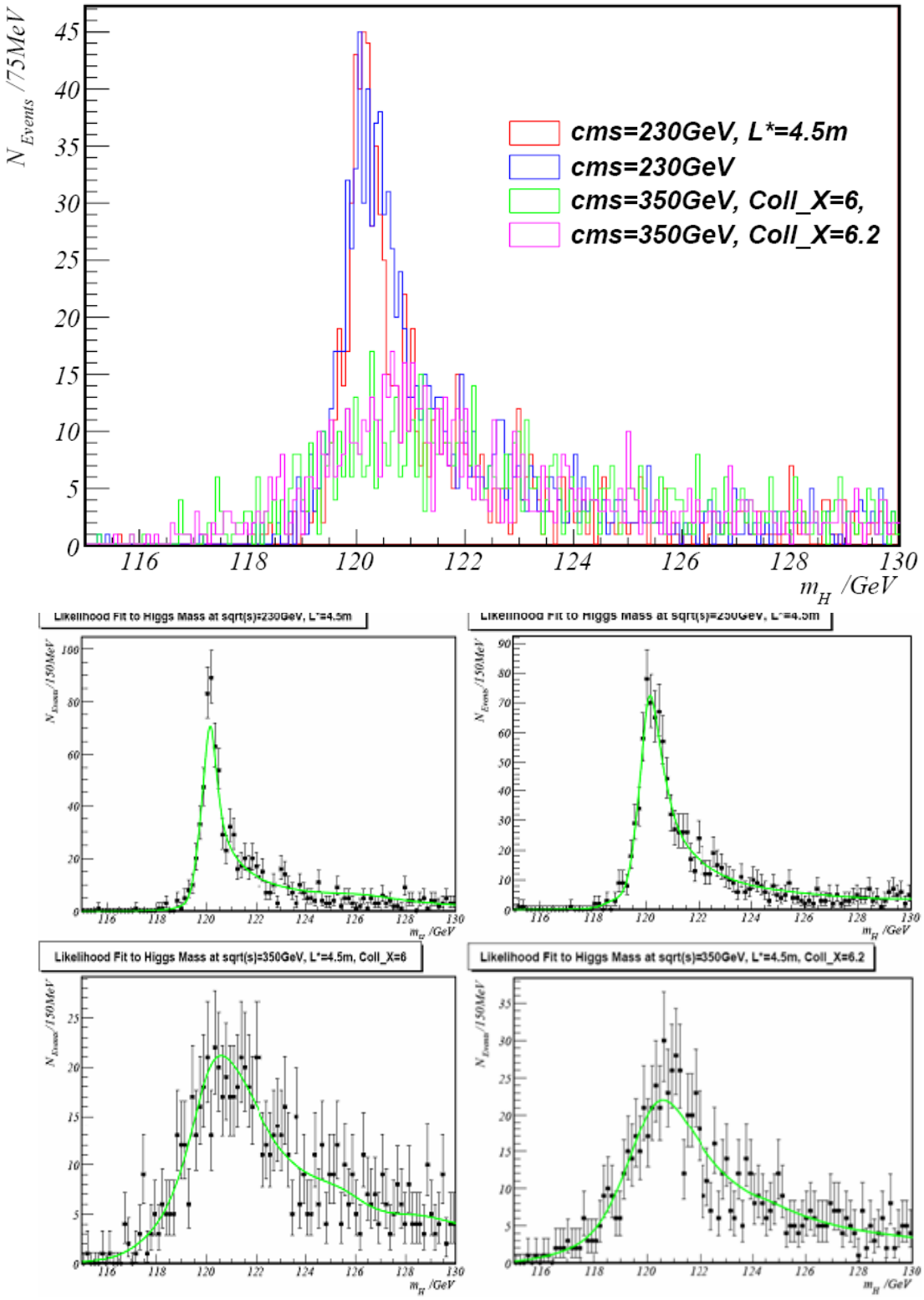

Figure 4.19 Fit to Higgs recoil mass spectrum with L*=4.5

4.5 Summary

In this chapter we have discussed the Higgs mass and cross section measurement through $e^+e^- \to HZ \to H\mu\mu$ process. The method we used here is the recoil mass method. Since the recoil mass method makes no assumption and no use of the Higgs decay information (we only need to know the center-of-mass energy and the 4-momentum information of the 2 μ particles), a model independent analysis could be applied by avoiding using any potentially model dependent event selection. And, by further assumptions on physical model (SM Higgs or invisible decay Higgs) we can get much powerful event selection and achieve better measured result.

The background we considered here includes the ZZ events, WW events, μμγ events and $q\bar{q}$ events. For the statistics of the backgrounds are huge, we introduced the precuts at generator level to reduce the number of events needed to be processed through the full simulation. After the precuts, we have totally 120k events, and we do the full simulation and reconstruction with the support or grid computing tools. In our analysis, all the radiation corrections (BS, ISR and FSR) have been considered.

For the model independent analysis, the Higgs mass measurement accuracy reaches 38.4MeV, and the relative error on cross section measurement is about 5%. When considering the Higgs decay final state information, the mass measurement improved to an accuracy of 28MeV – 29MeV, while the relative error on cross section is about 4%. See Table 4.7.

	Mass measurement	Cross section measurement
Model independent analysis	119.992 ± 0.038GeV	6.53fb ± 0.35 fb
SM Higgs analysis	119.986 ± 0.029GeV	6.65fb ± 0.24 fb
Invisible Higgs analysis	119.996 ± 0.029GeV	6.80 fb ± 0.25 fb

Table 4.7 result of the Higgs mass and cross section measurement

The beam is non-polarized in this analysis, if we assume the default polarized beam in ILC beam parameter (electron beam 80% polarized, positron beam 60% polarized), the WW background will be greatly suppressed (for the W boson only

couples to left-handed electron), and the statistics of our signal could increase by 58% (in the SM the coupling of the Z boson to left hand and right hand electrons are not the same due to the parity violation of weak interaction. The effect of the beam polarization on the signal cross section could be seen in Figure 2.4). As for the detector concept, we use the minimal LDC detector concept (LDC01_Sc), with smaller TPC, minimal silicon tracker (only has VTX and 2-layer SIT, no SET or ETD in between the TPC and ECAL) and no μ tracker installed in the YOKE. So our result is expected to improve a lot by using a more complete detector and the polarized beams.

Based on the knowledge of the beam effect we introduced in Chapter 3.5.2, a preliminary study on the beam parameter optimization for the Higgs recoil mass measurement has been carried out with beam parameters proposed by the BDS group. Same as for the detector optimization study, the beam parameter optimization study for different physical purposes is very important. The analysis is done at fast simulation level with the package developed by ourselves. In all the eight sets of proposed beam parameters, the best Higgs mass measurement is achieved with 230GeV center-of-mass energy and 3.5m L* (L* is the distance between interaction point to the FF system). This conclusion also supports our choice of 230GeV center-of-mass energy in our full simulation study (in comparing to 250GeV or 350GeV center-of-mass energy).

So far we have finished our discussion on the Higgs mass measurement study with Monte Carlo simulation, in the next chapter we are going to discuss the CALICE test beam experiment and its data analysis.

Chapter 5 Introduction to the CALICE test beam experiment

5.1 A brief introduction to the CALICE project

Most of the benchmark channels at the ILC have jet final states, see table 1.1. The ILC detector is required to be able to precisely measure the jet energy down to $0.3/\sqrt{E/GeV}$, at which we could easily identify the jets generated from the hadronic decay final states of W and Z bosons, see Figurer 5.1 [56].

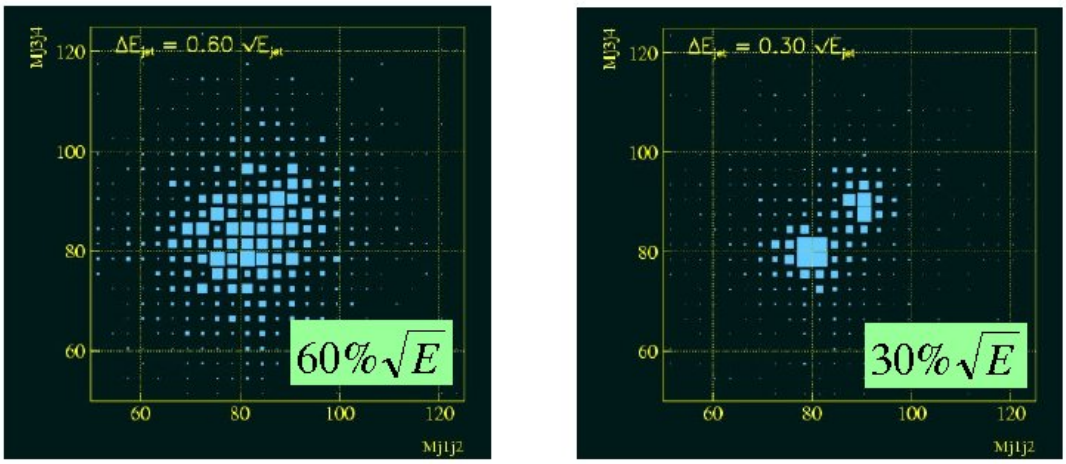

Figure 5.1 Reconstructed invariance mass of Z/W boson for ZZ/WW events with hadronic decay final state for 2 jets resolution

$0.3/\sqrt{E/GeV}$ jet energy resolution accuracy is roughly a factor two better than what we have achieved in previous LEP experiment. One way to reach this accuracy is the particle flow analysis (PFA), which requires a calorimetry system with high capability on the pattern recognition to identify the energy deposition from different sources. To construct an optimum calorimeter for the ILC, the CALICE collaboration has been formed.

The CALICE collaboration consists of over 200 physicists of 42 institutes from 12 different countries. A prototype of the ILC calorimetry system, which contains the

ECAL, HCAL and TCMT (Tail catcher and Muon Tracker), has been constructed, see Figure 5.2. The basic motivations of the CALICE project are twofold[57]:

1, To construct realistic prototype calorimeters and test their performance;

2, To confront the data with Monte Carlo simulation of the same kind as used for the full detector.

Since 2005 the CALICE collaboration has organized four test beam experiments. For the test beam data taking, besides the calorimetry prototype, some other detectors such as Cerekov detector (used for Particle identification), tracking system (consists of 3 or 4 pairs of Drift chambers) and the scitillator trigger system have been used. Now let's introduce the different components of the calorimeter prototype (The ECAL, HCAL and TCMT).

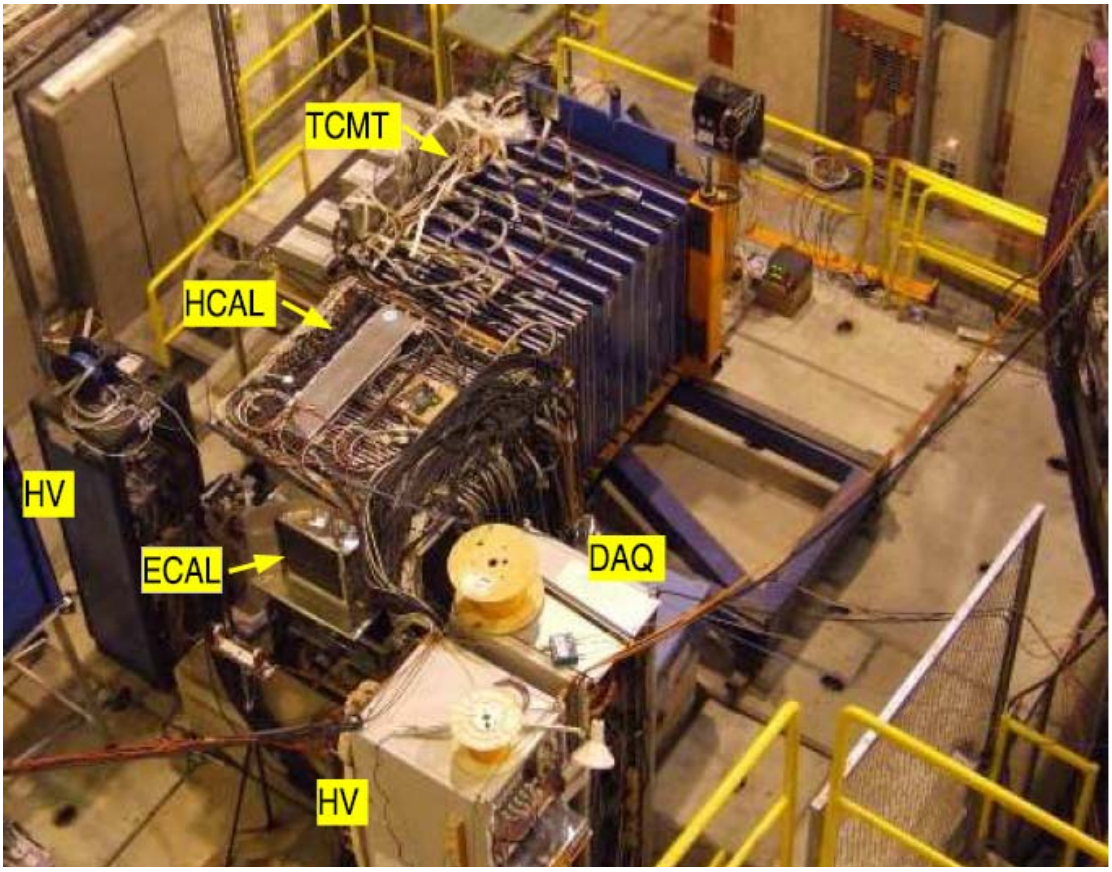

Figure 5.2 CALICE test beam experiment setup (Oct, 2006)

5.2 Introduction to the prototype subdetectors

5.2.1 The ECAL

The ECAL has a silicon-tungsten sandwich structure as illustrated in Figure 5.3 **[ref5.5]**. The tungsten is a very good absorber, with a very short radiation length as low as 3.5mm, which is about 1/3 of the lead radiation length. By using tungsten as the absorber, we could make a very compact ECAL. The silicon sensor ensures good energy resolution. The size of effective area of the ECAL is 18cm×18cm×20cm.

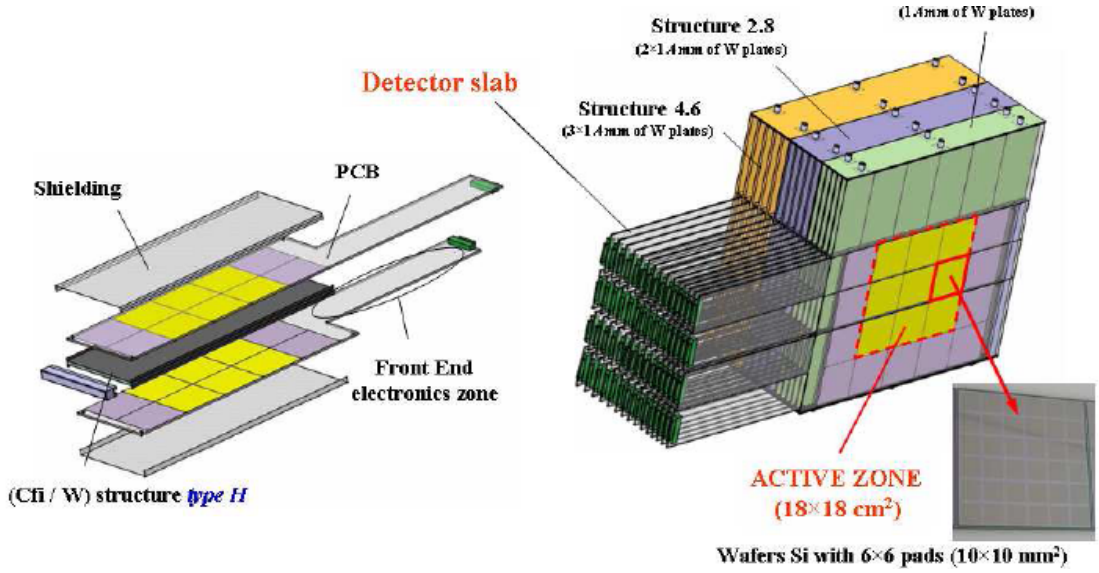

Figure 5.3 Schematic view of the ECAL in the CALICE test beam experiment

The ECAL is divided into 30 layers in the longitudinal direction with total depth of 24 radiation lengths. To achieve a better shower energy/spatial resolution, the absorber thickness for each layer is not identical. For the first, second and last 10 layers, the tungsten thickness is 1.4mm, 2.8mm and 4.2mm respectively (with ratio 1:2:3). In the transverse plane, each layer of the silicon sensor contains 9 wafers with the size of 6cm×6cm, and each wafer consists of 36 1cm×1cm cells, each cell is connected to a VFE (Very Front Ending) electronic channel. For every wafer there are 2 VFE chips, responsible for 18 channels each. For each layer, the 9 wafers are divided into two groups, with one group of 2×3 wafers and the other 1×3 wafers, installed on two Printed Circuit Boards (PCB). In total, the number of electronic

channels on ECAL is 36×9×30＝9720. For each wafer, there is a guide-ring with width = 1mm at the edge, so there is a 2mm wide dead zone in between the wafers, which causes energy loss as a systematic effect. We will discuss this effect in section 6.3.

The cell position in the Y direction for different layers are all identical, while in the X direction there are some shifts between different layers – for example, a 2mm shift between the odd and even layers. In some runs the ECAL is rotated in the X direction for beam to inject with different angles, and meaning while the ECAL layers are shifted in X direction to fully contain the shower profile, see Figure 5.4.

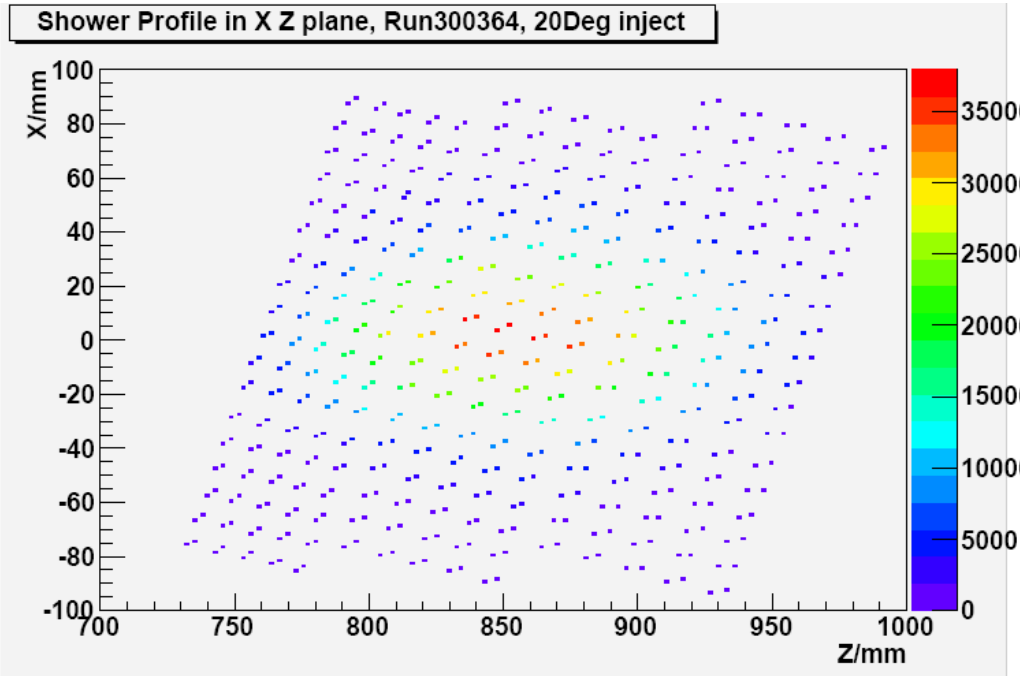

Figure 5.4 The ECAL layer shifts in X directions for 20 degree inject beam

Because the manufactory, test and calibration of each sensor layer take time, we did not have a fully equipped ECAL till 2007 (even then the first 6 layers of the ECAL have only equipped with a PCB contain 6 wafers). And the situation is similar for the HCAL.

5.2.2 The HCAL and TCMT

The absorber in the CALICE HCAL is iron, while the sensor is scintillator. Photons are created when a charged particle passes through the scintillator. The photons are collected by optical fibers and delivered to the photoelectric cell. The size of the HCAL effective area is 90cm×90cm×120cm. In the longitudinal direction, the HCAL has in total 4.5 interaction lengths, and is divided into 38 layers. In each layer, we have 2cm thick iron absorber and 5mm thick scintillator. On the transverse plane, the structure is more complex (see Figure 5.5). For the first 30 layers, in the central part of each sensor layer, the cell size is 3cm×3cm; while going from the center to the edge, the cell size is increased to 6cm×6cm and 12cm×12cm, on each layer we have 216 electronic channels. For the last 8 layers, there have only the 6cm ×6cm and 12cm×12cm cells, with 141 channels on each layer. So in total we have 7608 channels of electronics on the HCAL [58].

Figure 5.5 The HCAL structure for the CALICE test beam experiment

Comparing to the ECAL and HCAL, the TCMT [59] has relative simple structure and the total number of electronic channels on the TCMT is much smaller. The TCMT also adopts the iron-scntillator sandwich structure, and the size of the TCMT effective area is 100cm×100cm×120cm. In the longitudinal direction, it is divided into 16 layers, for the fist 8 layers, the absorber thickness is 19mm, while for the last 8 layers is 102mm. The size of each sensor layer is 100cm×100cm×0.5cm. The

sensor layer is divided into 20 strips with 5cm width in the X/Y direction for odd/even layers. We have in total 320 electronic channels in the TCMT.

Beside what we introduced above, there are some other calorimetry prototypes joining the CALICE test beam experiment. For example, Our Japanese colleagues constructed a tungsten-scitillator strips ECAL [60], and there is a DHCAL [61] proposal with very high HCAL spatial granularity but without the ADC information for each channel (we have huge number of electronic channels in the DHCAL concept, while for each channel, we only use 1 bit to record the information if this channel has been hit or not). The CALICE collaboration is making efforts in various directions to searching for the best design of the ILC calorimetry system.

5.3 The CALICE test beam experiment setup

Taking the test beam experiment that has been held at CERN between July-August, 2007 as an example, let's briefly introduce the setup of the CALICE test beam experiment.

This test beam experiment was located at the H6 [62] test beam zone of CERN Prevessin region. The beam source was the high energy proton beams in SPS. With tuning the magnetic solenoids and different targets/absorber, we could get electron, hadron and μ beams with energies from 10GeV to 180GeV. And by rotating the prototype, we can have beams injecting at different angles.

Figure 5.6 shows a schematic view of this experiment setting up [63]. The red line here indicates the beam, which is injected from the left-hand side, after a Cerenkov detector (with length ~ 11m), a scintillator trigger system and a tracking system (consisting of 3 pairs of drift chambers), the beam injects into the calorimetry system. From left to right, the calorimetry system consists of the ECAL, the HCAL and the TCMT. After the TCMT, there is a scintllator with area of 1000mm×1000mm (Mc1), used for the trigger of μ events. The trigger system before the calorimeter consists of four scitllators, named with Sc1 – Sc4. Sc1 and Sc3 have the size of 100mm×100mm, they are used for the beam event trigger: if both Sc1 and Sc3 are hit in one event, the event is identified

as a beam event. The Sc4 is a scintillator used to veto the events with large scattering angles, it has the size of 1000mm×1000mm, and there is a hole of 200mm×200mm in the center. The size of Sc2 is 200mm×200mm, Sc2 is located precisely in the hole of Sc4 in the transverse plane – so combine the information from the Sc2 and Sc4, we could identify the events with pre-shower (hit both Sc2 and Sc4) or with large scattering angle (hit only Sc4).

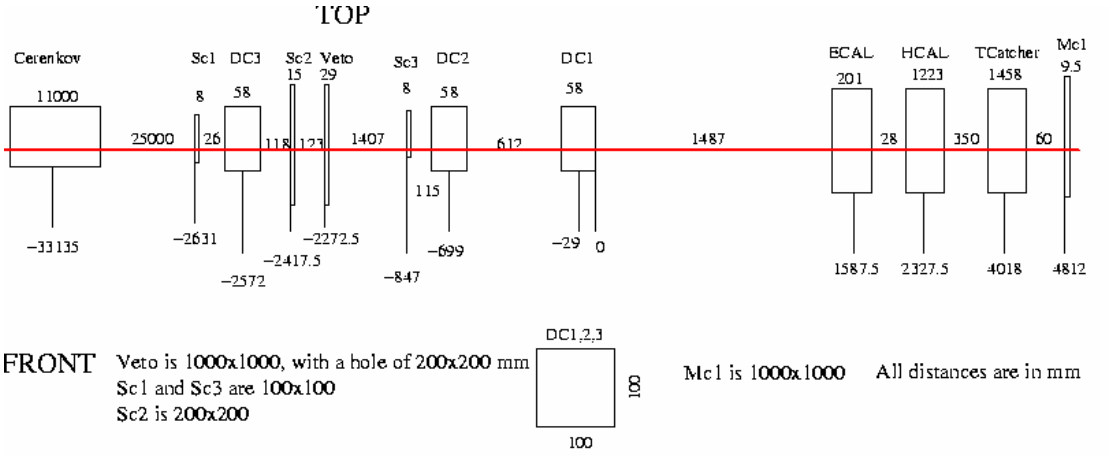

Figure 5.6 Test beam experimental setup (July-August, 2007, CERN)

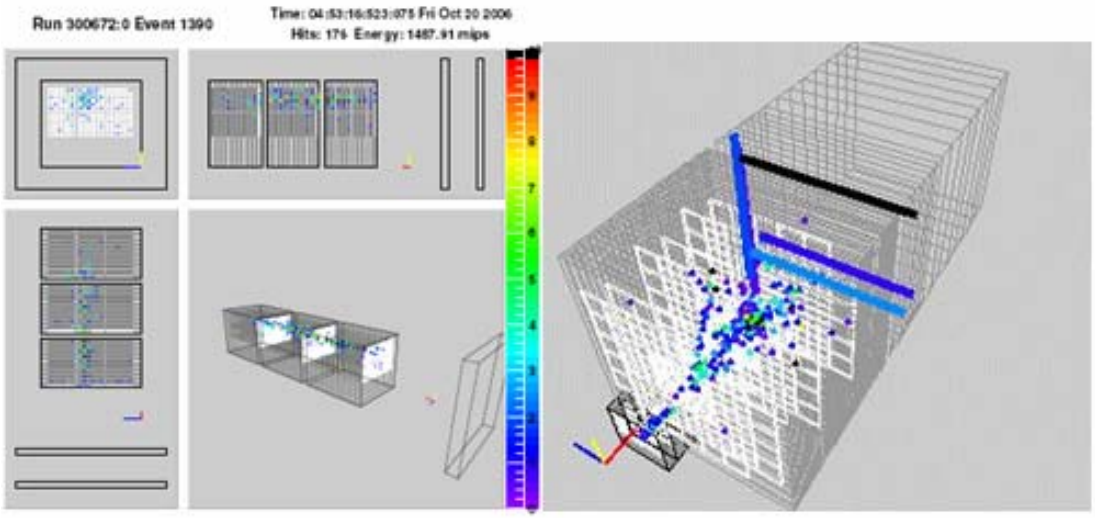

Figure 5.7 Online monitoring system for the test beam experiment (left，monitoring for the ECAL；right，monitoring for the whole calorimetry system)

For the data taking of each run in the test beam experiment, at least 3 members of the CALICE collaboration are presented to take shift at the control room. The experimental conditions and corresponding information are recorded both to the notes and to the webpage (elog, https://ttfinfo.desy.de/CALICEelog-sec). A very powerful online monitoring system has been developed (mainly by G.Mavromanolakis of Cambridge University) for the test beam experiment (see Figure 5.7)[57], by which the shift crew can easily monitor the status of data taking. This monitoring system can also record the basic information for each run to a root file, making it easier for the on-line data analysis. For example, Figure 5.8 shows the online ECAL/HCAL energy resolution as a function of time [64], from which we can see that even without the offline cleaning and correction, the linearity and stability of the ECAL/HCAL is very good (done by Allister Levi Sanchez from LLR, this work, as well as my data quality check, are regarded as the most important works during this shift – and we are rewarded with a special gift, a bottle of honey, whose name is coincidently CALICE as well).

This test beam experiment lasted for 7 weeks and has taken over 15 Tb of data, including 14 Tb of ECAL + HCAL data and 1 Tb of HCAL only data. Figure 5.9 shows some overall information of the data taking. We have spent on the shifts over 418 people-times and have collected data far beyond our expectation (see Table 5.2). The data that we have taken include [65]:

π runs with energy 6 – 180GeV and injection angle 0^o, 10^o, 20^o;
electron runs with energy 6 – 50GeV and injection angle 0^o, 10^o, 20^o;
HCAL only runs with electron and π beam, energy 6 – 50GeV.

Besides, we have taken the data for some specific purposes. For example, the correction for the effect of the dead zone in between wafers; and the irradiation effect of chips, etc. the data are being analyzed.

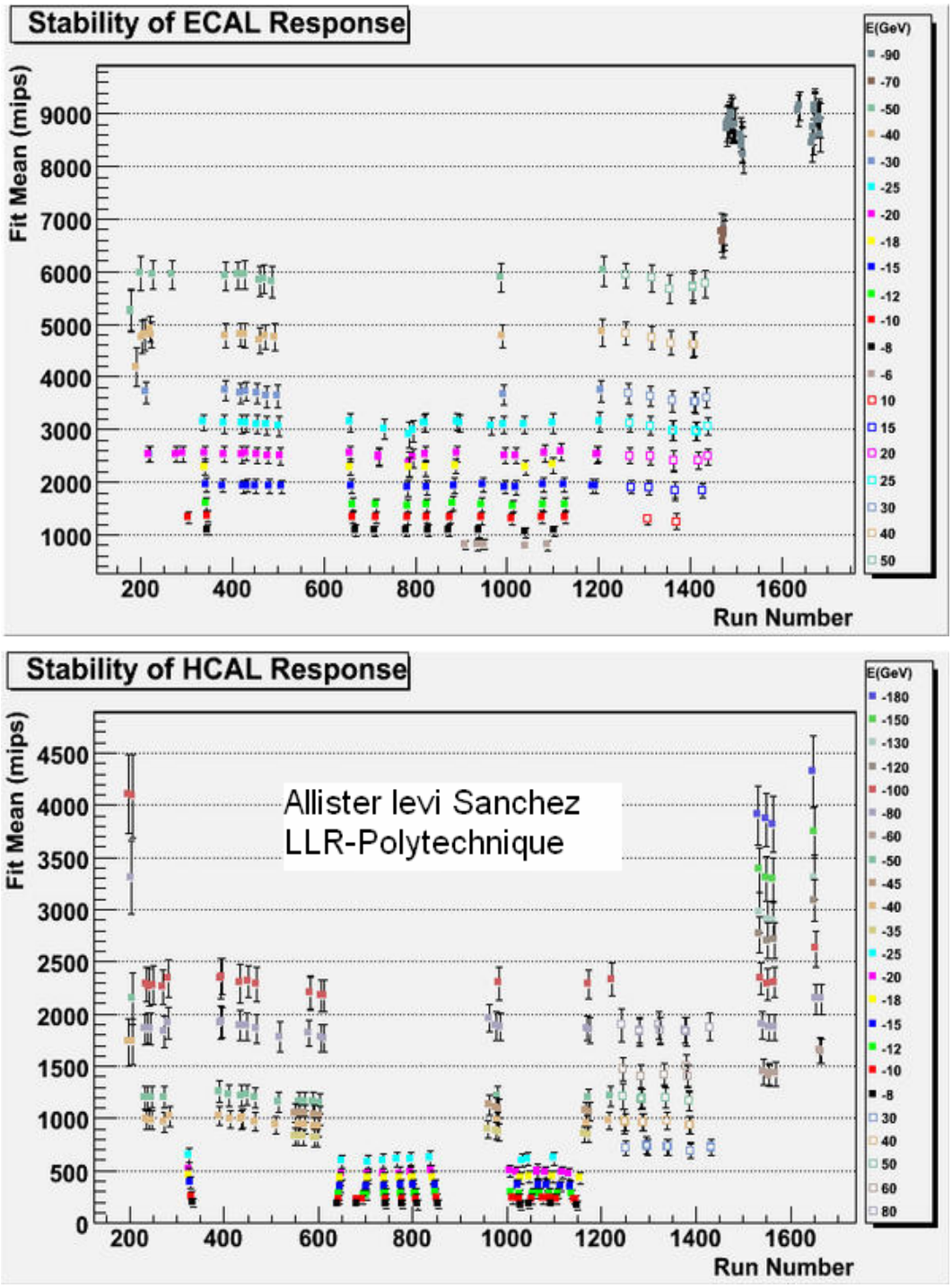

Figure 5.8 The stability of ECAL/HCAL response (July-August, 2007, CERN)

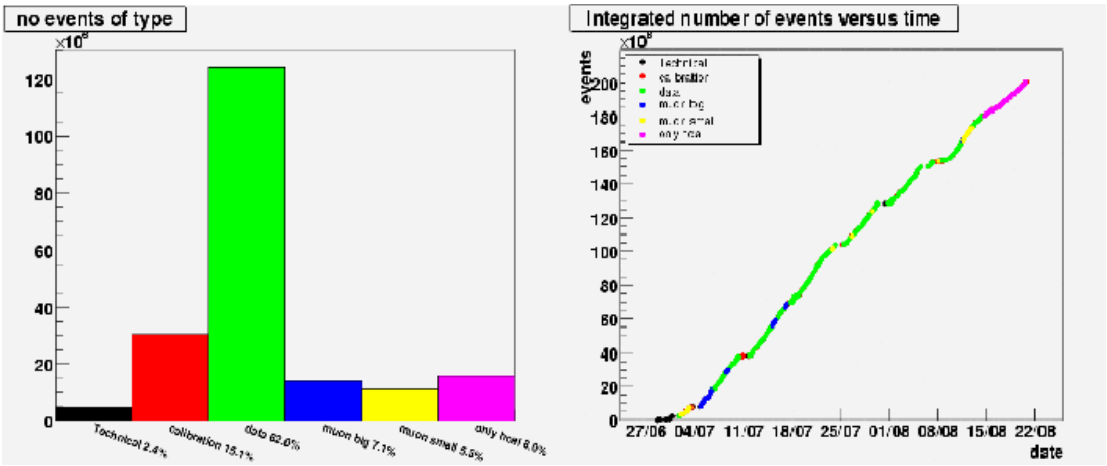

Figure 5.9 Brief summaries for the data taking condition (July-August, 2007, CERN) [65]

Since 2005 the CALICE collaboration has organized four test beam experiments. The basic information has been summarized in Table 5.1. The beam sources we have used are the DESY electron beam [66] with energy 1 – 6 GeV, the H6 CERN beam and we will use the MT7 beam [67] at the Fermi National Accelerator Lab (FNAL, provides low-energy hadron beam) in the summer of 2008, thus we can get a full spectrum of the calorimetry system performance.

	Time	Beam type	Energy range	Setting up
DESY0205	Feb, 2005	e	1－6GeV	14-layer ECAL
DESY0506	May, 2006	e	1－6GeV	24-layer ECAL
CERN1006	Aug-Oct, 2006	e，π，μ	10－80GeV	30-layer ECAL 26-layer HCAL
CERN0707	July-Aug, 2007	e，π，μ，p	10－180GeV	30-layer ECAL 28-layer HCAL

Table 5.1 Basic information of previous CALICE test beam experiments

In the next section, we will describe the data taking and the data quality check of the CALICE test beam experiment.

	Proposed in TB plan (4 weeks of data taking)	Acheved at the TB (7 weeks of data taking)
Combined physics package: low energy π	π^-: 1M evts @ 6/8/10/12/15/18/20 GeV, 0 deg π^-: 500K evts @ 6/10/12/15/18/20 GeV; 10, 15, 20, 30 deg	- π^-: 1M evts @ 6 GeV, 0 deg; - 1.75M evts @ 8/10/12/15/18/20 GeV, 0 deg. - π^-: 400K evts @ 6/10/12/15/18/20 GeV, 10 deg; - 1M evts @ 6 GeV; 500K evts @ 8-20 GeV, 20 deg.
Combined physics package: high energy π	π^-: 1M evts @ 25/30/40/50 GeV, 0 deg π^-: 500K evts @ 25/30/40/50 GeV; 20, 30 deg	- π^-: 1.5M evts @ 25/40/50/60/80/100/120/130/150/180 GeV, 0 deg; - 200K evts @ 5/40/45/50/80/100 GeV, 0 deg: ECAL on beam line, AHCAL displaced by 6 cm. - π^-: 200K evts @ 35/40/45/50/80/100 GeV, 10,20 deg.
ECAL physics package: low energy e	e^-: 1M evts@6/10/15(/20), 0 deg	- e^-: 1M evts @ 6 GeV, 0 deg; ~700K evts @ 8/10/12/15/18/20 GeV, 0 deg. - 1M evts @ 6 GeV, 20 deg; ~400K evts @ 8/10/12/15/18/20 GeV, 10, 20 deg.
ECAL physics package: high energy e		- e^-: ~2M evts @ 25/30/40/50 GeV, 0 deg; - ~200K evts @ 25/30/40/50 GeV, 10, 20 deg.
ECAL physics package: high energy e		- e^-: scan of the bottom ECAL layer; ~250K evts @ 90 GeV/pos, 0 deg.
ECAL irradiation package: high energy e	e^-: 1M evts@10/50 GeV, 0 deg	- e^-: ~1.1M evts@70 GeV, 0 deg; - > 5.5M events @ 90 GeV, 0 deg. Position scanning on chip.
ECAL inter-alveolae package: high energy e	e^-: 300M evts@20/50 GeV, 0 deg	- e^-: ~2M evts @ 8/10/12/15/18/20/25/30/40/50 GeV, 0 deg; 6 positions.
AHCAL only package: e/π, all energies	e/π^-: 500-1M evts @ 6/10/15/20/25/30/40/50 GeV, 0 deg	- π^-: 100K evts @ 8/10/12/15/20 GeV, 30 deg; - e^-: 100K evts@6/10/15/20 GeV, 30 deg; - π^+: 400K evts @ 10/15/20/25/30/40/50 GeV, 0, 10, 20, 30 deg; - e^+: 400K evts @ 10/15/20/25/30/40/50 GeV, 0, 10, 20, 30 deg.
π^+/e^+/protons		- e^+: 1.5M evts @ 10/15/20/25/30/40/50 GeV, 0 deg; - π^+/protons 1.5M evts @ 30/40/50/60/80 GeV, 0 deg: position scanning on ECAL front face.

Table 5.2 Status of the CALICE test beam data taking (CERN0707) [65]

5.4 The data acquisition and data flow of the CALICE test beam experiment

In the test beam experiment, the data acquisition system first writes the electronic signal from the detector to a binary file. The binary files (divided into 2 GB in size each) were first stored in a hard-disk cluster in the control room, and at the same time the data format transformation and reconstruction through the grid computing is processed.

The binary files are first transformed into the standard format of slcio files. The latter files contain the ADC value of each channel and some global run parameters. After the pedestal subtraction and calibration, the information is reconstructed into calorimeter hits. The data (the binary file, the transformed slcio file and the reconstructed file) are transported to the grid storing elements and any member of the CALICE collaboration could access these data files through the CALICE Virtual Organization (VO).

5.4.1 The ECAL Calibration

The calibration constant for each ECAL channel is obtained from the cosmic ray experiments and the μ events data in the test beam experiment (while for the on-line monitoring and analysis, we use calibration constants calculated from previous data). After the pedestal subtraction, a hit with more than 25 ADC values is regarded as an effective hit. Since 1 mip is about 50 ADC value, this condition is about 0.5 mip cut. The following conditions are used for the μ event selection[57];

First, the number of effective hits should between 15 and 40 (totally 30 layers);

Second, the projection of these hits on the transverse plane should be within 2 cm distance on both directions.

In total we have collected over 10M μ events in CERN 2007 test beam experiment.

For a single ECAL cell, the distribution of energy deposition of a μ event could be regarded as a Gaussian distribution convolute with a Landau distribution, see Figure 5.10. The most probable value of this distribution is defined as the calibration

constant of this channel.

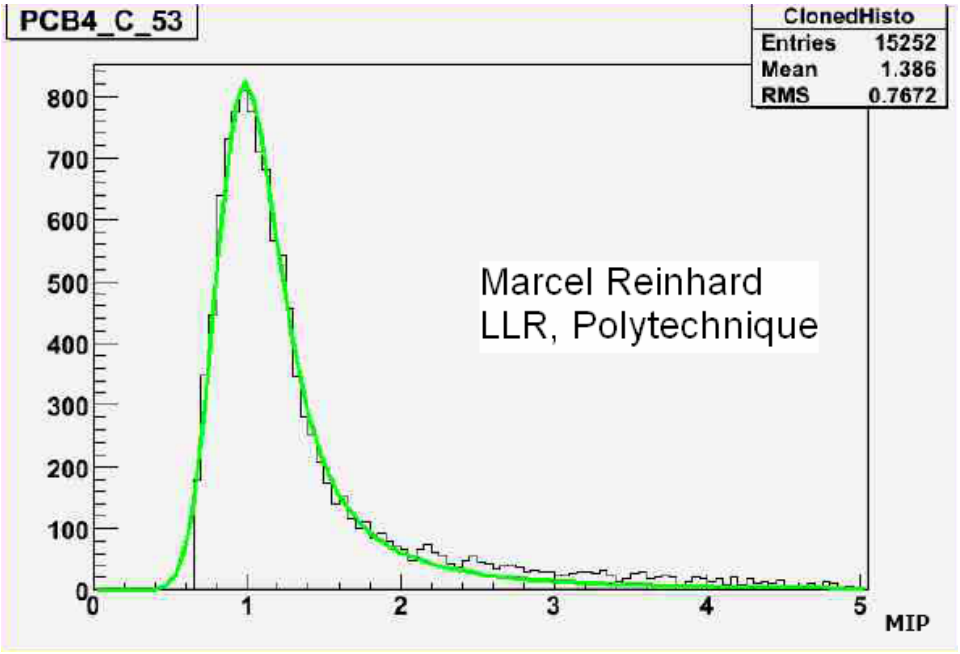

Figure 5.10 Energy depositions of μ events for a single cell: Landau + Gaussian

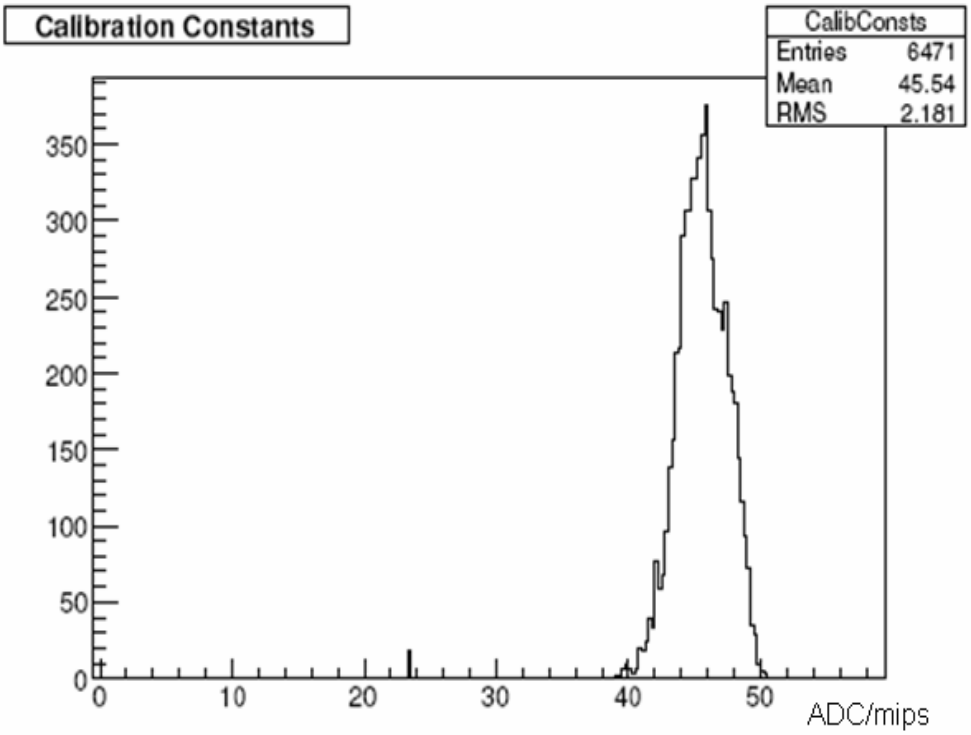

Figure 5.11 Distribution of calibration constant for ECAL cells [57]

Figure 5.11 shows the calibration constants for all the ECAL channels of the test beam experiment in the summer of 2006. At that time each ECAL layer is equipped with a 6-wafer PCB only. So in total we have 12×18×30＝6480 electronic channels. Besides 9 dead channels, almost all the calibration constants have value between 40-50ADC/mips (here the small peak at 23.5 ADC/Mip is caused by an abnormal VFE chip).

5.4.2 Noise level

In the test beam experiment, the data taking sequence for any beam run is like following: first we take 500 pedestal events and 500 calibration events with charged current injected into the chips, and then we collect 20k beam events. This sequence is repeated till the end of the run. During the pedestal events taking, we veto the event with the highest totally energy deposition in every 20 events to avoid possible beam event. For each cell, the mean value of these 500 pedestal events is used to calculate the pedestal constant (the pedestal constant is defined as a weighted sum of previous pedestal value and the value determined with current 500 events), while the RMS of the 500 events is defined as the noise level.

The noise level is usually around 6 ADC values, and it is quite stable in time, see Figure 5.12 [57].

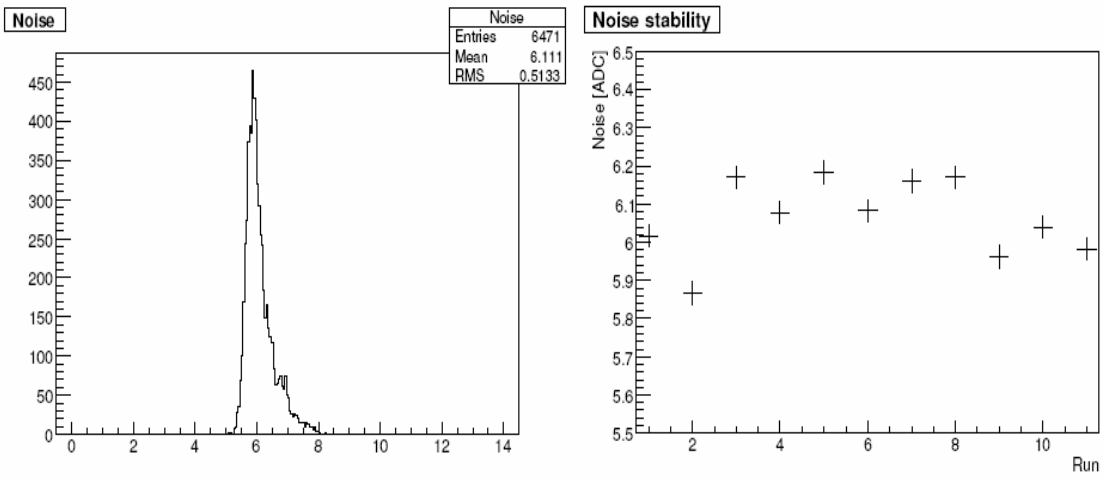

Figure 5.12 Noise level for each ECAL cell and the noise stability [57]

5.4.3 The data quality check

In the CALICE test beam experiment many efforts have been made to ensure the high quality of data. For example, to avoid possible mismatching of the beam condition setting, the parameters (different type of target/absorber, magnetic field strength, collimator setting, etc) are recorded into files, we only need to load the corresponding file when we need a certain type of beam. The online monitoring system has the alert system for almost any known errors. However, the data quality check, a careful scan over all the reconstructed files, is still needed. By the data quality check we could discover any strange pattern beyond our expectation (and then inform the experts), and we could have a summary and classification for all the runs, which is very helpful for the later data analysis work.

Because of the huge amount of data, the grid tools are very important for the data quality check. The process of data quality check is straight forward, for every run we generate a root file containing the basic information (see Figure 5.13), and check if there has any strange pattern.

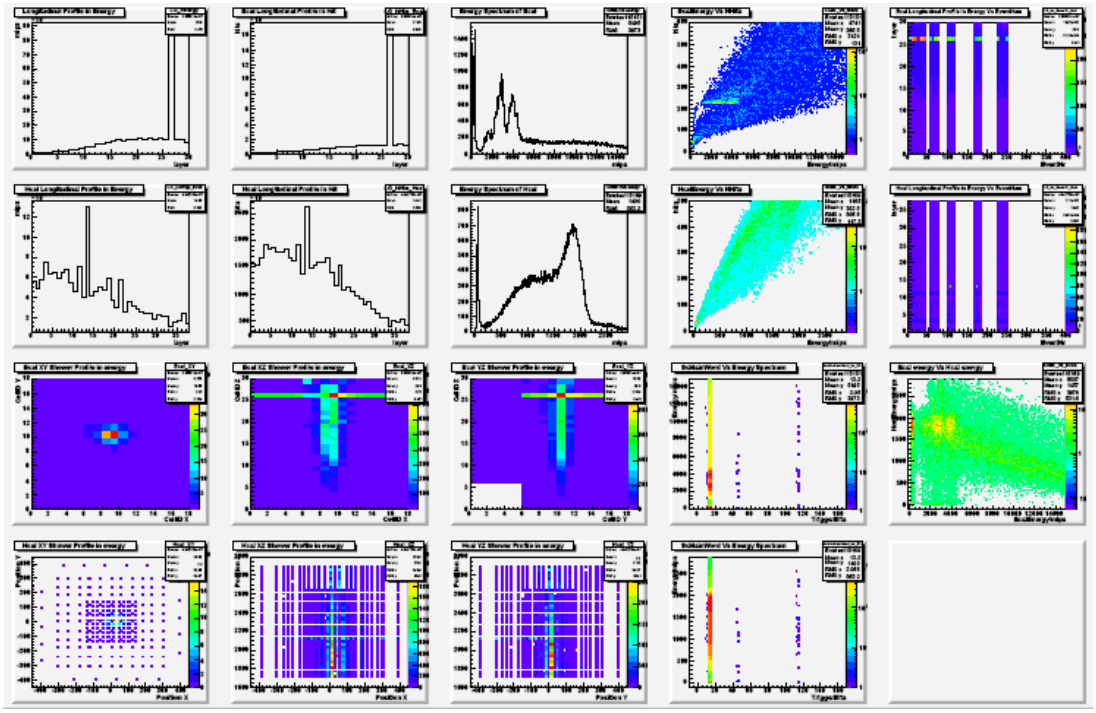

Figure 5.13 Data quality check on Run331241, from which we could see huge noise on both ECAL and HCAL, while the beam is also not stable

There are many strange patterns observed through the data quality check, i.e.:

1. Time dependent noise, VFE dependent noise and PCB dependent noise;
2. Energy loss in the last ECAL layer;
3. Low energy noise in the ECAL;
4. Unstable beam;
5. Systematic energy loss caused by the dead zone between ECAL wafers;
6. Wrong setting of experimental condition (very few runs);

Now let's discuss some of the important strange patterns.

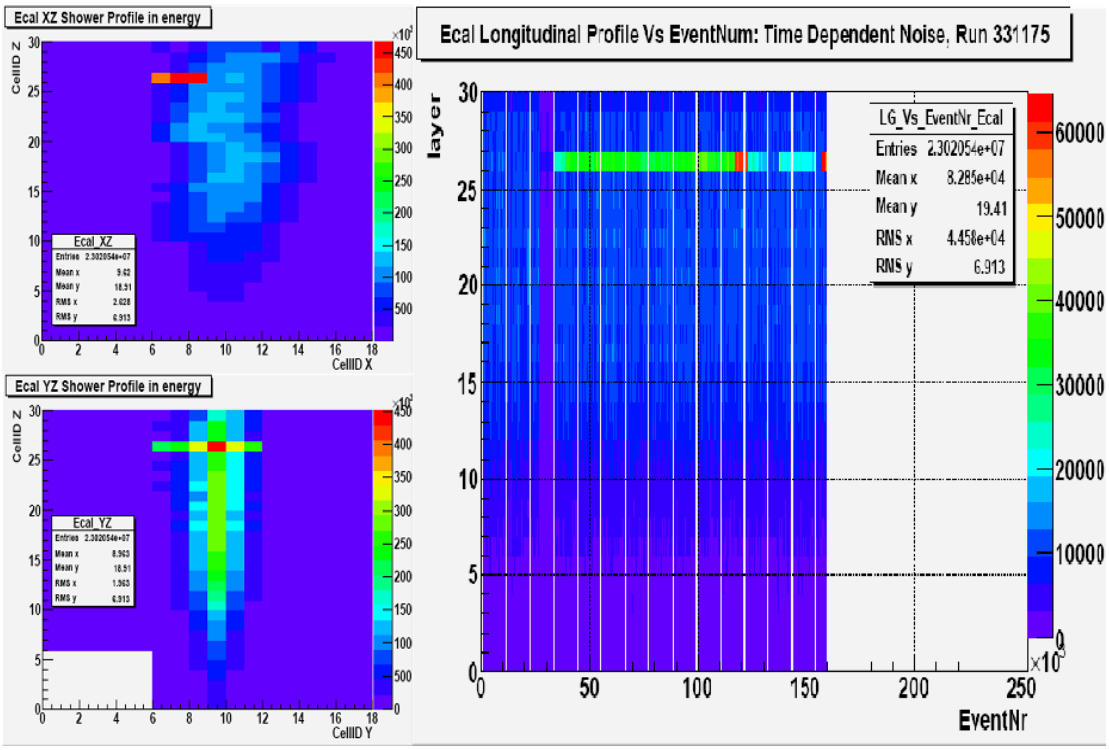

Figure 5.14 Time and chip dependent noise, Run331175

Figure 5.14 shows the shower profile projections on XZ, YZ plane (left plot), as well as the longitudinal shower profile versus the number of events (right plot) for Run331175. Run331175 is a 45GeV electron run with 20 degree injection angle, where the lower ECAL PCBs (each contains 3 wafers) have not yet been installed for

the first 6 layers. In the right plot, we find that there is a large noise on layer 26 after 30k events. This noise can be located to a VFE chip, which corresponds to 18 electronic channels (a matrix of 3 cells in the X direction and 6 cells in the Y direction, see the left plot of Figure 5.14). In some other run, even the whole PCB could be very noisy – this pattern is caused by large pedestal shift, which can be corrected for when the pedestal value will be updated. The same pattern is also observed in the HCAL for many runs.

As shown in Figure 5.15, the energy deposition on the last ECAL layer is much lower than expected. This is observed in almost all the electron-pi mixed runs and hadron runs. This is caused by large number of the dead channels on the last layer.

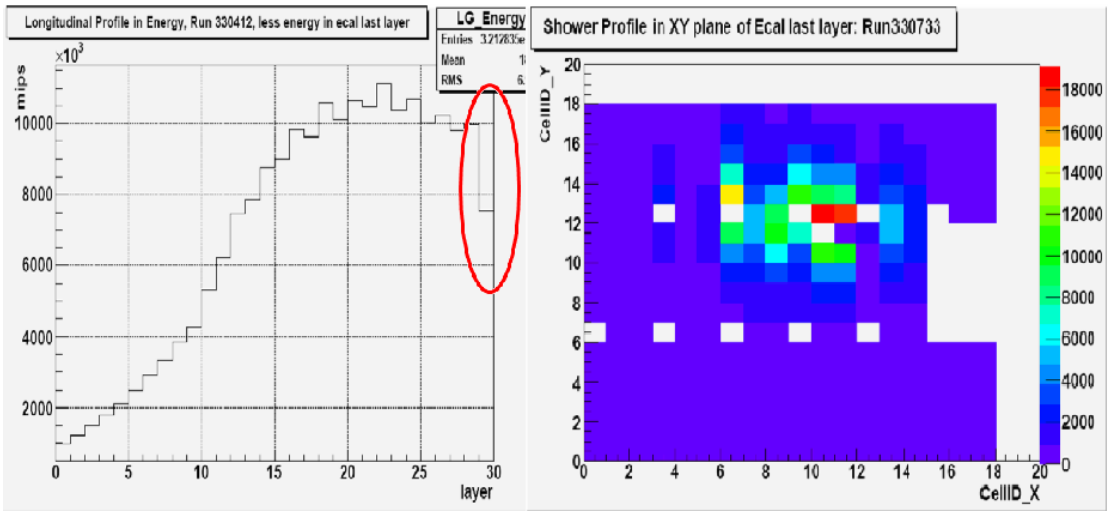

Figure 5.15 Many dead cells observed in the last ECAL layer，Run330733

Low energy noise in some layers is also observed in many runs, see Figure 5.16, this noise will largely increase the number of hits on the corresponding layer, while for the energy deposition there is no significant change. This is caused by the pedestal shift as well as the variation of the noise level, which could also be corrected in later reconstruction.

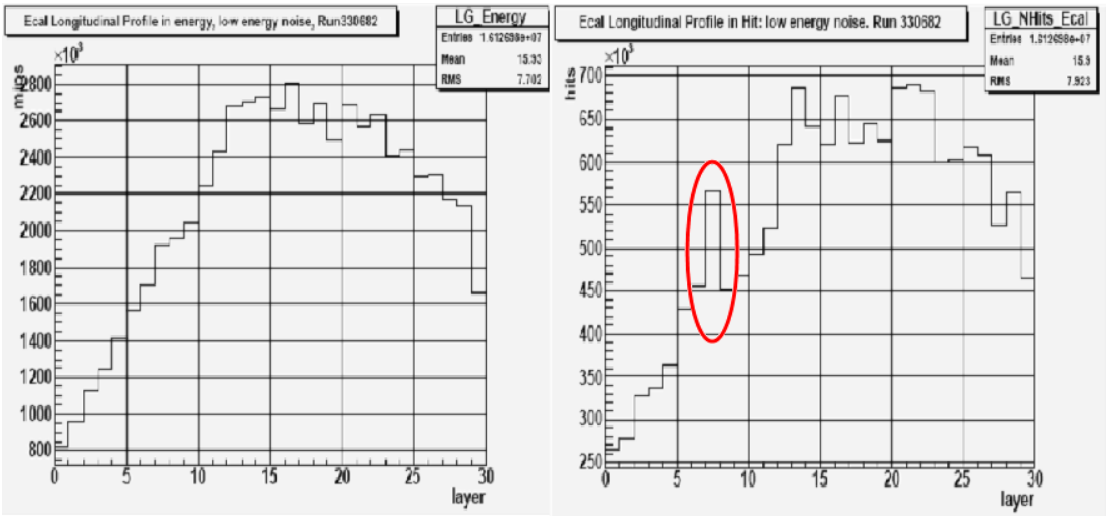

Figure 5.16 Layer dependent low energy noise

As we mentioned in the previous section, there is a systematic effect caused by the 2mm dead zone between wafers (as shown in Figure 5.17, there is a 1mm width guide ring at the edge of each wafer). When the charged particles pass through the dead zone, no energy deposition will be recorded. That caused the low energy bump on the total energy deposition spectrum. Take Run330195, a 45GeV nominal injection electron run as an example, the beam is injected at the center of the wafer in the X direction, and in the middle of 2 wafers (dead zone) in the Y direction. We could clearly see a low energy bump on the total energy spectrum (see Figure 5.18), and significant correlation between the total energy deposition and the mean position in Y direction (see Figure 5.19). If we select events far away from the dead zone (at least 3 mm from the wafer gap, red plot in Figure 5.18), this bump disappear.

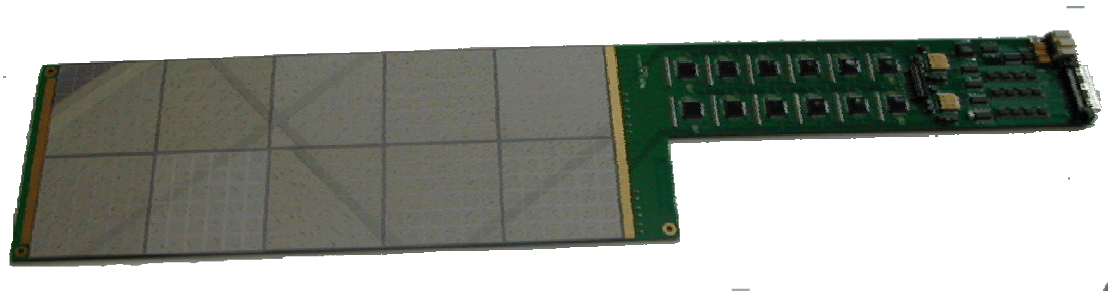

Figure 5.17 A sensor layer of ECAL (including the PCB and VFE chips), note the 2mm width of dead zone between wafers

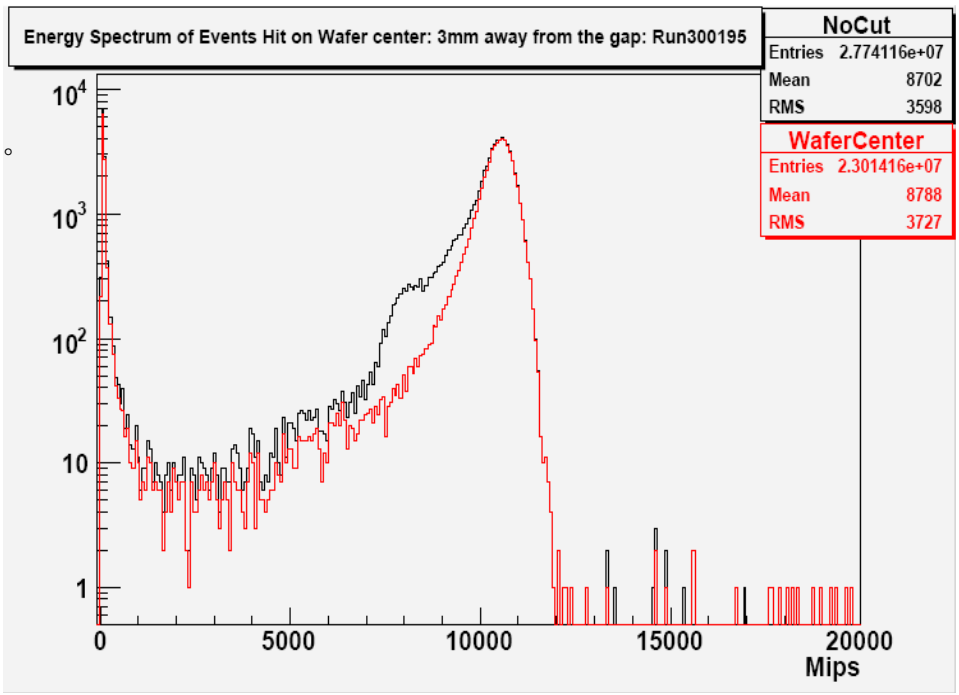

Figure 5.18 Low energy bump caused by the dead zone

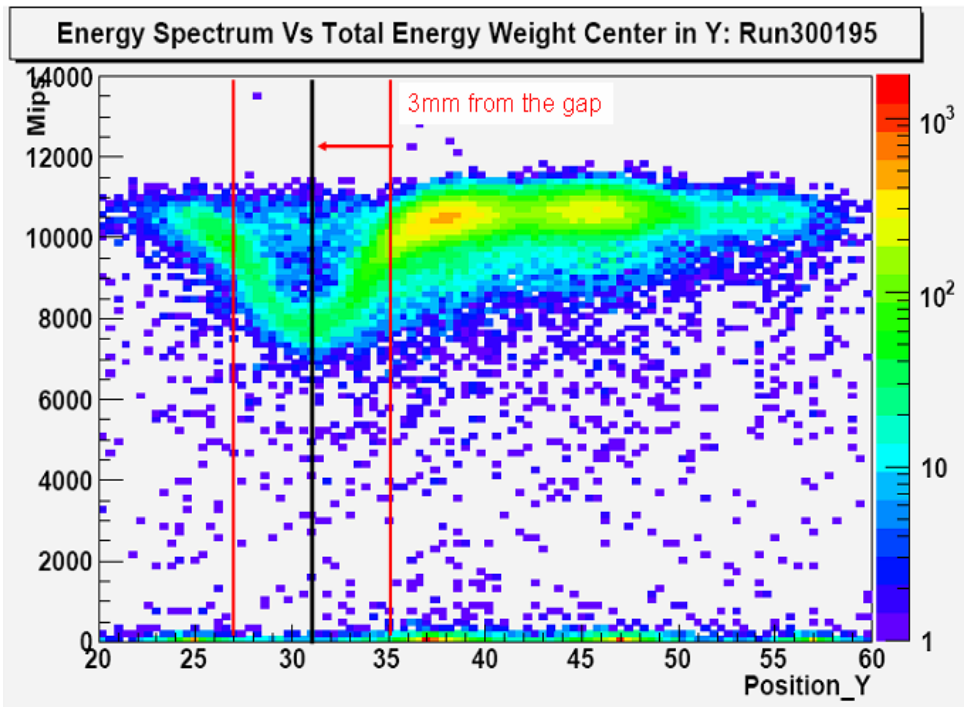

Figure 5.19 Correlation between the total energy deposition and the beam impact position

If the beam is injected at the edge of wafers, we can even observe the double-bump pattern on the low energy side of total energy deposition spectrum. Many different methods to correct this effect have been proposed, i.e. giving additional weight to the edged cells, or assuming there are virtual cells on the dead zone (while the energy is determined by the neighbor cells). Figure 5.20 shows the energy spectrum before/after the correction (LPSC, J-Y. Hostachy & L. Morin[68]).

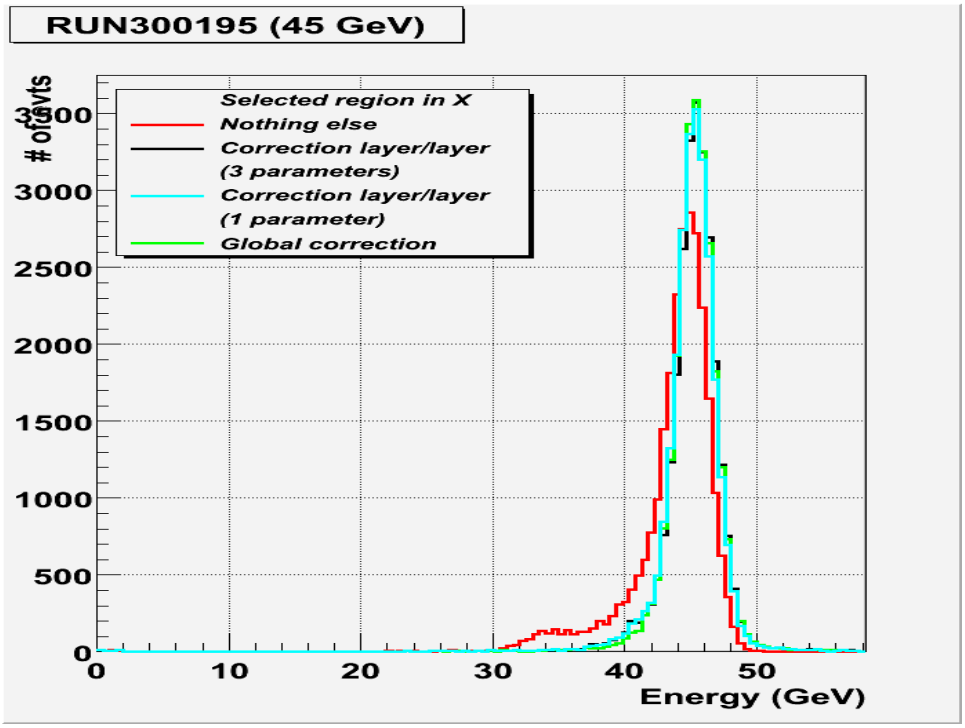

Figure 5.20 Total energy deposition spectrum correction[68]

The runs that we performed the data quality check are summarized, as shown in table 5.3. This classification is used for later offline data analysis, making convenient for our later analysis work.

None Beam Run	300090, 300106-107, 300209, 300211-212, 300214-219, 300226, 300228-233, 300244-246, 300248-256, 300258-259, 300261-263, 300267-268, 300279-290, 300292-299, 300301, 300309-310, 300324-326, 300335, 300342, 300344-346, 300351, 300355-359, 300362, 300367-369, 300372, 300603, 300617, 300621-623, 300625-627, 300636, 300639-642, 300655,
Garbage Run	300095, 300097, 300212, 300224, 300240, 300270, 300272, 300275, 300264, 300291, 300336, 300340 300370, 300596-597, 300615, 310057-058, 310061, 310067-70
Run with low statistics (Reconstruct Event Num <1500)	300093, 300094, 300098, 300100, 300204, 300273, 300323, 310049
Clean electron run	300084, 300087-89, 300091, 300096, 300205-206, 300236, 300366, 300373-375, 300383, 310046-48, 310052, 310054-056, 310060, 310063, 310064
Clean pion run	300086, 300193-194, 300234, 300312, 300314-315 300329-332, 300347, 300358, 300360-361, 300382, 300592, 300600,
Clean mixed run	300092, 300099, 300101-104, 300187-188, 300190-192, 300589, 300591, 300670-676,
Almost clean electron run	300197-198, 300201, 300203, 300220-221, 300257, 300260, 300269, 300318-322, 300327-328, 300333, 300353, 300377-379, 300633, 310053, 310062,
Run with noisy layer	300085, 300105, 300185-186, 300189, 300196, 300199, 300210, 300213, 300227, 300237, 300239, 300241-243,

	300265-266, 300276, 300277, 300338, 300354, 300363, 300371, 300380, 300381, 300590, 300593-595, 300598-599, 300601-602, 300604-610, 300612-614, 300618-620, 300628-631, 300634-635, 300637, 300643-652, 300654, 300656-659, 310050-051, 310059, 310065,
Electron run with bump pattern in total energy spectrum	300195, 300196, 300207-208, 300210, 300225, 300227, 300235, 300241-243, 300247, 300278, 300302-304, 300311, 300313, 300316-317, 300334, 300337-339, 300341, 300348-350, 300371, 300381, 300384, 300352, 300364-365
Electron run with large low energy tail	300200, 300202, 300222-223, 300237-239, 300271, 300274, 300276, 300300, 300305-308, 300334, 300354,
Run with less hit in first layer	300611, 300616, 300618-619, 300624, 300628, 300632, 300659, 300666-669

Table 5.3 Classification for test beam runs (CERN, August – October, 2006)

5.5 Summary

In this chapter, we introduced the CALICE test beam experiment. The CALICE collaboration is one of the biggest and most active collaborations on the ILC detector R&D, and its result will greatly affect the ILC project. The CALICE collaboration has successfully organized several test beam experiments, and the corresponding data analysis work is well under way with highly efficiency organization and management.

In the next chapter, we will focus on the data analysis of the ECAL signal of the CALICE test beam experiment.

Chapter 6 CALICE test beam data analysis, ECAL part

6.1 Introduction: interactions between particles and materials

Showers are created when beam particles inject into the calorimeter. The electromagnetic shower create huge number of charged particles (mainly in the absorber), and when those particles passing through the sensor layer, the materials are ionized and create free charges. Driven by the electric field the ionized electrons shift to the edge of sensor layer, and are collected by the capacitance there. The quantity of the charge, which is proportional to the number of charged particles passing through the sensor, is converted to the voltages and then ADC values in the electronic. The energy deposition in each calorimeter cell is assumed to be proportional to the quanta of charge, so by pedestal subtraction, calibration and ADC value counting of each channel, we are able to calculate how much energy is deposited in each cell.

For the calorimeter, an inject particle means a set of hits with their positions and energy depositions information. The total energy deposition, the beam inject position and inject angle could be calculated with those information. In this chapter, we will discuss the energy, position and angle resolution algorithm and accuracy for the ECAL in the CALICE test beam experiment. To get a better understanding to the physical picture, we will first discuss the interactions between different beam particles and the calorimeters.

The electron density is very high in materials, thus the electromagnetic interaction of electron, positron and photon to the material is very strong. For different materials, the conception of radiation length X_0 is introduced to describe the strength of their interaction with electron/positron/photon. The energy flow density will be reduced by a factor of e when electron beam passing through one X_0 of material. X_0 is approximately 7/9 of the electron

mean free path length. The short the X_0 is, the stronger the interaction with electron beam is. For example, the X_0 of lead is 0.9cm, while tungsten, the absorber material in the CALICE ECAL prototype, has an X_0 of 0.35cm, only about 1/3 of that of lead. In CALICE ECAL prototype, to ensure an inject electron (positron, photon) could deposit all its energy in the ECAL, the ECAL prototype have totally 24 radiation length in the longitudinal direction (8.4cm thick tungsten), divided into 30 layers. Small X_0 allows a compact ECAL and ensures good separation between energies deposited from different sources. (Since the Moliere radius (see section 6.3.2) is proportional to X_0.)

The CALICE ECAL prototype is segmented in 1cm×1cm cells in the transverse plane (see chapter 5.2), and Figure 6.1 shows the spectrum of energy deposition in each cell for the ECAL prototype. We find that besides the Minimal Ionization Particle (MIP) peak, the energy deposition in each cell covers a wide range, from several mips to hundreds of mips. The MC result agrees nicely with the real data (The disagreement between MC and real data at low energy region is caused by the electric Noise, which could be regarded as a Gaussian with 0.12 mip width).

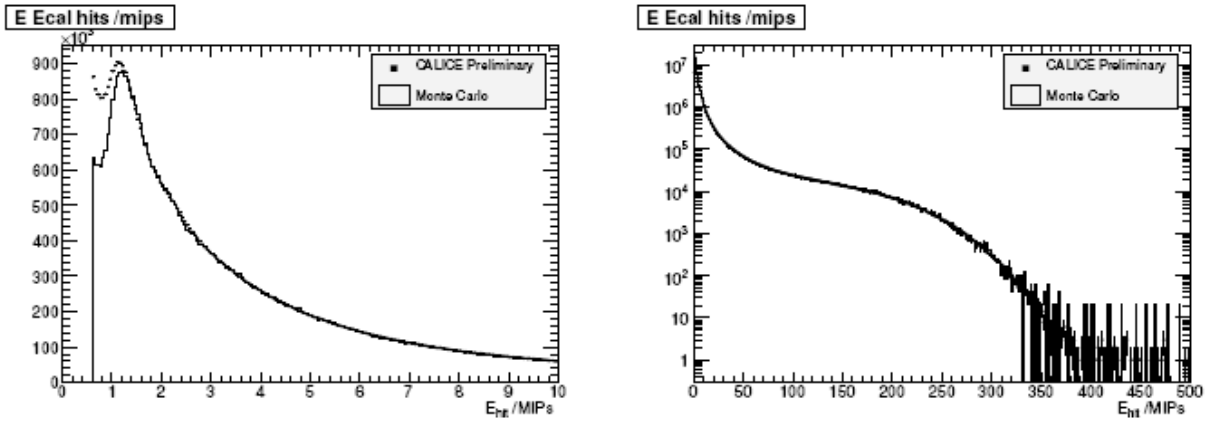

Figure 6.1 Energy deposition per cell for a 30GeV electron beam [57]. Left, zoom at low energy part; right, full scale of energy per hit with log scale.

The strength of interaction between long life time hadrons (π, K_L, proton, in the CALICE test beam experiment we collected many π events and some of

proton events) with the ECAL is much weaker than that of electron. Actually for the π beam, a lot of π interact with the ECAL as minimal ionization particles, see Figure 6.2. Like the conception of radiation length, the conception of interaction length λ_{HAD} is introduced to describe the strength of interaction between hadrons and material. For the most frequently used absorber in the HCAL, iron, has a λ_{HAD} of about 17cm, which is much larger than its radiation length (1.75cm). This refers to the fact that the penetration ability of hadron is much higher than the electron.

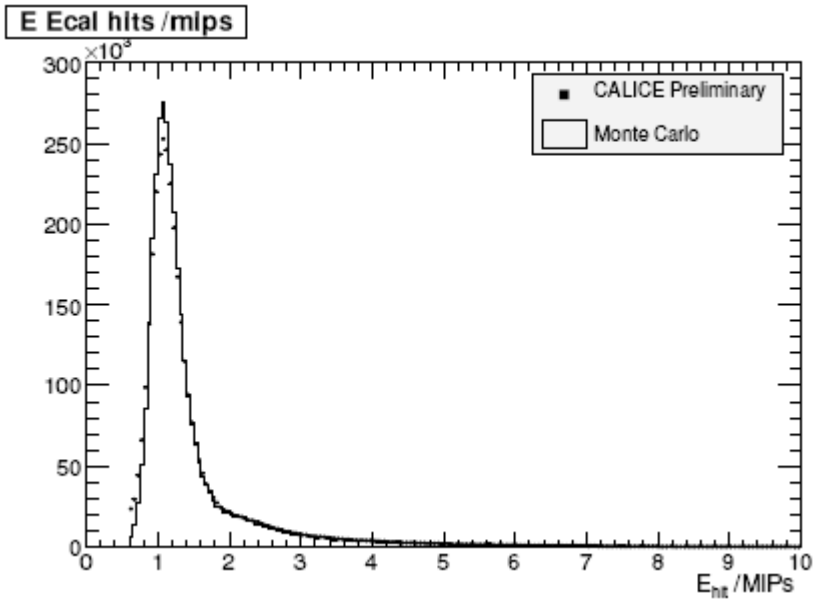

Figure 6.2 Energy depositions per cell for 12GeV π [57]

The μ particle is seen as the minimal ionization particle for the calorimetry system: the interaction between μ particle and materials is very weak (for most of the time it is the weakest of all the charged particles). The energy deposition per cell of μ passing by the material could be regarded as a Landau distribution convolute with a Gaussian distribution (from Noise), which peaks at a value defined as "1 mip". This property of μ makes people to use it for calibration, see chapter 5.4. Besides the test beam experiments, the CALICE collaboration also collect μ events from cosmic ray experiments.

6.2 Energy response and resolution for the ECAL Prototype

For the ECAL energy response, besides the energy deposition per cell, the total energy deposition of one event is also very important. The total energy deposition could be regarded as a weighted sum of energy deposition on each cell.

Figure 6.3 shows the total energy spectrum of an electron run and a π run. In the left plot we found almost all the energy of electron is deposited in the ECAL, create a Gaussian peak; while the energy deposition of π in ECAL is quite uncertain, and the total energy deposition is almost a flat distribution. In both plots we find a mip peak caused by the μ components in the beam.

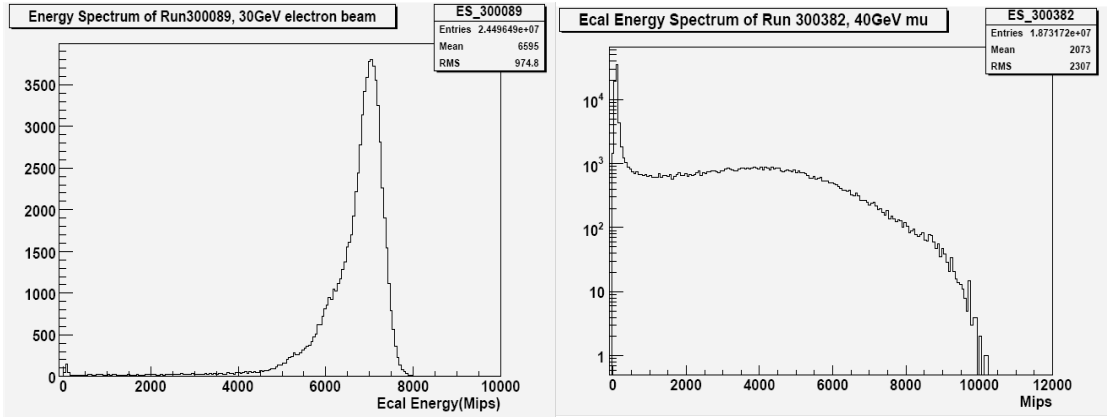

Figure 6.3 Total energy deposition in ECAL for a 30GeV electron run (left) and a 40GeV π run (right)

Some runs have mixed components (π, μ and electron). Figure 6.4 shows the total energy deposition (left) and total energy Vs total hit number (right) for a 60GeV mixed run (Run300092). In the two-dimensional plot (right), we could see clearly the separation of different beam components.

For the CALICE ECAL prototype, the thickness of each absorber layer is not identical (1.4mm, 2.8mm and 4.2mm for the first, second and last 10 layers respectively). The total energy deposition is a weighted sum for the energy of each hit: $E_{tot} = (\alpha_1 E_1+\alpha_2 E_2+\alpha_3 E_3)/\beta$. Here $E_1/E_2/E_3$ is the sum of energy deposited in the first/second/third 10 layers. As for the weight factor, a

direct choice is (α_1, α_2, α_3) = (1, 2, 3), (proportional to the absorber thickness), while further study shows when (α_1, α_2, α_3) = (1.1, 2, 2.7) we could achieve better performance in the linearity of energy measurement, see Figure 6.5. For electron runs, with a fit to the Gaussian peak in the total energy spectrum we could get the corresponding mean value and accuracy of energy resolution. As shown in Figure 6.6, the CALICE ECAL prototype has good energy linearity and resolution.

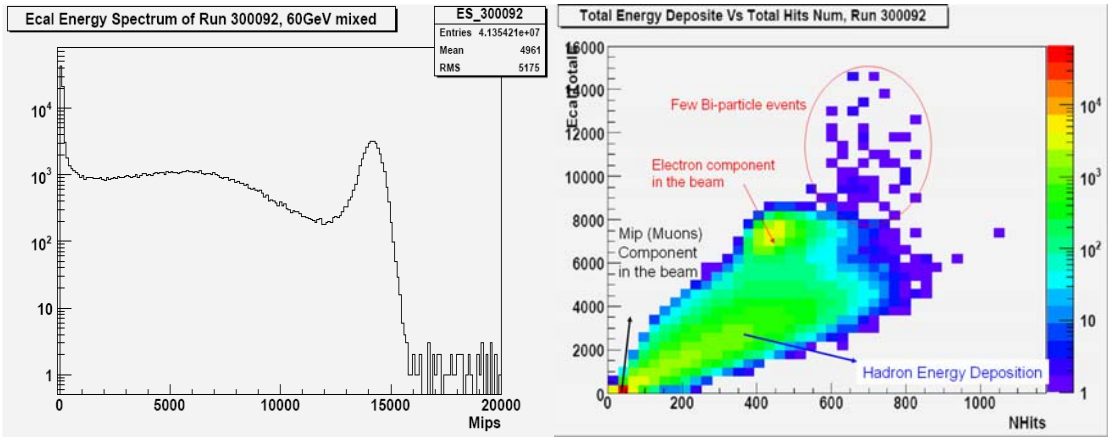

Figure 6.4 Total energy deposition (left) and total energy Vs total hit number (right) for a mixed run

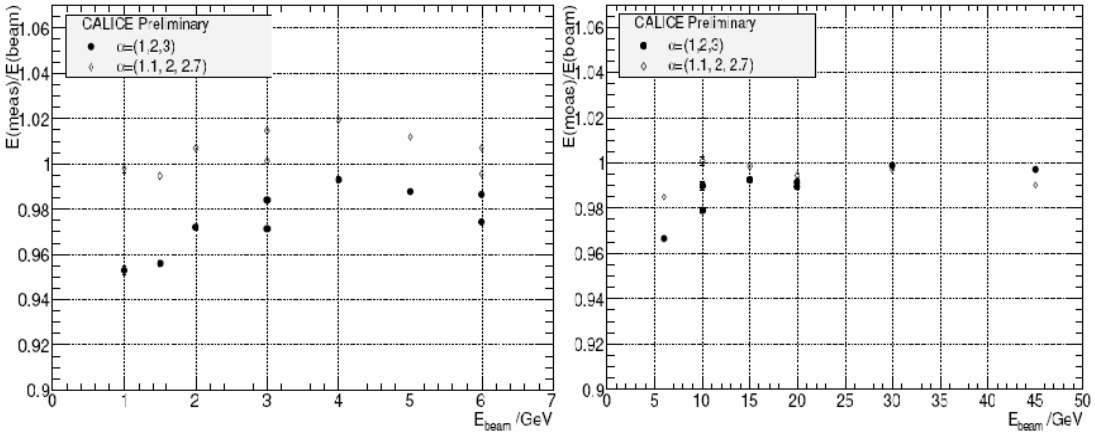

Figure 6.5 Linearity of ECAL energy response with different weight;
Left, DESY Runs (1－6GeV); right, CERN Runs (6－45GeV) [57]

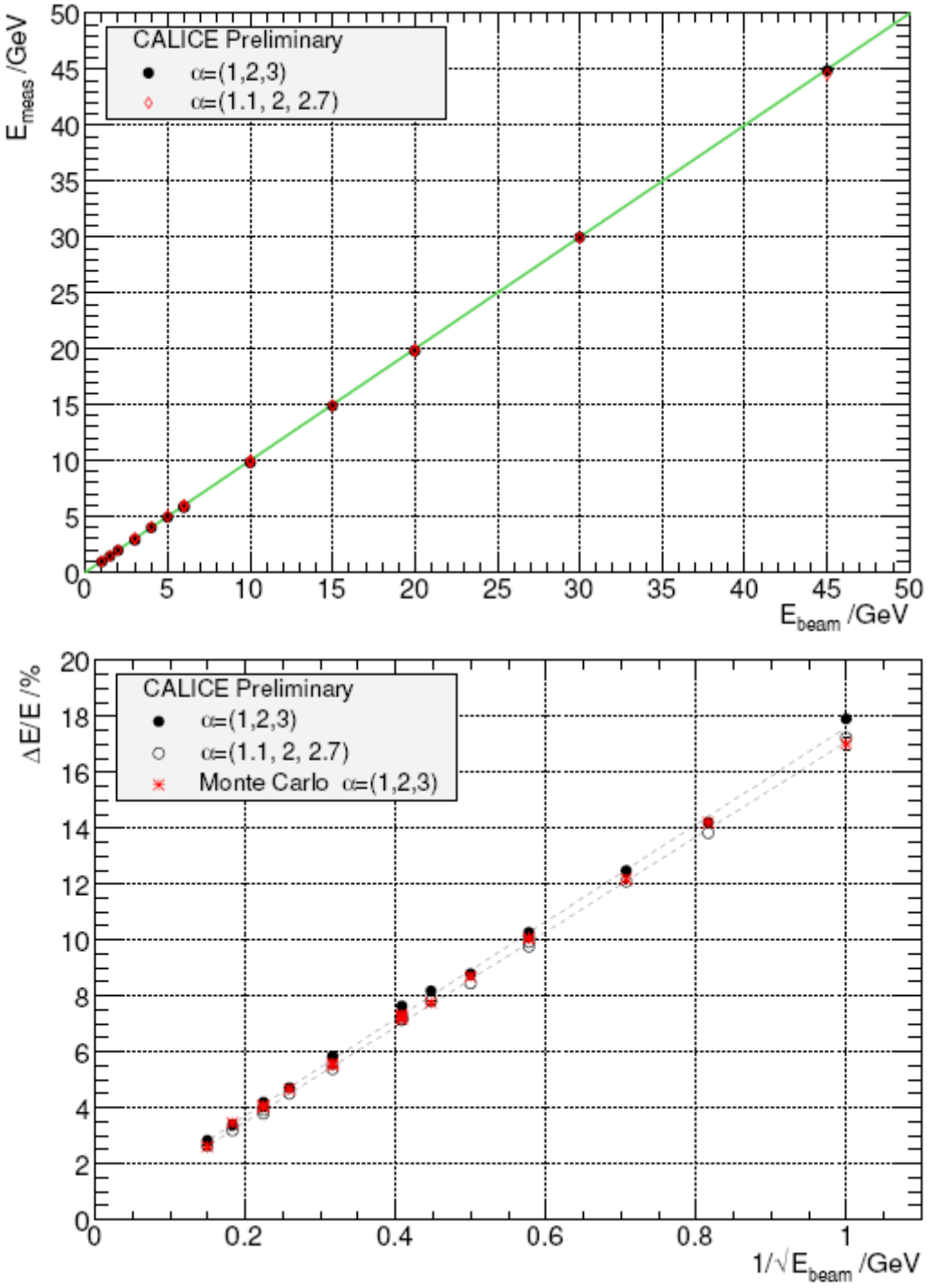

Figure 6.6 Energy linearity and resolution of CALICE ECAL Prototype [57]

With a fit, we could get the following relation between energy resolution accuracy and beam energy:

Taken (α_1, α_2, α_3) = (1, 2, 3), we have:

$$\Delta E/E = \left(17.13 \pm 0.07/\sqrt{E(\mathrm{GeV})} \oplus 0.54 \pm 0.15\right)\%$$

While for (α_1, α_2, α_3) = (1.1, 2, 2.7), we have:

$$\Delta E/E = \left(17.67 \pm 0.07/\sqrt{E(\mathrm{GeV})} \oplus 1.07 \pm 0.08\right)\%$$

When the beam inject with an angle, the accuracy of total energy deposition will slightly changed, see Figure 6.7.

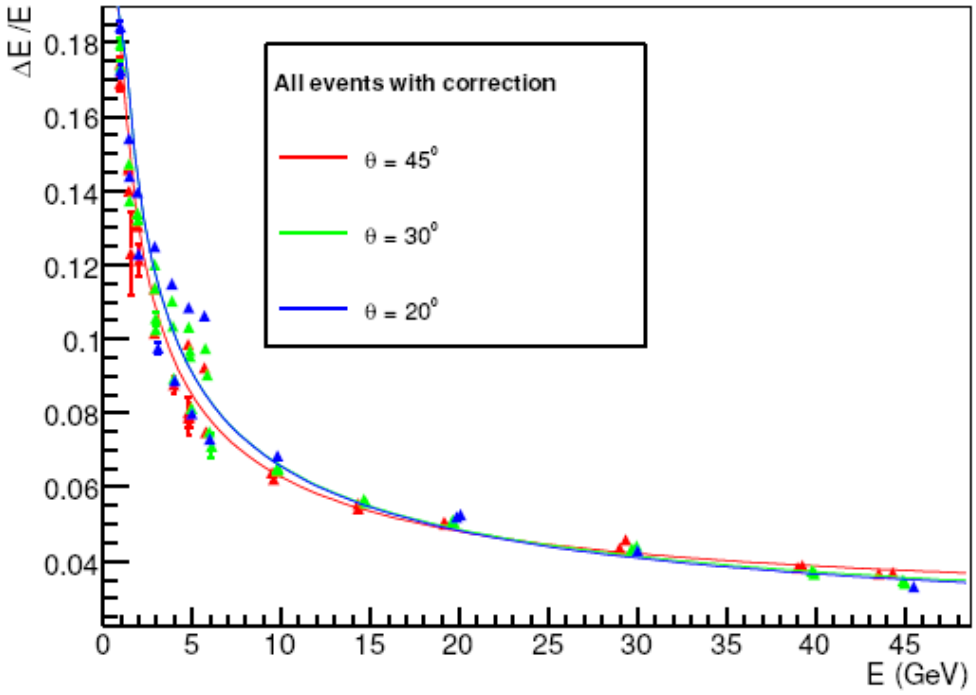

Figure 6.7 Energy resolution varies with beam energy and inject angle [57]

Generally speaking, the performance of the CALICE ECAL prototype on energy measurement is very good and agrees with people's expectation, it also agrees nicely with the MC result. In the next section we will switch to its spatial resolution.

6.3 The shower profiles and the spatial resolution

The shower profile means the spatial distribution of a shower. Figure 6.8 shows the projection of shower profile on XY (left) plane and XZ (right) plane for a 50GeV electron run. The shower spread wider in X direction than in Y direction, that's caused by the asymmetry in the beam collimator system. The projection of shower profile on Z direction (XY plane) is called the longitudinal (transverse) shower profile.

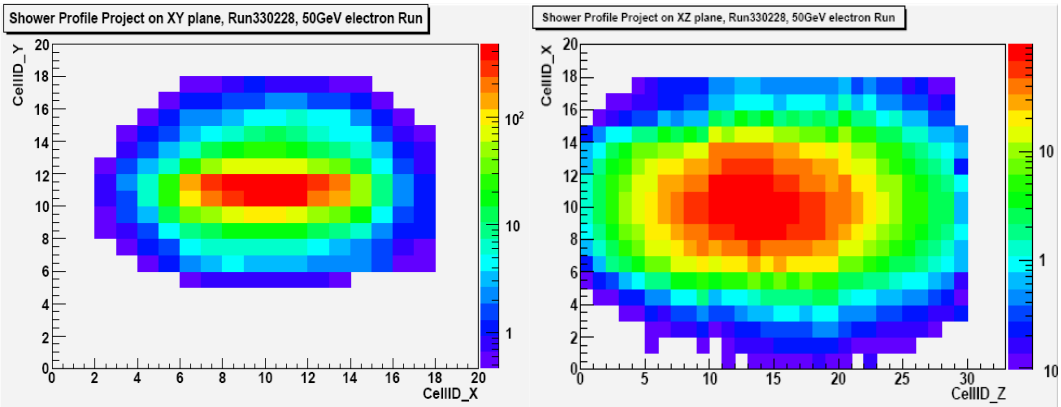

Figure 6.8 Shower profile projection on XY plane and XZ plane for a 50GeV electron run (Run330228)

6.3.1 The longitudinal shower profile

The longitudinal shower profiles for electron runs with different beam energy are shown in Figure 6.9 (here beam inject normally). The histogram is the result from MC, while the points with error bar are the real data result. The curve is a fit with function $\gamma(t)=c*t^{a}*\exp(-\beta t)$, here t refer to the calorimeter depth, and c is the overall normalization factor.

When we increase the beam energy, the energy deposited on each layer increases and the shower maximal moves to deeper layers. The left plot of Figure 6.10 shows the relationship between shower maximal and the beam energy, we find that these two quanta are nicely correlated with a logarithm relationship. That's not surprising for the energy flux decays exponentially

with the material depth. The right plot of Figure 6.10 shows the shower maximal with different inject angle (beam energies are all equal to 30GeV). And the position of shower maximal satisfy L(0)=L(θ)/cos(θ), means the true depth of shower maximal is the same for different inject angles.

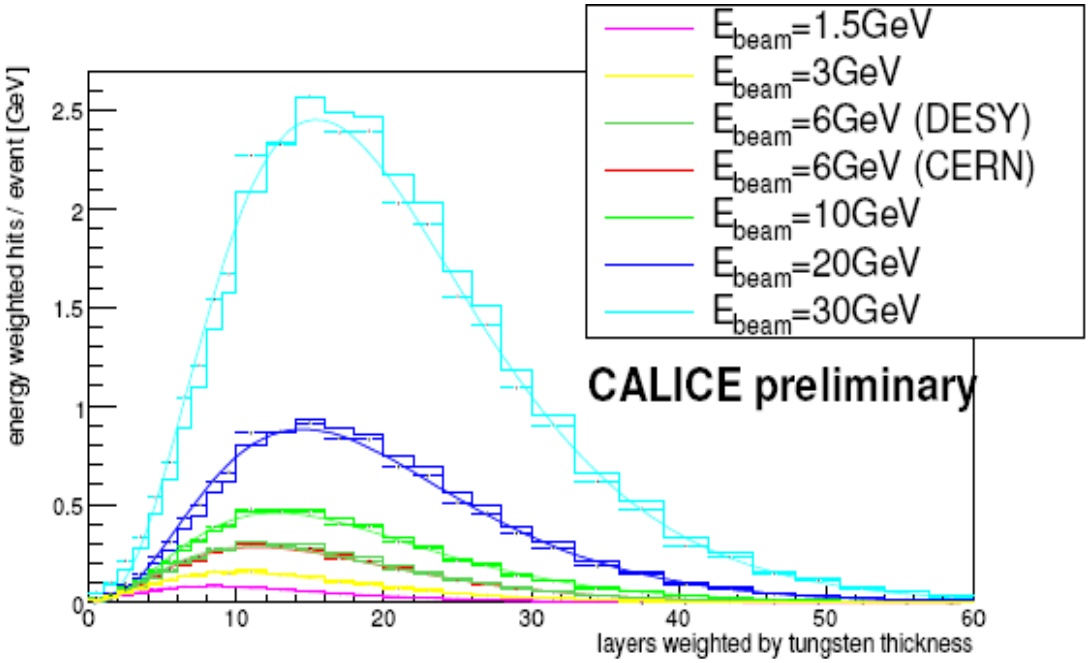

Figure 6.9 Shower longitudinal profiles for beam with different energy [57]

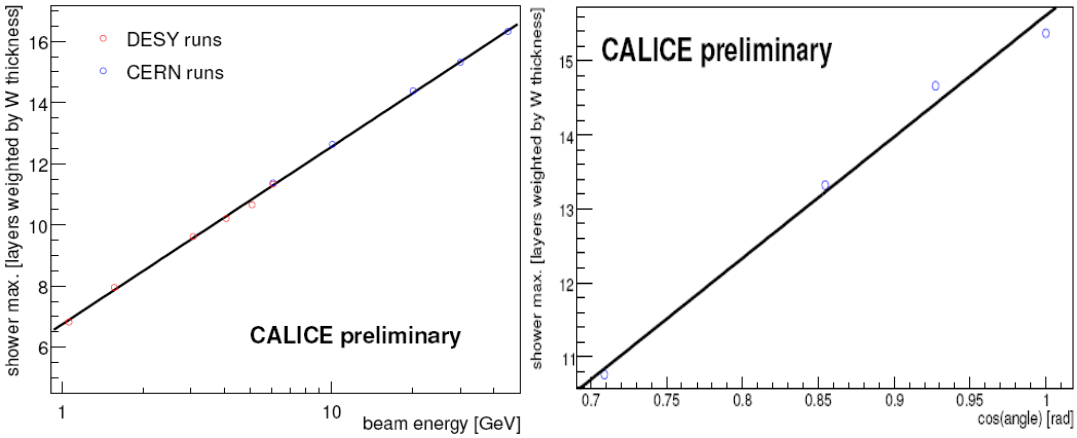

Figure 6.10 left, shower maximal position Vs beam energy (normal inject run); right, shower maximal position Vs inject angle (30GeV beam energy) [57]

The above discussing shows that the longitudinal shower profile agrees with our expectation, and the MC simulation gives comparable result with real data. Now let's turn to the transverse shower profile.

6.3.2 The transverse shower profile

Alike the conception of radiation length, people introduce Moliere radius with dimension of length to describe the shower development in the transverse plane. The physical meaning of Moliere radius is following: on the projection of shower profile in XY plane, if we draw a circle with radius equal to the Molilere radius, then 90% of the shower energy will distribute within the circle. Moliere radius is proportional to the radiation length, approximately we have:

$$R_M=0.038\times(Z+1.2)\times X_0.$$

Here Z refers to the atomic number of the material. Smaller Moliere radius means the shower is much more concentrated on the XY plane, and better separation of showers from different injected particles, which is of extremely importance for the PFA algorithm. The Moliere radius for tungsten, the absorber material we used in the CALICE ECAL prototype, is about 10mm.

Figure 6.11 shows the energy distribution on XY plane for a 3GeV electron Run in the test beam experiment. Take the beam line as axis and making a column with different radius, Figure 6.11 shows the relationship between the radius of the column and the corresponding energy coverage (percentage of total energy contains inside the column). We find that for the ECAL prototype, when energy coverage reaches 90%, the column radius is about 20mm. That's mainly caused by the sandwich structure of our prototype (In the longitudinal direction, the total thickness of tungsten is 84mm, about 42% of the ECAL prototype thickness).

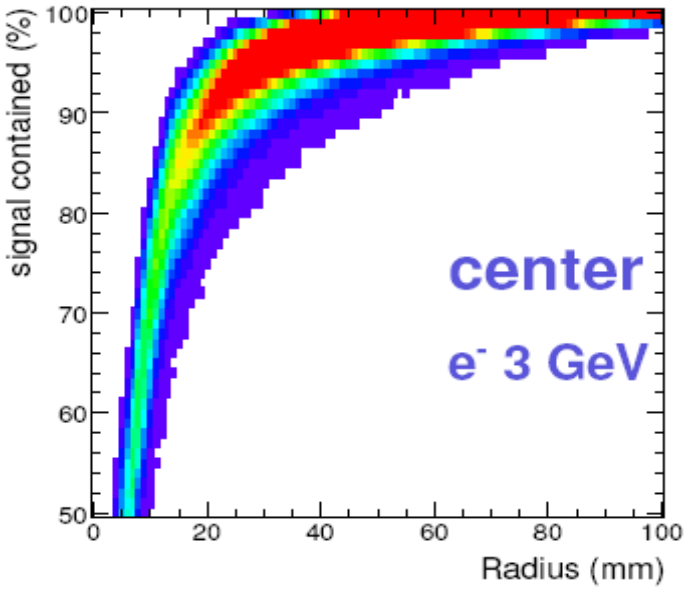

Figure 6.11 Column radius Vs energy coverage for 3GeV electron Run [57]

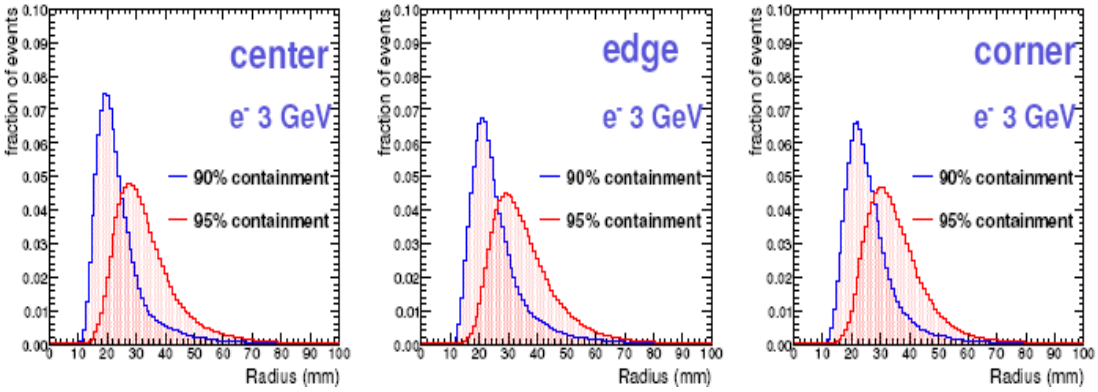

Figure 6.12 Distribution of Column radius with 90%/95% energy coverage [57]

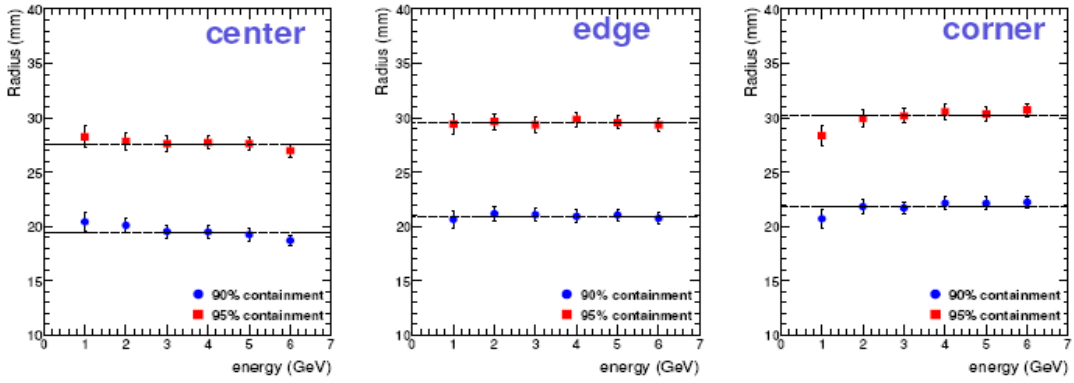

Figure 6.13 Peak position of Column radius with 90%/95% energy coverage [57]

Figure 6.12 shows the column radius distribution with 90% and 95% energy coverage. These distributions are slightly different for beam aim at wafer center, edge or corner for the 2mm dead region between wafers. For a given energy coverage, larger column radius is required from the center to the edge and then to the corner. While for the runs with different energy, the peak position for the column radius with 90% and 95% energy coverage doesn't have significant difference (see Figure 6.13).

From the above discussing the distribution of transverse shower profile also meets our expectation. Besides, the 2mm dead region between wafers caused significant systematic effect here, and need to be corrected. From the news of electronics, many efforts are made to reduce the size of dead region between different wafers.

6.3.3 The spatial resolution of the CALICE ECAL prototype

The inject position on the XY plane of the particle could be regarded as the shower energy weighted center (for normal inject run), we have:

$$(X,Y) = (\sum x_i E_i / \sum E_i , \sum y_i E_i / \sum E_i) .$$

To measure the ECAL spatial resolution we need a reference point. In the test beam experiment, by using the track information reconstructed by the tracking system (include 3 or 4 pairs of Drift Chambers in front of the ECAL) we can predict the particle inject position on the ECAL, see Table 6.1.

By subtract the ECAL measured position and reference position we get Figure 6.14, a Gaussian distribution on both X (left) and Y (right) directions (the derivation of mean values from 0 for both distributions are caused by the misalignment between subdetectors). With a fit we can get the width of the Gaussian, which is defined as the spatial resolution of the ECAL. For a normal inject run, the spatial resolution is better in X direction than in Y direction, that's caused by the geometry effect: in the X direction there are

shifts between different layers, while for the Y direction, all the layers are aligned to the same position.

	x		y	
Beam Energy (GeV)	Position (mm)	Angle (mrad)	Position (mm)	Angle (mrad)
1.0	1.68 ± 0.22	2.48 ± 0.27	1.57 ± 0.22	2.41 ± 0.27
2.0	1.00 ± 0.12	1.34 ± 0.13	0.98 ± 0.12	1.30 ± 0.13
3.0	0.81 ± 0.09	0.92 ± 0.09	0.79 ± 0.09	0.90 ± 0.09
4.0	0.72 ± 0.07	0.73 ± 0.07	0.69 ± 0.07	0.72 ± 0.07
5.0	0.66 ± 0.06	0.62 ± 0.06	0.65 ± 0.06	0.61 ± 0.06
6.0	0.60 ± 0.06	0.53 ± 0.05	0.59 ± 0.06	0.52 ± 0.05

Table 6.1 Track position and angle reconstructed from the Tracking system （Run230097-230104）[57]

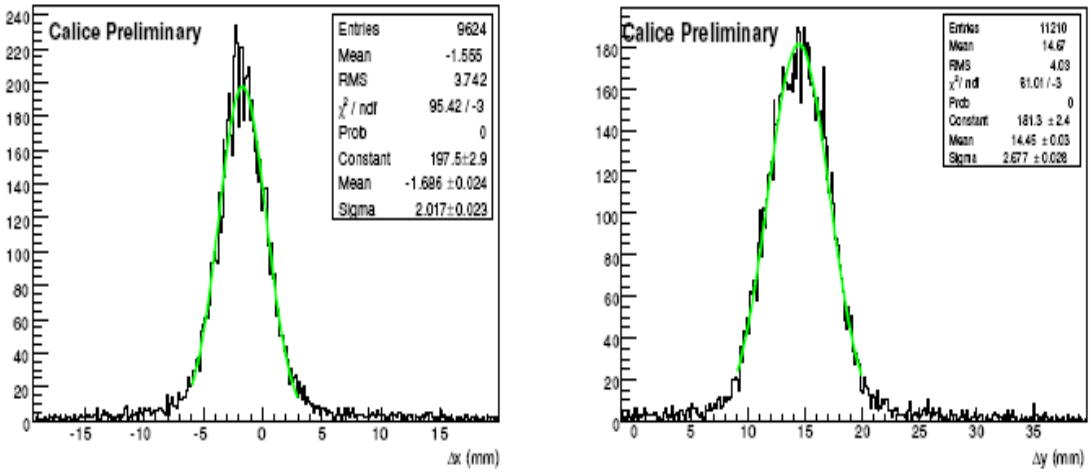

Figure 6.14 The difference between the ECAL measured position and the Drift Chamber predicted position（Run230097，6GeV Run）[57]

It’s not surprising that the ECAL spatial resolution accuracy depends on the beam energy, see Figure 6.15, also the MC results are shown there. As well as the energy resolution, we achieve better spatial resolution for larger beam energy. And the resolution difference between X direction and Y direction is a systematic effect doesn’t depending on the beam energy. The result from MC basically agrees with our real data result.

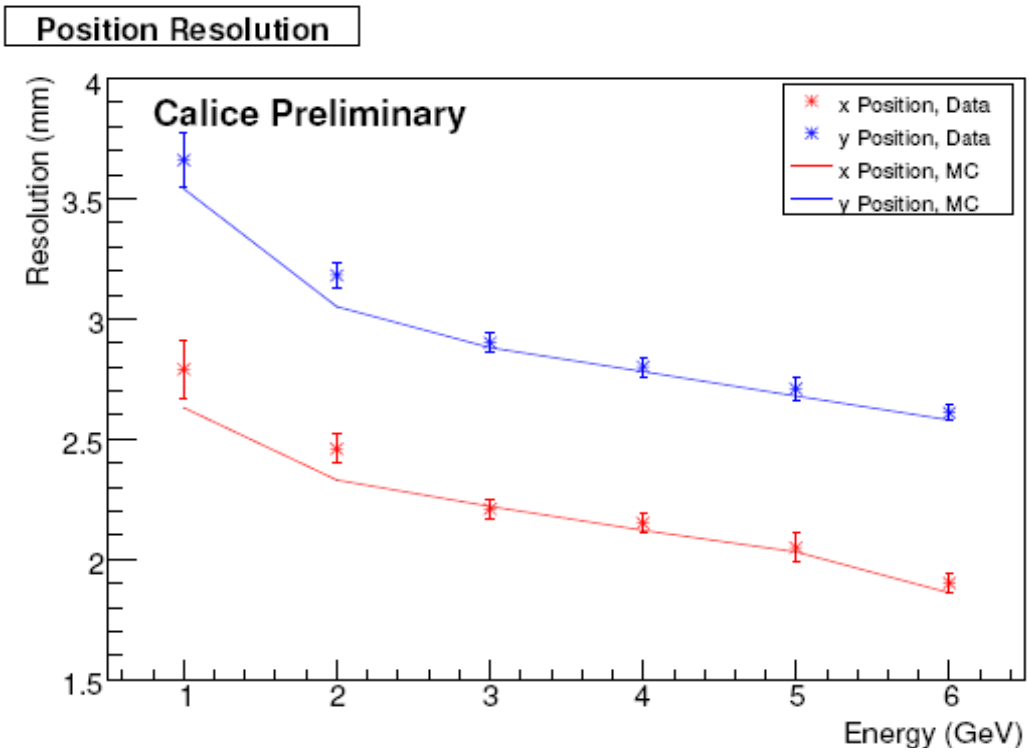

Figure 6.15 The ECAL spatial resolutions for different beam energy [57]

6.4 The angular resolution for the CALICE ECAL prototype

6.4.1 Introduction and motivation

As well as the energy resolution and spatial resolution, the angular resolution accuracy is a characteristic parameter of the calorimetry system, especially for the ECAL. Since the neutral particles have no track in the TPC, the 4-momentum of a neutral particle (mainly gamma and hadrons) is measured by the calorimetry system. Because the photon components always takes over 20% of the total energy in a jets (while the neutral hadron components takes only 5% of total jet energy), the 4-momentum measurement of photon through ECAL is of extremely importance for us to achieve good jet energy resolution.

Besides, if the ECAL have good spatial resolution, we could use it to identify a photon generated beyond the interaction point, which is possible in

some SUSY models (image a long life time NLSP decays into LSP and a photon). Also, we could gain better track momentum resolution if we could identify the FSR photon from a track (and match the FSR photon to the track), see Figure 6.16.

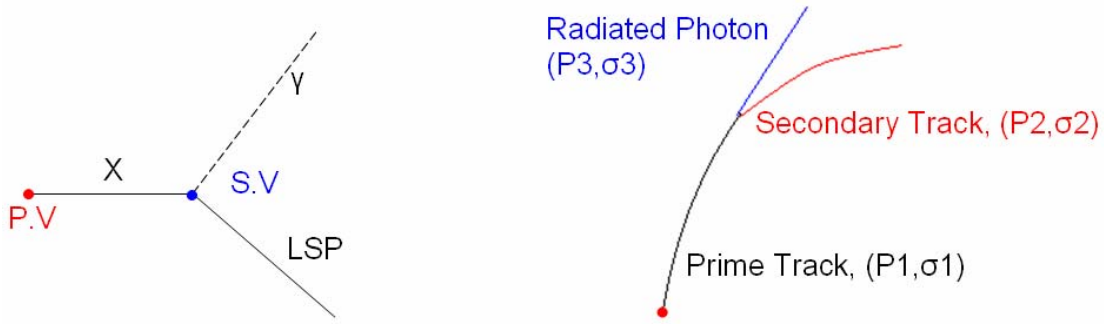

Figure 6.16 Possible physical application of the ECAL angle measurement: detect photon generate beyond the interaction point (In the left plot the P.V refer to the Prime Vertex, and S.V means the Secondary Vertex)

We develop an angular resolution algorithm based on the ECAL information only (or called the track-free method). Since the photon interact with the ECAL in the same way as electrons and positrons, we test our algorithm on a set of electron runs, and making a comparison between our result and previous result which use the drift chamber information to reconstruct a reference line. The result looks encouraging.

Table 6.2 shows the data we used: totally 24 electron runs, including 6 normal inject DESY runs with 1GeV to 6GeV beam energy and 18 CERN runs with beam energy from 15GeV to 50GeV. For the CERN runs we have three sets of inject angles (normal inject, or inject with 10 degree, 20 degree angle), each contain six runs. In the DESY runs the ECAL has only been equipped with 24 sensor layers (layer 0-21, 24, 25), and each layer has only a PCB with 2×3 wafers (2 wafers in Y direction). For the CERN runs we have almost fully equipped ECAL (for the first 6 layers we have only installed the 6-wafer PCB).

In order to get rid of noise (including the μ components in the beam, and the double events, etc), a straight forward event selection based on the sum of

energy deposition on each layer is applied. The event selection information is summarized in column 4 of Table 6.2. Now let's begin our discussing on the algorithm.

RunNum	Beam energy	Inject angle	Cut on sumE /mips	RunNum	Beam energy	Inject angle	Cut on sumE /mips
230098	1GeV	0°	90-230	330996	15GeV	10°	1.5k-2.5k
230099	2GeV		150-450	330995	20GeV		1.5k-3.5k
230097	3GeV		300-600	330994	25GeV		2.5k-4.5k
230100	4GeV		400-800	330993	30GeV		3.0k-4.5k
230104	5GeV		500-1.0k	330990	40GeV		3.0k-6.0k
230101	6GeV		600-1.2k	330986	50GeV		5.0k-8.0k
330433	15GeV		1.5k-2.5k	331194	15GeV	20°	1.5k-2.5k
330423	20GeV		1.5k-3.5k	331198	20GeV		1.5k-3.5k
330431	25GeV		2.5k-4.5k	331202	25GeV		2.5k-4.5k
330456	30GeV		3.0k-4.5k	331204	30GeV		3.0k-4.5k
330224	40GeV		3.0k-6.0k	331207	40GeV		3.0k-6.0k
330228	50GeV		5.0k-8.0k	331209	50GeV		5.0k-8.0k

Table 6.2 Test beam data files used in the angular resolution algorithm test

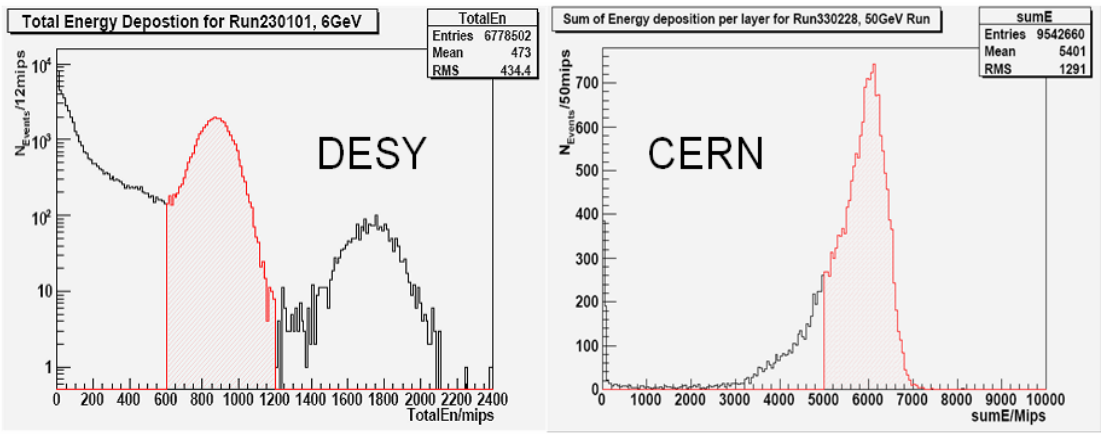

Figure 6.17 Event selection based on the sum of energy deposition per layer

6.4.2 Angular resolution algorithm for the CALICE ECAL Prototype

We assume that in the absence of external magnetic field, the longitudinal shower development of an electron/photon in the ECAL continues in the direction of the beam. This direction should coincide with the shower axis and the latter can be determined from a straight line fit to the shower. The X and Y directions are treated separately assuming there is no correlation between them. Here is the algorithm (take the X direction for example):

First, hit selection for each event: a hit is taken into account when it has energy deposition larger than 0.6mip.

Second, get a reference line with χ^2 fit to the energy weighted center per layer, $((X_i, Y_i) = (\sum_j x_{ij} E_{ij} / \sum_j E_{ij}, \sum_j y_{ij} E_{ij} / \sum_j E_{ij})$, here index i denotes the layer number and index j marks the hit number of the corresponding layer). The χ^2 is defined as following:

$$\chi^2 = \sum_{i=1}^{n} (X_i - aZ_i - b)^2 E_i$$

Total energy deposited in each layer is used as an additional weight in the χ^2. With the reference line, we are able to calculate the distance between the intersection point (of the reference line and the layer plane) and energy weighted center for each layer. The distribution of this distance is always a Gaussian, while its width could be defined as the spatial resolution of this layer, marked with σ_i, see Figure 6.18.

Third, taken into account the spatial resolution per layer, and fit the energy weighted centers into a straight line again. We have:

$$\chi^2 = \sum_{i=1}^{30} \frac{(x_i - az_i - b)^2}{\sigma_i^2} E_i$$

The direction of the fitted line is defined as the direction of inject beam. Thus the beam angle is measured.

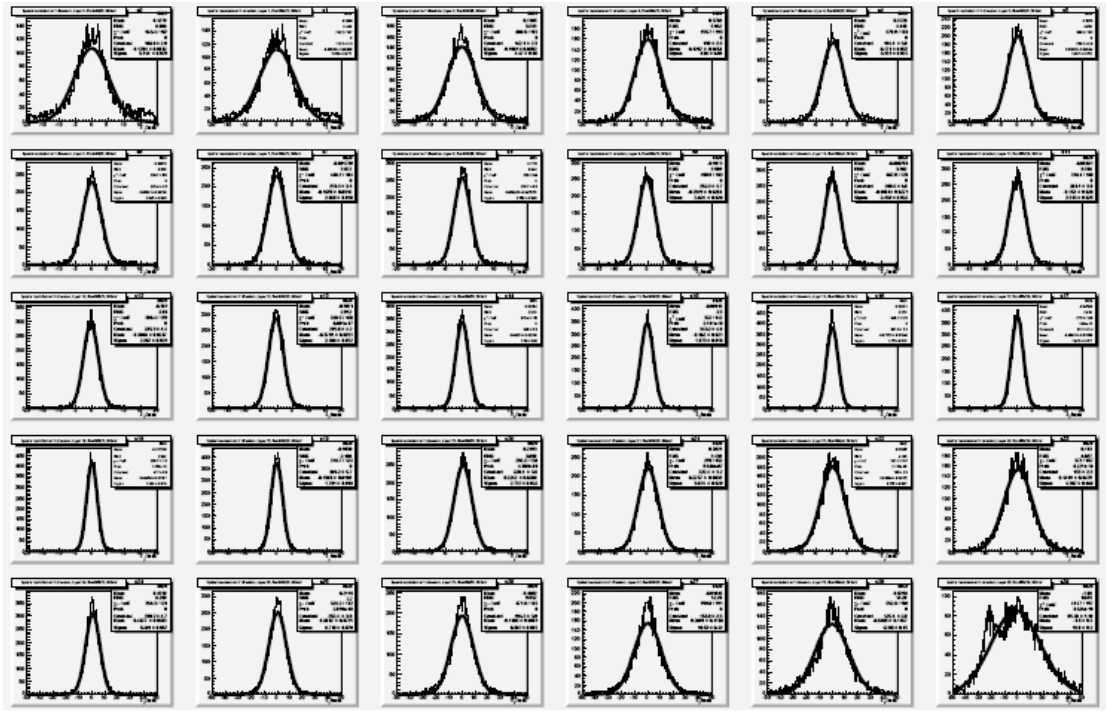

Figure 6.18 ECAL spatial resolutions per layer，50GeV electron run

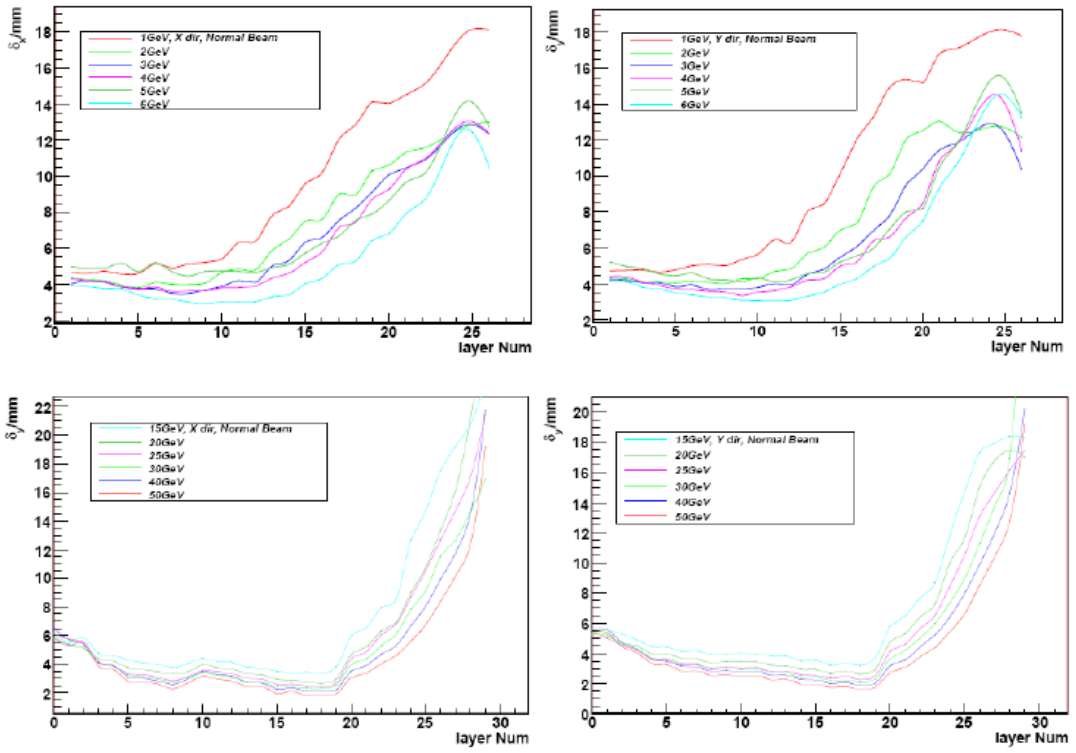

Figure 6.19 Spatial resolution per layer vary with beam energy（Up, Desy runs; lower, CERN Runs; left, X direction; right, Y direction）

Follow the order of left to right and up to low, the 30 plots in Figure 6.18 show the distribution of difference between expected positions (intersection point) and measured positions (energy weighted center) of all 30 layers. For the first 3 layers, since the energy deposition and number of hits are small, the distributions are not perfect Gaussians and the spatial resolutions are not good. There are nice narrow Gaussian distributions for the middle layers with large number of hits and the majority of energy deposition. And for the last 4 layers, since the shower have yet deposited most of its energy, the spatial resolution gets worse again.

We have the spatial resolution depend on layer number for different beam energy, shown in Figure 6.19. It's not surprising that with increasing the beam energy we get better spatial resolution; as for an individual run, the spatial resolution also gets better for layers with larger energy deposition.

The result of angle measurement has been demonstrated in Figure 6.20. The measured angle agrees nicely with the marked angle (10^{o}=174.5mrad). In the next section we will systematically show the results for different runs, and study the energy dependence of angle measurement accuracy.

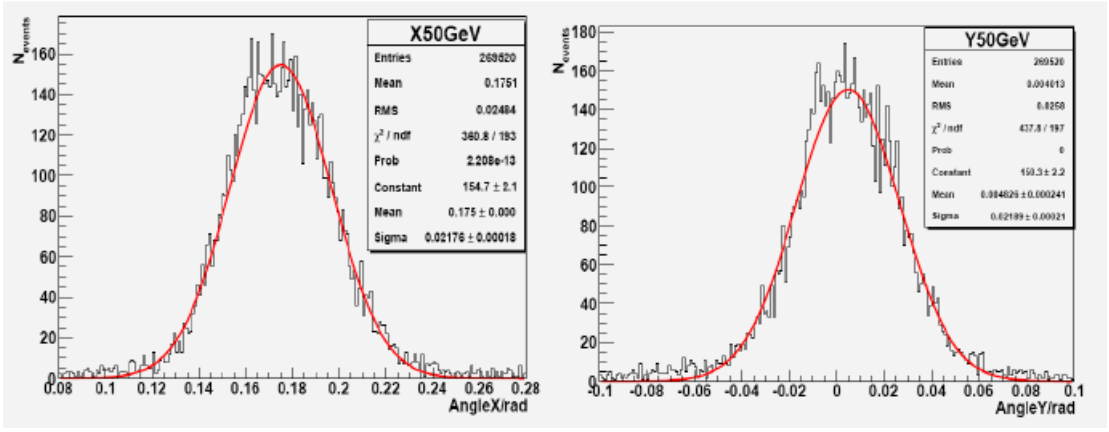

Figure 6.20 Angle measurement for Run330986 (50GeV electron run, inject with 10Degree angle in X direction)

6.4.3 The result of the angle measurement

In Table 6.3 (Normal inject runs) and 6.4 (Runs inject with 10^o or 20^o angle) we summarize the angle measurement result for all the 24 runs.

Run number	Inject angle	Beam energy/GeV	Event selection/mips	θ_x (mrad)	θ_y (mrad)
330228	0^o	50	5k - 8k	7.8 ± 16.1	0.8 ± 21.9
330224		40	3k - 6k	6.6 ± 18.0	0.7 ± 23.5
330456		30	3k - 4.5k	8.5 ± 19.2	1.0 ± 25.0
330431		25	2.5k - 4.5k	11.3 ± 20.0	0.1 ± 23.9
330423		20	1.5k - 3.5k	16.3 ± 23.3	-1.6 ± 26.9
330433		15	1.5k - 2.5k	9.1 ± 26.4	-1.3 ± 29.4
230101		6	0.6k – 1.2k	14.2 ± 38.2	1.2 ± 36.9
230104		5	0.5k – 1.0k	12.6 ± 44.4	2.6 ± 43.3
230100		4	400 – 800	14.6 ± 47.4	1.8 ± 45.8
230097		3	300 – 600	12.3 ± 53.9	1.2 ± 51.2
230099		2	150 – 450	15.5 ± 63.5	0.2 ± 59.9
230098		1	90 – 230	11.8 ± 82.1	-1.8 ± 80.3

Table 6.3 Angular measurement result for normal inject runs

In Table 6.3 we find that the angular measurement accuracy gets better with increasing the beam energy, as the spatial resolution per layer gets better with larger beam energy. For the CERN runs, the central value of angular measurement in the X direction is about 10mrad, and about 3.5mrad in the Y direction. Similar derivation from expectation value (0mrad) also observed in the DESY runs, which might be caused by the experimental setting.

Figure 6.21 shows a comparison of our track-free algorithm and previous CALICE result (**[ref6.5]**). Our result is comparable with the CALICE previous result, which use the drift chamber information to reconstruct the reference line. It is also very clear that the angle measurement goes better with larger

beam energy, we have roughly $\delta\theta \approx (74/\sqrt{E/GeV}+8.7)mrad$: as well as the energy measurement, the angular measurement goes better with square root of the beam energy.

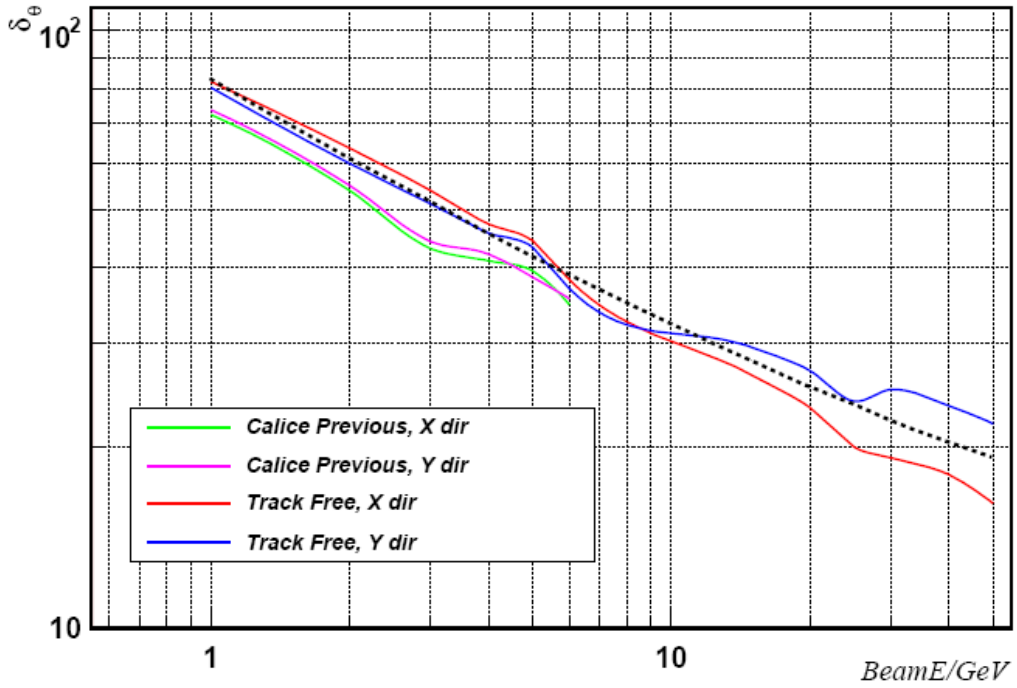

Figure 6.21 Dependence of angle measurement accuracy and beam energy

Table 6.4 shows the angle measurement results for run with 10^o or 20^o inject angle (in X direction). The measurements give consistent result with the marked angles (10^o＝174.5mrad，20^o＝349mrad). Similar as the normal inject case, there have about 3mrad derivation in both X and Y directions for 10^o inject runs, while for 20^o inject runs, we have about -10mrad derivation in the X direction and 2mrad derivation in the Y direction.

Run number	Inject angle	Beam Energy/GeV	Event selection/mips	θ_x (mrad)	θ_y (mrad)
330986	10^o	50	5k - 8k	175.0 ± 21.8	4.8 ± 21.9
330990		40	3k - 6k	173.6 ± 23.2	4.6 ± 22.8
330993		30	3k - 4.5k	176.0 ± 24.9	2.8 ± 24.1
330994		25	2.5k - 4.5k	179.4 ± 25.2	2.5 ± 26.1
330995		20	1.5k - 3.5k	175.5 ± 28.0	1.5 ± 28.6
330996		15	1.5k - 2.5k	177.3 ± 29.5	0.9 ± 31.4
331209	20^o	50	5k - 8k	337.9 ± 15.0	3.7 ± 20.5
331207		40	3k - 6k	337.0 ± 16.7	3.9 ± 22.2
331204		30	3k - 4.5k	339.0 ± 18.5	3.0 ± 23.0
331202		25	2.5k - 4.5k	341.3 ± 19.3	2.8 ± 24.0
331198		20	1.5k - 3.5k	338.7 ± 21.6	1.9 ± 26.7
331194		15	1.5k - 2.5k	340.1 ± 23.8	1.1 ± 29.2

Table 6.4 Angle measurement for run with 10^o or 20^o inject angle

6.5 Summary

In this chapter we briefly introduced the interaction between materials and charged particles (electron, π, μ) and the shower development in the calorimeter. Based on which we discussed the energy, spatial and angular resolution of the CALICE ECAL prototype. For the energy and spatial resolution, we call the previous results of the CALICE collaboration, while the angle measurement is an independent work of this thesis.

The CALICE ECAL prototype has good energy and spatial resolution, and the measured result agrees with the Monte Carlo simulation nicely.

For the angular resolution, we developed an algorithm based on ECAL information only, and test its performance with totally 24 runs (Energy range 1-50GeV, inject angle 0^o, 10^o, 20^o). In comparing to the previous result of the CALICE collaboration (DESY runs with 1-6GeV beam energy), which using

the drift chamber resolved track as reference, we find our result is comparable with previous result for 1-3GeV beam energy, while our result is slightly better than the previous result for 4-6GeV beam energy.

With our algorithm, the measured angle agrees with the expected angle, We found that the angular resolution is fit well by a function varying with the square root of the beam energy (as the energy resolution), and we were able to achieve a precision of approximately $\delta\theta \approx (74/\sqrt{E/GeV} + 8.7)mrad$ in the angular resolution.

Chapter 7 Summary and perspective

7.1 Summary of the thesis

This thesis has mainly focused on ILC detector studies. Contributions of this thesis are mainly twofold: first, the analysis of Higgs boson mass and cross section measurements at the ILC (with full simulation of the $e^+e^- \to HZ \to H\mu\mu$ channel and corresponding backgrounds); second, an analysis of CALICE test beam data. A preliminary study on beam parameter selection has also been performed.

The detector is a very complex system, and its exact performance is difficult to predict solely via theoretical calculations. Before its construction, numerous Monte Carlo simulations and test beam experiments must be performed to ensure that the detector can achieve its optimal performance. The sequence of detector R&D then goes something like the following:

First, develop Monte Carlo tools and perform test beam experiments where feasible.

As noted in pervious chapters, the ILC detector is required to achieve a jet energy resolution of $0.3/\sqrt{E/GeV}$, which is roughly twice as good as that achieved during the LEP experiments. This precision may be achieved via a PFA algorithm and an extremely high degree of spatial granularity in the calorimetry system. Members of the CALICE collaboration have constructed a prototype calorimeter including ECAL, HCAL and TCMT elements. This prototype has been studied in test beam experiments, and one of the important works of this thesis is to analyze data from said experiments.

Second, virtualize the detector utilizing Monte Carlo tools and test its performance for different physical processes with different detector geometries and settings. Though this step, one or more reliable detector concepts may be developed.

This process is known as detector optimization study, and it requires huge amounts of computational resources – since full simulations on a set of benchmark channels must be performed under various detector concepts. The application of grid tools is mandatory for this study. The organization and management of the detector optimization project is very important (That's why people formed the ILD collaboration). For this detector optimization study, we have studied Higgs mass and cross section measurements via the $e^+e^- \to HZ \to H\mu\mu$ channel under the LDC01_Sc detector concept.

Third, summarize the test beam experimental results and/or the full simulation results and develop fast simulation tools (FSTs).

For a given detector, system performance can be summarized by an analytic function, and measured distributions can be regarded as a convolution of the system function (including efficiencies and acceptances) with the actual physical values. This enables the development of FSTs, which make it far more convenient to perform physics analyses prior to the construction of the actual accelerator and detector. By summarizing the μ-momentum measurement at different beam energies and polar angles, we develop a fast simulation package to predict the Higgs recoil mass spectrum. Results obtained using this FST agree nicely with results from our full simulation. This FST was then applied in a study of the Higgs mass measurement under assorted beam parameters to obtain results supporting our beam parameter and center-of-mass energy selections for the full simulation study.

Next let's briefly discuss the motivation and results of this work.

Involving the CALICE test beam data analysis, our work is mainly focused upon two aspects: data quality checks and the track-free ECAL angular measurement. Data quality checks are used to detect strange signals or unexpected phenomena in the test beam data and quickly feed these result back to the rest of the collaboration. They are also used to classify all the runs and summarize them into a report to aid latter analysis work (Chapter 5).

The track-free ECAL angular resolution algorithm is designed to precisely measure the direction of a photon, a very important component in determining the direction of the neutral components in jets. We found that the angular resolution is fit well by a function varying with the square root of the beam energy (as the energy resolution), and we were able to achieve a precision of approximately $\delta\theta \approx (74/\sqrt{E/GeV}+8.7)mrad$ in the angular resolution.

For the full simulation study of the Higgs boson mass and cross section measurements, we chose the $e^+e^- \to HZ \to H\mu\mu$ channel as our signal. Since the ILC has a known and tunable center-of-mass energy, and the μ-momentum can be very precisely measured through the sophisticated tracking system, it is appropriate to consider application of the recoil mass method to measure the Higgs boson mass. The recoil mass method doesn't require any information concerning the final state decay products from the Higgs boson, making it possible for us to execute a model-independent analysis by avoiding using any potentially model-dependent cuts. For a 120GeV Higgs particle, setting the center-of-mass energy to 230GeV and with 500fb^{-1} of integrated luminosity, a precision of 38.4MeV was obtained for the Higgs boson mass measurement, while the cross section could be measured to 5%; if we make some assumptions about the Higgs boson's decay, for example a Standard Model Higgs boson or a invisibly-decaying Higgs boson, measurement results could be improved by 25% (achieving a mass measurement precision of 29MeV and a cross section measurement precision of 4%).

We considered all the radiation effects (BS, ISR and FSR) and all possible SM backgrounds in our full simulation. We also utilized the LDC01_Sc detector model, which may be regarded as a minimalist conception for an LDC detector. The beam is assumed to be unpolarized in our simulation, although if we had used the default beam-polarization parameters, we would greatly suppress the WW background and increase the signal cross section by 58%. Considering this, our results for the mass measurement precision – 38.4MeV – could be regarded as conservative compared to what might be achievable at the ILC. Nonetheless, it is already about an order better than that expected at the LHC. That's why the ILC is needed to precisely measure Higgs boson properties.

As well as detector optimization, we need to optimize the beam settings for different physics measurements. With the fast simulation tools for the Higgs boson recoil mass spectrum we developed, we studied the variation of the physical performance with different beam parameters as purposed by the BDS group, and the results confirm that setting the center-of-mass energy to 230GeV is a suitable choice (this is the value used in the full simulation study).

7.2 Perspective

Based on the results of this thesis, there are many avenues of investigation open to further inquiry:

First, closer co-operation with the BDS group:

With additional input from the Guinea-pig event generator Whizard, the fast simulation tools we have developed could predict the Higgs boson recoil mass spectrum under different beam parameters and quickly feed said data back to the BDS group. Along the same lines, for different detector conceptions and different physical channels (or different physical measurements) we could develop similar software packages, making it easier and faster for people to do physics analyses and corresponding beam-setting optimization studies.

Second, further analysis on the CALICE test beam data

One main task would be studying the required correction for the ECAL geometrical systematic effect. We could use our Monte Carlo tools to find a shift schedule to achieve good angular resolution performance for 0^{o}—40^{o} from the inject beam. With the low energy hadronic data collected at FNAL this summer, we will have a full spectrum for detector-answering (by energy and by particle type). This could be summarized and included into our simulation tools, thus enabling us to do further analyses --- for example, developing particle identification modules, *etc*.

Third, further full simulation studies of Higgs boson profile measurements.

Following the same sequence of steps as we used in the Higgs boson mass measurement, we could do many further studies on measuring other Higgs boson properties --- for example, a constrained fit on the Higgs boson mass measurement through hadronic decay final states with the $e^+e^- \to HZ$ channel. Compared to the recoil mass method we have studied, this method is expected to perform better at higher center-of-mass energies. With support from jet-flavor-tagging and particle-identification packages, we can precisely measure the decay branching ratios of the Higgs particle (for a light Higgs particle, decays are mainly into b, c, and τ pairs) and calculate the corresponding couplings. Studies of the measurement of the Higgs-W coupling through the W fusion process ($e^+e^- \to Hvv$), measurements of the Higgs self-coupling, *etc.* also merit consideration.

Results from such studies could be quickly fed back to the ILD collaboration, providing reference for further studies on ILC detector optimization.

Reference

[1] ILC Passport on line: http://www.linearcollider.org/gateway

[2] International Linear Collider Reference Design Report, Physics case Part

[3] LHC homepage: http://lhc.web.cern.ch/lhc

[4] ILC homepage: http://www.linearcollider.org

[5] P. Wienemann, Physics at the ILC, report at Tsinghua ILC Summer School 2005.

[6] P. Gay, et al. Energy Flow with high granujlarity calorimeters, report at LCWS2000, Fermlab, Oct, 2000.

[7] M. A. Thomas, Particle Flow Calorimetey at the ILC, arXiv:physics/0607261v1.

[8] CALICE group webpage: http://polywww.in2p3.fr/activites/physique/flc/calice.html

[9] W. Siegel. Fields. 3rd edition, Aug 2005. hep-th/9912205 v3.

[10] M. Gomez-Bock, et al. Concepts of Electroweak Symmetry Breaking and Higgs Physics, http://arxiv.org/abs/0712.2419v1

[11] LEP Higgs search webpage: http://lephiggs.web.cern.ch/LEPHIGGS/papers/index.html

[12] F. Richard and P. Bambade. Strategy to measure the Higgs mass, width and invisible decay at ILC, CARE-ELAN Document-2007-001.

[13] M. Ruan. Higgs mass measurement through μ channel of Higgs strahlung process, report at Zeuthen ILD workshop, Jan 2008.

[14] ECFA/DESY LC Physics Working Group, J. A. Aguilar-Saavedra, et al. TESLA Technical Design Report Part III: Physics at e+e- Linear Collider. hep-ph/0106315.

[15] V. Barger, et al. Higgs Bosons: Intermediate Mass Range at e+e- Collider. Phys.Rev.D49 (1994) 79.

[16] D. J. Miller et al. Phy. Lett.B 505 149 (2001).

[17] M. T. Dova et al. Determination of the Higgs boson spin with a linear e+e- collider. arXiv: hep-ph/0302113.

[18] E. Accomando et al. Phys. Rep. 299 (1998) 1; J.A. Aguilar-Saavedra et al. TESLA TDR, hep-ph/0106315; A. Diouadi et al. ILC RDR, arXiv: 0709.1893 [hep-ph].

[19] J. Alcaraz and E. Ruiz Morales, Phys. Rev. Lett. 86, 3726 (2001), [hep-ph/0012109].

[20] K. Desch, Higgs boson precision study at a Linear Collider [hep-ph/0311092].

[21] A. Gay. presentation at the ECPA/DESY Workshop, Amsterdam 2003 LC-Note 2004, and in hep-ph/0311092, Higgs Boson Precision Studies at a Linear Collider.

[22] C.Castanier, et al. Higgs self coupling measurement in e+e- collisions at center-of-mass energy of 500 GeV. hep-ex/0101028.

[23] Y.Yasui, et al., Measurement of the Higgs self-coupling at JLC, arXiv: hep-ph/0211047v2.

[24] International Linear Collider Reference Design Report, Accelerator Part.

[25] International Linear Collider Reference Design Report, Detector Part.

[26] ILD group webpage: http://www.ilcild.org

[27] M. Thomas, ILD Detector Optimization Strategy, Report at ILD Meeting, 14/01/2008, DESY, Zeuthen.

[28] MOKKA homepage: http://polzope.in2p3.fr:8081/MOKKA

[29] R. Poeschl. Software status and First look into Data of irradiation test, report on CALICE phone meeting, August 2007.

[30] C. Rimbault. Guinea-Pig, a tool for beam-beam effect study, report at Daresbury, April 2006.

[31] Guinea-Pig support: http://flc.web.lal.in2p3.fr/mdi/BBSIM/bbsim.html

[32] ILCSOFT gateway: http://www-zeuthen.desy.de/linear_collider

[33] LCIO homepage: http://lcio.desy.de

[34] Marlin homepage: http://ilcsoft.desy.de/marlin

[35] F. Gaede. The LDC Software framework, report at 6th SiLC meeting, University of Torino, Dec 2007.

[36] Whizard homepage: http://whizard.event-generator.org

[37] Pythia homepage: http://home.thep.lu.se/~torbjorn/Pythia.html

[38] STDHEP homepage: http://cepa.fnal.gov/psm/stdhep

[39] Geant4 homepage: http://geant4.web.cern.ch/geant4

[40] T. Behnke. Simulation and Reconstruction Software for the ILC. http://confluence.slac.stanford.edu/download/attachments/8535/software.pdf?version=1

[41] MySQL homepage: http://www.mysql.com

[42] Gear homepage: http://ilcsoft.desy.de/portal/software_packages/gear

[43] MarlinReco homepage: http://ilcsoft.desy.de/portal/software packages/marlinreco

[44] R.Morgunov and A. Raspereza. Novel 3D Clustering Algorithm and Two Particle Separation with the HCAL. arXiv:physics/0412108.

[45] PandoraPFA homepage: http://www.hep.phy.cam.ac.uk/~thomson/pandoraPFA

[46] M. Ohlerich, et al. Analysis details for a Higgs recoil mass study with MOKKA and MarlinReco, report at LDC Optimization Meeting, Orsay, July 2007.

[47] A. Gellrich. The Grid-Future of Scientific Computing, EGEE-II, INFSO-RI-031688.

[48] LCCD homepage: http://ilcsoft.desy.de/lccd

[49] CondDBMySQL homepage: https://savannah.cern.ch/projects/conddb-mysql

[50] CALICE software webpage: http://www-flc.desy.de

[51] Ilcinstall webpage: http://ilcsoft.desy.de/portal/software_packages/ilcinstall

[52] RooFit webpage: http://root.cern.ch/root/html/RooFit.html

[53] PAW webpage: http://wwwasd.web.cern.ch/wwwasd/paw

[54] K.Belotsky, et al., Invisible Higgs Boson Decay into Massive Neutrinos of 4th Generation, arXiv: hep-ph/0210153v1.

[55] A. Seryi, et.al. For discussion of GWP04 IR integration, report at Nov 2007.

[56] J. Brau, R&D for future detectors, report at 2004 ICHEP, Beijing. Aug, 2004

[57] CALICE Analysis Note 001: Study of the response of the CALICE silicon-tungsten electromagnetic calorimeter prototype to electrons

[58] CALICE Analysis Note 003: Preliminary result from hadron shower data with the CALICE tile AHCAL prototype

[59] G. Lima. CALICE TCMT beam test status, report at ALCPG-Calorimetry meeting, Nov 2006

[60] CALICE Analysis Note 005: The Scintillator-ECAL Beam Test at DESY, 2007

[61] V. Ammosov, Status and plans of DHCAL RPC R&D in IHEP, report at CALICE meeting, Amsterdam, May 2003.

[62] CERN beam introduction: http://sl.web.cern.ch/sl/eagroup/beams.html

[63] Data summary for 2007 CALICE testbeam experiment [EB/OL]: http://www.pp.rhul.ac.uk/%7Ecalice/fab/WWW/dataSummary.htm

[64] CALICE elog webpage: https://ttfinfo.desy.de/CALICEelog-sec/index.jsp

[65] F. Salvatore and E. Garutti, The 2007 CALICE test beam, report at CALICE meeting Prague, Sep. 2007.

[66] DESY webpage: http://www.desy.de

[67] FNAL webpage: http://www.fnal.gov

[68] J-Y. Hostachy and L.Morin. Presentation and discussion about the energy measurement in the ECAL, report at CALICE meeting Prague, Sep, 2007.

Acknowledgements

My deepest gratitude goes first and foremost to Professor Yuanning Gao and Professor Zhiqing Zhang, my supervisors, for their encouragement and guidance. They provided me many opportunities to learn the knowledge on particle physics and practice my working skills; they have walked me through all stages of the work of this thesis. Without their continuous support, this thesis could not have reached its present form.

I would like to express my heartfelt gratitude to Professor Francois Richard, who has taught me a lot on both theory and experiment. He always inspired me with great new ideas; He has so strong instinct on Physics that the discussions with him are really wonderful and indelible.

Many thanks to Roman Posechl, who has taught me so much on the technical stuffs of software and experiments. His help and support comes in the darkest time in my thesis and really means a lot to me. I will always remember his continuous help on the experiment.

Thanks to Professor Philip Bambade, who has taught me many things on the accelerator Physics. Philip is one of the few people who kept try to speak French with me, encourage me a lot to embed deeper into the French culture. Thanks also for his kind hospitality at his house.

Thanks to Doctor Zhenwei Yang and Professor Shaomin Chen, who always helps me during this thesis.

Last my thanks would go to Qiong Liu, my beloved family and friend for her understanding, support and the great confidence in me through these years. Thanks to Tingting and Wudi, my best friends.

I also owe my sincere gratitude to my friends and colleagues at ILC group and TUHEP, Vincent, Jibo, Oliver, …

CV and Publication

CV

Born on April 11th, 1982, at Huangshan city of Anhui province, China.

2003.9 – 2008.11, Bachelor degree on Biomedcial Engineering, at Tsinghua University, Beijing, China.

2003.9 – 2008.11, Co-supervision Ph.D student on particle physics between TUHEP, Tsinghua University (Beijing, China) and LAL, Paris-XI University (Orsay, France).

Publication

[1] RUAN Manqi, ZENG Jinyan. Construction of the EPR Entangled States. Chinese Physics Letter. Vol. 20, No. 9, (2003) 1420

[2] RUAN Manqi, ZENG Jinyan. Complete sets of commuting observables of GHZ states; April. 2004, P.R.A

[3] RUAN Manqi, XU Gang, ZENG Jinyan. Three types of maximally entangled states for a two-particle system. Science in China (Series G), 2004 47 (1)

[4] RUAN Manqi, XU Gang, ZENG Jinyan. Costruction of GHZ-like States for a Three-Particle (Spin-1/2) System. Commun. Thero. Phys. 42 (2004) 51-54

[5] CALICE Collaboration, Design and Electronics Commissioning of the Physics Prototype of a Si-W Electromagnetic Calorimeter for the International Linear Collider. arXiv:0805,4833

[6] M. Ruan, Y.Gao, F.Richard and Z.Zhang. A precision determination of Higgs mass using the fully simulated Higgsstrahlung process ee→HZ→Hμμ at ILC (Note to be published)

[7] M. Ruan, Z.Zhang. A determination of the angular resolution of ECAL using CALICE test beam data (CALICE internal note)